DYNAMIC SQUARE PATTERNS IN TWO DIMENSIONAL NEURAL FIELDS

by

Kevin R. Green

A Thesis Submitted in Partial Fulfillment
of the Requirements for the Degree of

Doctor of Philosophy

in

The Faculty of Science

Modelling and Computational Science

University of Ontario Institute of Technology

July 29, 2015

This thesis is dedicated to my family,

for the endless moral support throughout my education.

Abstract

The goal of this thesis is to study the emergence of spatiotemporal waves in neural field models. Neural field models aim to describe the activity of populations of neurons at a mesoscopic scale, considering averaged neuronal states dependent on continuous space and time. Mathematically, they are composed of spatial and temporal integral operators on domains of anatomical interest. The cortex is modelled as a two dimensional sheet, and under physiological assumptions for the spatial extent of connectivities, it is shown when the principal transition from resting to active states will result in the formation of waves. This thesis starts with a derivation for the integral operators from a physiological viewpoint. The notion of a dynamical system is then introduced, and theory relevant to the spontaneous emergence of activity is discussed. The thesis progresses to applying the dynamical systems view to neural fields, leading to an understanding of the transitions from inactive resting states to space dependent temporal oscillations – waves. For tractable analysis, the active states are restricted to have square periodic symmetry.

Acknowledgements

First and foremost, I would like to thank the members of my advisory committee: Lennaert van Veen, Greg Lewis, and Mark Daley, whose work has been a constant source of inspiration. It is the little thoughts from Greg Lewis and Mark Daley that are most memorable, keeping me on track from an early stage. I am grateful to be the first PhD student of Lennaert van Veen, who will surely have a long line of talented researchers develop under his supervision.

I thank Pietro-Luciano Buono, for his ability to plant the seeds of ideas. Without his input, the role of symmetry, which touches all aspects of the results in this thesis, would have been much less prominent. I also thank all of the MCSC graduate students who have been here during my studies. As a very small program, I am lucky to have enjoyed all of the personalities that have passed through.

I would like to thank Axel Hutt for hosting me at INRIA Nancy from February to June of 2014. This was the perfect opportunity I needed to connect a few of the disjoint ideas that had been implanted over the first years of my studies. I thank Eric Nichols for his software work with the nfSimulator project. I also thank the rest of INRIA Team Neurosys For welcoming me with bright smiles, and making my time in Nancy socially enjoyable as well.

Finally, I thank my external examiners: Stefanos Folias, and Bernadette Murphy. I am particularly pleased that Stefanos Folias agreed to examine this thesis, as well as make the long journey from Anchorage, Alaska, for the oral examination. While Bernadette Murphy did not have to make such a long trip, her time spent reviewing this thesis is still greatly appreciated.

This work was funded in part by OGS and NSERC PGS-D scholarships.

Contents

Page

Abstract v

Acknowledgements vii

Contents ix

List of Figures xiii

List of Tables xv

Notation xvii

1 Introduction 1
- 1.1 Overview . . . 1
- 1.2 An historical note . . . 2
- 1.3 Publications . . . 3
- Bibliography . . . 3

2 Physiology & modelling 5
- 2.1 Neocortex physiology . . . 6
  - 2.1.1 Structure of the human brain . . . 6
  - 2.1.2 The pyramidal cell . . . 6
  - 2.1.3 Cortical columns . . . 7
  - 2.1.4 Towards measurement . . . 10
  - 2.1.5 EEG rhythms . . . 13
- 2.2 Neural field models . . . 14
  - 2.2.1 A brief history of neural masses . . . 15
  - 2.2.2 Neural field components . . . 16
- 2.3 Scalar neural field . . . 20
  - 2.3.1 Specific components . . . 21
- 2.4 Liley's neural field model . . . 25

2.4.1 General form . . . 25
2.4.2 Specific form of components . . . 26
2.5 Summary . . . 28
Bibliography . . . 30

3 Dynamical systems **33**
3.1 Finite dimensional dynamical systems . . . 34
3.1.1 Equilibrium solutions . . . 35
3.1.2 Hopf bifurcation . . . 36
3.1.3 Periodic solutions . . . 38
3.2 Infinite dimensional systems . . . 40
3.2.1 Equilibrium solutions . . . 40
3.2.2 Linear stability . . . 41
3.2.3 Bifurcation from dispersion relation . . . 42
3.3 Bifurcations with symmetry . . . 43
3.3.1 General problem . . . 43
3.3.2 $D_4 \ltimes T^2$ Hopf bifurcation . . . 44
3.4 Continuation . . . 47
3.4.1 General methods . . . 49
3.4.2 Applied to equilibria . . . 51
3.4.3 Applied to bifurcations of equilibria . . . 52
3.4.4 Applied to periodic orbits . . . 53
3.4.5 Applied to continuous dispersion relations . . . 54
3.4.6 Applied to bifurcations of SHE . . . 54
3.5 Summary . . . 56
Bibliography . . . 56

4 Analysis of a scalar neural field **59**
4.1 Preliminaries . . . 60
4.1.1 Integral transforms . . . 60
4.1.2 Firing function . . . 61
4.2 Spatially homogeneous dynamics . . . 61
4.2.1 Continuation . . . 62
4.2.2 Linearization and dispersion relations . . . 63
4.2.3 Homogeneous dynamics . . . 64
4.3 $D_4 \ltimes T^2$ symmetric Hopf . . . 64
4.3.1 Finding dynamic Turing bifurcations . . . 64
4.3.2 $D_4 \ltimes T^2$ Normal form . . . 75
4.3.3 Locating degeneracies . . . 75
4.4 Simulation . . . 78
Bibliography . . . 80

5 Analysis of Liley's model **83**
5.1 Preliminaries . . . 84
5.1.1 Linearization and dispersion . . . 86
5.1.2 $D_4 \ltimes T^2$ symmetric Hopf . . . 87
5.1.3 Simulation . . . 90
5.1.4 Periodic orbit computations . . . 93
5.1.5 Initialization of $D_4 \ltimes T^2$ modes . . . 94
5.2 Parameter set I . . . 95
5.2.1 Origin . . . 95
5.2.2 Building on previous work . . . 98
5.3 Parameter set II . . . 105
5.3.1 Origin . . . 105
5.3.2 Building on previous work . . . 105
Bibliography . . . 110

6 Conclusions **113**
6.1 Summary . . . 113
6.2 Discussion of results . . . 114
6.2.1 Comparisons and extensions . . . 114
6.3 Conclusions . . . 117
6.4 Further work . . . 118
Bibliography . . . 120

A Resources for scalar equation **123**
A.1 Calculations . . . 123
A.1.1 Details of separation of scales calculation . . . 123
A.1.2 Details of Fredholm alternative inner products . . . 127
A.2 Initialization files for nfSimulator . . . 129

B Resources for Liley's model **131**
B.1 Calculations . . . 132
B.1.1 Equivalence of Integral and PDE models . . . 132
B.1.2 Normal form coefficient example . . . 132
B.2 Numerical algorithm descriptions . . . 134
B.2.1 PETSc overview . . . 134
B.2.2 Timestepping . . . 135
B.2.3 Stepping of the first variational equation . . . 136
B.2.4 Equilibria . . . 137
B.2.5 Periodic solutions . . . 138
B.3 PETSc simulation code initialization files . . . 139
B.4 Testing of simulation code . . . 139
B.4.1 Numerical timestepping error . . . 139
B.4.2 Accuracy testing . . . 139
Bibliography . . . 141

C Copyright permissions **143**
C.1 Oxford – Nunez & Srinivasan 2006 144
C.2 IOP Publishing – Silber & Knobloch 1991 146
C.3 Elsevier – Frascoli et al. 2011 149
C.4 Elsevier – Bojak & Liley 2007 156

List of Figures

Page

2.1 The human brain (exterior) . . . 7
2.2 The human brain (interior) . . . 8
2.3 Single pyramidal neuron . . . 9
2.4 Schematic of cortical column . . . 10
2.5 Dipole layers in the cortex . . . 11
2.6 Dipole alignment and EEG electrode measurement . . . 12
2.7 Dipole alignment and MEG magnetometer measurement . . . 13
2.8 Single neuron and population firing functions . . . 19
2.9 View of spatiotemporal connectivity on Ω . . . 20
2.10 Dendritic response with a single exponential time scale . . . 21
2.11 Dendritic response with two exponentially decaying time scales . . . 22
2.12 Dendritic response for alpha function . . . 23
2.13 *Wizard hat* connectivity . . . 24
2.14 Double exponential connectivity . . . 25
2.15 Schematic view of Liley's model . . . 28

3.1 Unfolding of the Hopf bifurcation . . . 38
3.2 Dynamic Turing bifurcation . . . 43
3.3 Travelling wave modes of $D_4 \ltimes T^2$ Hopf bifurcation . . . 46
3.4 Standing wave modes of $D_4 \ltimes T^2$ Hopf bifurcation . . . 46
3.5 Alternating roll mode of $D_4 \ltimes T^2$ Hopf bifurcation . . . 47
3.6 All $D_4 \ltimes T^2$ unfolding diagrams . . . 48
3.7 Parameter continuation . . . 50
3.8 Pseudoarclength continuation . . . 51

4.1 Continuations of scalar SHE . . . 63
4.2 Λ^{CONT}, stable for all k . . . 65
4.3 Λ^{CONT}, stable for all k . . . 65
4.4 Λ^{CONT}, unstable to spatially homogeneous oscillations . . . 66
4.5 Λ^{CONT}, stable for all k, potential for dynamic Turing . . . 66
4.6 Λ^{CONT}, unstable for some k, potential for dynamic Turing . . . 67

4.7 Λ^{CONT}, at a dynamic Turing bifurcation 68
4.8 How the steepness parameter effects branching of $D_4 \ltimes T^2$ modes . . 77
4.9 Direct numerical simulation of scalar model: stable TR and AR . . . 79
4.10 Direct numerical simulation of scalar model: random IC 80

5.1 Jacobian structure for Liley's model on a 3x3 periodic grid 91
5.2 Distributed regular square grid 92
5.3 Reproduction of continuations from Bojak & Liley, 2007 96
5.4 Reproduction of dynamic Turing bifurcations from Bojak & Liley, 2007 97
5.5 Reproduction of temporal power spectra from Bojak & Liley, 2007 . . 97
5.6 Numerically computed unstable mode 99
5.7 Gamma oscillations and hot spots in PS1 100
5.8 Spectral power of spatially averaged timeseries 101
5.9 Temporal period along SHPO branch in PS1 102
5.10 Spectral power for spatially homogeneous periodic solution 102
5.11 Critical branch of Λ^{CONT} for PS1 at left dynamic Turing bifurcation . 103
5.12 Critical branch of Λ^{CONT} for PS1 at right dynamic Turing bifurcation 103
5.13 PS1 Homogeneous diagram with bifurcation zoom 105
5.14 Homogeneous dynamics of PS2 107
5.15 Least stable branch of Λ^{CONT} for PS2 at dynamic Turing bifurcation 108
5.16 Neutral stability curves for PS2 109
5.17 Bifurcation zoom in for PS2 SS branch 110
5.18 Standing square solution in Liley's model 111

B.1 Schematic representation of the components of PETSc and SLEPc . . 135
B.2 Timestepping error for Liley's model 140

List of Tables

Page

2.1 Brain rhythms 13
2.2 Meaning and ranges for parameters of Liley's model. 29

3.1 $D_4 \ltimes T^2$ amplitudes and branching conditions 46

4.1 Parameters that give a dynamic Turing bifurcation 70
4.2 Branching diagram characteristics for varying steepness 76
4.3 Degeneracy conditions for branch flipping 76

5.1 Algorithm list for a large system 93
5.2 PS1: Liley model parameters for 40Hz oscillations 96
5.3 $D_4 \ltimes T^2$ coefficients for PS1 left and right dynamic Turing bifurcations 104
5.4 PS2: Liley model parameters for supercritical Hopf 106
5.5 $D_4 \ltimes T^2$ coefficients for PS2 dynamic Turing bifurcation 108

A.1 Nontrivial quadratic coefficients of u_2 128

Notation

Abbreviations

AR ..... Alternating roll
BC ..... Boundary condition
CSF ..... Cerbrospinal fluid
DFT .... Discrete Fourier Transform
EEG .... Electroencephalogram
EPSP ... Excitatory postsynaptic potential
FD ..... Finite difference
GMRES Generalized minimum residual
IDE ..... Integro-differential equation
ILU ..... Incomplete lower upper
IPSP .... Inhibitory postsynaptic potential
LFP ..... Local field potential
MEG .... Magnetoencephalogram
MFM ... Mean field model
ODE .... Ordinary differential equation
PETSc .. Portable, extensible toolkit for scientific computation
PDE .... Partial differential equation
PS1 ..... Parameter set 1
PS2 ..... Parameter set 2
PSP ..... Postsynaptic potential
SHE ..... Spatially homogeneous equilibria
SHPO ... Spatially homogeneous periodic orbit

SLEPc .. Scalable library for eigenvalue problem computations
SR ..... Standing roll
SS ..... Standing square
TR ..... Travelling roll
TS ..... Travelling square
VSD .... Voltage sensitive dye

Math symbols

$A \circ B$ Function composition, A composed with B
$A * B$ Temporal convolution of A and B
$A \otimes B$ Spatiotemporal convolution of A and B
$A \ltimes B$ Semidirect product between *normal* subgroup A and subgroup B
$\langle A \rangle$ Average value of A (definition dependent on usage)
$\langle A, B \rangle$ Inner product of A and B (definition dependent on usage)

Chapter 1

Introduction

1.1 Overview 1
1.2 An historical note 2
1.3 Publications 3
Bibliography 3

This thesis is directed at studying the nonlinear behaviour of wave forming bifurcations for mesoscopic models of cortical activity. The work presented here is at the forefront of both applied mathematics and mathematical neuroscience, having i) general applicability to equations defined on two dimensional spatial domains with space dependent delays, and ii) specific novel results for neural models that contain long range excitatory connections and delays induced by finite transmission speeds.

1.1 Overview

A brief overview of cortex physiology is presented in Chapter 2, followed quickly by a semi-heuristic derivation of the spatiotemporal neural field operator. Two specific models that make use of this operator are then presented, and their relevance to the physiology discussed.

Chapter 3 gives an introductory view into the world of dynamical systems. While this is indeed a rather large world, a few specific topics relevant to setting up the analyses we perform are presented in some detail. These topics include equilibria bifurcations, normal forms, spatially extended systems, symmetry, and numerical continuation applied to each of these scenarios.

Chapter 4 is where the results start. It begins slowly, presenting results that could easily be found in existing works, but quickly builds to the nonlinear analysis

of the wave forming bifurcation. A normal form for an arbitrary scalar neural field model – one that contains an arbitrary temporal operator (synapse) and an arbitrary spatiotemporal connectivity – that captures the dynamics of two dimensional waves with square periodic symmetry is obtained, with symbolic expressions for the normal form coefficients. Predictions of this normal form are confirmed with direct numerical simulation of the spatiotemporally delayed system.

In Chapter 5, a couple of things happen. First, the analysis of the wave forming bifurcation from the previous chapter is extended to handle a more complicated system of two coupled populations of neurons. This model is complicated both by the addition of interacting populations, and by the separation of postsynaptic and soma membrane potential dynamics. Next, numerical software is developed for general purpose simulation of this complicated model. The software is turned towards the neighbourhood of the wave forming bifurcation, eventually leading to a continuation of one of the branches of waves that emerge.

1.2 An historical note

The work presented in this thesis has been laid out in the progression that makes the most logical sense. This is not, however, the progression in which it was conducted. Perhaps many who have gone through the doctoral process can relate, or maybe they can not. For me, personally, I can not help but chuckle when considering my initial viewpoints and expected progression of the work. So much ignorance in those days, yet so much more now.

For the reader who would like *in* on this humour, the one who wishes to read this work in its temporal ordering, the results would progress as follows.

- Read Chapter 5, ignoring any reference to the integral formulation of Liley's model. Also ignore anything to do with the dynamic Turing bifurcation, as our initial abilities to compute this thing were non existent.
- Skim Appendix B.1.1-B.3, to get an idea of how we were originally planning on studying neural field models.
- Read Chapter 4 in its entirety, and maybe glance at Appendix A. This chapter was the result of us not understanding the dynamic Turing bifurcation at all, and discovering that no relevant literature existed for neural fields in two dimensional space.
- Go back to Chapter 5, now considering all things that have to do with the dispersion relation, all things that have to do with the integral representation of the model, and all unfoldings of square symmetric wave modes in the neighbourhood of dynamic Turing bifurcations.

With this temporal history, some of the results, particularly with respect to Liley's model, do not fit together as perfectly as I would have liked. From my experience, I can only say that this is just the nature of a doctoral dissertation.

1.3 Publications

The publication of results from this thesis tell a similar story to the historical note above. The numerical algorithms and general simulation tools for Liley's model (Sections 5.1.3, 5.1.4, and Appendix B.2) are published in [2]. After this, the numerical tools were turned towards computing a branch of supercritical standing wave solutions (Section 5.3.2) with results published in [3].

The normal form results at the wave forming bifurcation in the scalar field (Chapter 4, and Appendix A) are currently under review, and consist of a heavily modified version of the technical report [1]. The numerical normal form computations in Liley's model are currently unpublished results.

Bibliography

[1] Green, K. R., and Hutt, A. Analysis of a 2D neural field equation with finite transmission speed. Tech. rep., HAL Id: hal-01007667, 2014.

[2] Green, K. R., and van Veen, L. Open-source tools for dynamical analysis of Liley's mean-field cortex model. *Journal of Computational Science 5*, 3 (2014), 507–516.

[3] van Veen, L., and Green, K. R. Periodic solutions to a mean-field model for electrocortical activity. *The European Physical Journal Special Topics 223*, 13 (2014), 2979–2988.

Chapter 2

Physiology & modelling

2.1 Neocortex physiology 6
2.1.1 Structure of the human brain 6
2.1.2 The pyramidal cell 6
2.1.3 Cortical columns 7
2.1.4 Towards measurement 10
2.1.5 EEG rhythms 13
2.2 Neural field models 14
2.2.1 A brief history of neural masses 15
2.2.2 Neural field components 16
2.3 Scalar neural field 20
2.3.1 Specific components 21
2.4 Liley's neural field model 25
2.4.1 General form 25
2.4.2 Specific form of components 26
2.5 Summary 28
Bibliography 30

This section introduces some of the relevant physiology needed to place the models that will be studied. After this, a brief historical view of the progression of neural field/mass modelling is given, moving from the models of Wilson & Cowan [37] forward to Liley's mean field model of the cortex [26]. From there, the integral operators that are commonly found in these models are then derived from a semi-heuristic viewpoint, and the two specific models studied in this thesis are presented in terms of these operators.

2.1 Neocortex physiology

2.1.1 Structure of the human brain

One possible decomposition of the human brain is into the following three high-level regions: cerebrum, cerebellum, and brain stem [21], as visualized in Figure 2.1.

The cerebrum is divided into a left and right hemisphere and accounts for most of our brains' mass. The hemispheres consist of a wrinkled outer layer of *grey matter* – the cerebral cortex, consisting mostly of unmyelinated neurons and glial cells – which is supported by an inner layer of *white matter*, which also consists of glial cells, but contains myelinated axons of neurons as well. The left and right hemispheres of the cerebrum are linked through a structure called the *corpus callosum*, which is visible in Figure 2.2.

The unmyelinated neurons in the cerebral cortex are responsible for local connections within the cortex, while the myelinated axons of the white matter connect the different regions of a cerebral hemisphere to each other, as well as to lower brain centres. The myelin covering of an axon assists with signal transmission properties, increasing speed of transmission while decreasing signal degradation. This allows neurons with myelinated axons to communicate effectively at longer distances.

The cerebral cortex is where much of the higher processing in humans occurs, and it is divided into four lobes: frontal, parietal, temporal and occipital. Each lobe handles various functions, for example the frontal lobes are responsible for functions such as judgement, foresight, and personality [7, 23]. The parietal lobe houses the primary somatosensory cortex, responsible for handling the tactile representation for our sense of touch. Another example, the occipital cortex, houses the primary visual cortex which is responsible for the processing of our visual field.

Despite the large number of functions that the cortex handles, and this apparent separation into lobes, the structure of the neurons within it remains qualitatively similar throughout. This is a large motivating factor for our work: To study the cortex through models related to its physiological structure.

Deeper within the cerebral hemispheres are many more structures, such as the basal ganglia, thalamus, hypothalamus, hippocampus, and the amygdaloid nuclei to name a few. Discussion of the functions of these deeper cerebral structures is deferred at this point for brevity. This thesis will focus on modelling the cortex, so the reader should consult a more prominent source, such as Kandel [21], for details regarding these deeper cerebral structures, the cerebellum, and the brain stem.

2.1.2 The pyramidal cell

Neurons are often thought of as the fundamental building blocks of the brain. They come in many variations based on their location and role. The type of neurons most abundant in the neocortex are called pyramidal cells due to their shape. The main components of these pyramidal cells are their cell body (soma), dendrites and axon. A pyramidal cell is shown in Figure 2.3.

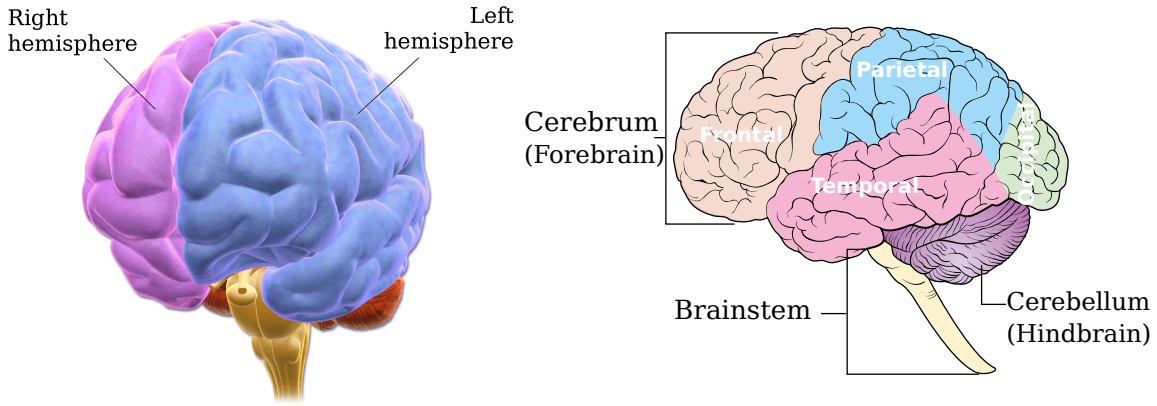

Figure 2.1: Schematic view of the exterior of the human brain. *Left:* The cerebrum is split into two hemispheres. *Image modified from Blausen Gallery 2014 licensed under CC BY 3.0.* *Right:* Both hemispheres can be divided into separate lobes: frontal, parietal, temporal, and occipital, which are generally responsible for handling different cognitive functions. Also visible from the exterior are the cerebellum and the brain stem. *Image modified from Cancer Research UK licensed under CC BY-SA 4.0.*

When a neuron is not firing, it maintains a balance of Na^+, K^+ and Ca^{2+} ions such that the interior of the neuron is at an electric potential of about -70 mV relative to the outside. This is called the rest potential. If the neuron receives enough excitatory input such that this potential difference depolarizes to some critical value, somewhere around -55 mV, the neuron produces an action potential, a rapid depolarization and repolarization of the membrane potential, which travels down the axon. Hodgkin & Huxley developed the original nonlinear model for this *firing* phenomenon based on measurements of the membrane potentials of squid giant axons [18].

Communication between neurons is then done via neurotransmitters, released from an axonal branch once an action potential has reached the end. The neurotransmitters are released into the space between the neurons, called a *synapse*, and picked up by the dendrites of other neurons. In principle, a neuron can release both excitatory and inhibitory neurotransmitters to communicate, but about 90% of the neurons within the cortex seem to be dedicated to one or the other [32]. To give an idea of the composition of the human neocortex, the primary inhibitory neurotransmitter (gamma-aminobutyric acid, GABA) accounts for 20% to 44% of all neurotransmitters within it [33].

2.1.3 Cortical columns

Every larger structure we speak of, e.g., the hippocampus or the cerebral cortex, is composed of millions to billions of a variety of neurons. The human neocortex however, seems to be made up itself of functional units that are composed of many neurons in groupings that are perpendicular to the cortical surface. These units that fire

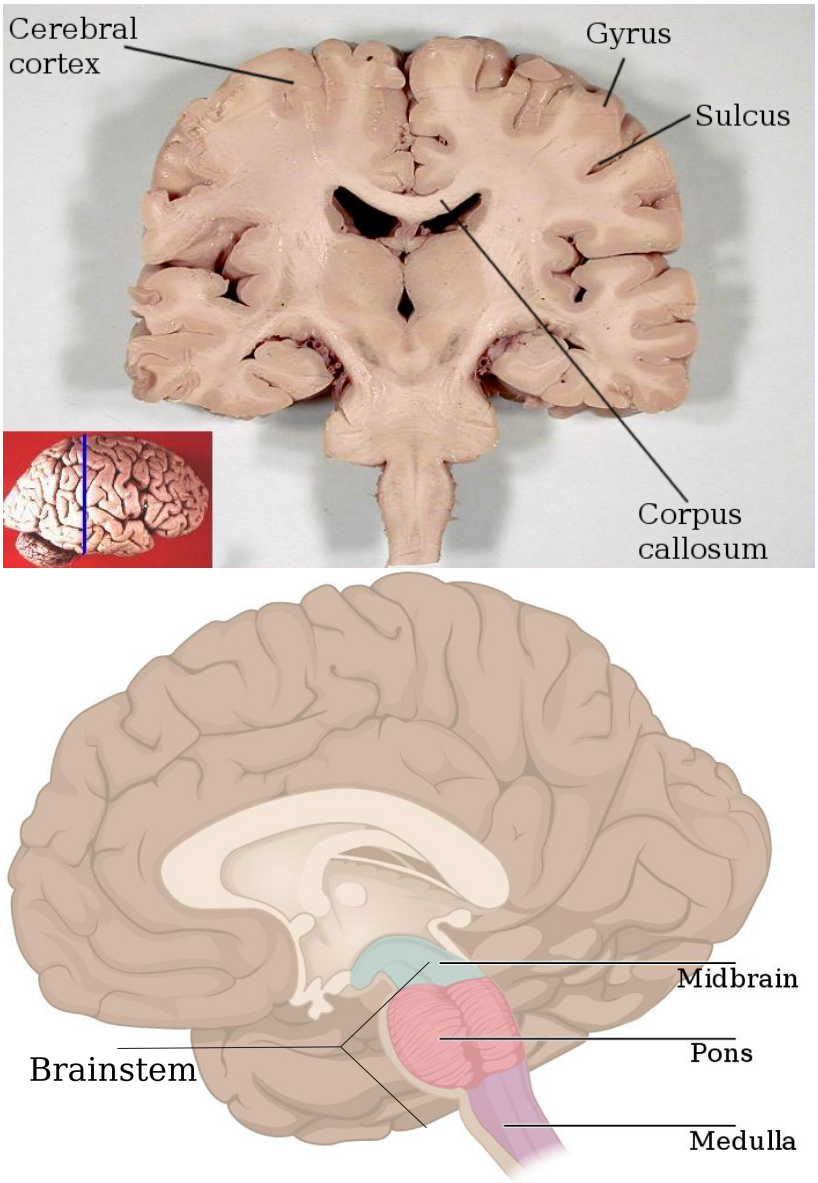

Figure 2.2: View of the interior of the human brain, showing deeper structure from two cross sections. *Top:* Cross section through the coronal plane, showing both cerebral hemispheres. Gyri and sulci are highlighted in the cerebral cortex, and the corpus callosum is labelled. While other deeper cerebrum structures could be highlighted from this view, we omit labels for brevity. *Image modified from John A. Beal licensed under CC BY 2.5.* *Bottom:* Schematic cross section through the sagittal plane (cerebellum omitted), showing the right cerebral hemisphere. This view also shows division of the brain stem into the midbrain, pons, and medulla. *Image modified from OpenStax College licensed under CC BY 3.0.*

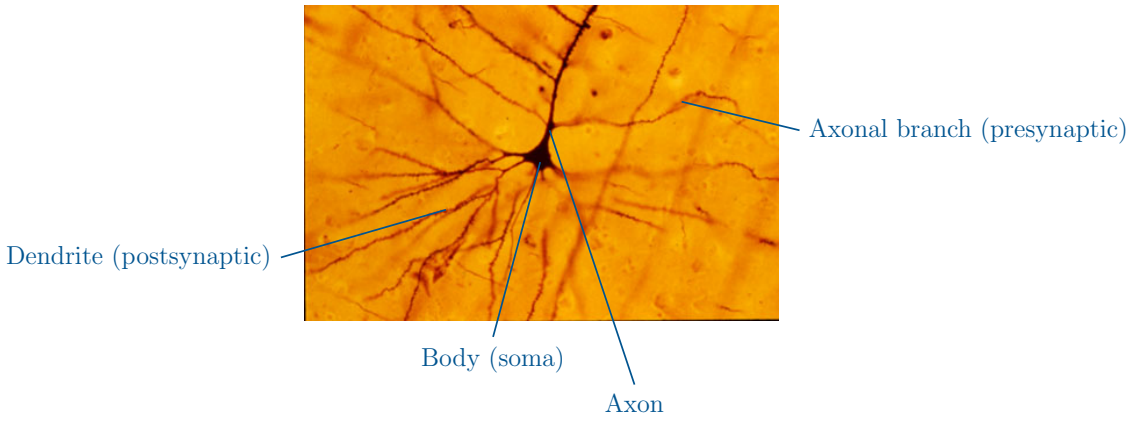

Figure 2.3: A single pyramidal neuron. The dendrites are stimulated by neurotransmitters from other neurons, and their resulting potentials are summed at the soma. Once the soma potential is above a threshold, the neuron undergoes an action potential that travels through the axon and its branches, releasing neurotransmitters to other neurons. *Image from Bob Jacobs licensed under CC BY-SA-2.5.*

coherently are referred to as *minicolumns*, and are composed of about 100 pyramidal cells and a million or so synapses, all in a radius of about 0.03 mm. In some regions of the cortex, even larger scale has been observed: *Macrocolumns*, which are composed of 80 or so minicolumns, and have radii around 0.5 mm [32].

This idea of a macrocolumnar scale comes originally from Mountcastle [29], who determined that neurons perpendicular to the local cortical surface have common receptive fields at about this length scale. The *receptive field* of a neuron is a region in space in which the presence of a stimulus will alter the behaviour of that neuron. Thus, this scale is relevant for elements of sensory cortex.

Mountcastle, for example, looked at the neural response to applying pressure (among other things) to various regions of cats' skin. For a given location, correlated neuronal firing in the cortex was observed mostly in localized regions perpendicular to the local cortical surface. It is for this reason that macrocolumns are thought of as the functional scale of the cortex. These macrocolumns can overlap, but the degree to which they do is not very well known, and most likely varies with region. While this idea originated in the 1950s, it is still considered to be a useful scale for cortex dynamics [30], provided one is wary of all the ways that the term *cortical column* is used [35].

In humans, the columns in the neocortex have six layers numbered from outermost to innermost I-VI, as shown in Figure 2.4. Layers I and VI are responsible mostly for intracortical and corticocortical excitation. The middle layers are where most of the relatively short range inhibition takes place. In addition to being densely connected to itself, the cortex is also connected to the thalamus. Various types of connections can be found between the thalamus and cortex layers I, IV, and VI. Even beyond this, layers V and VI are connected to other regions such as the brain stem.

The number of neurons that connect the cortex to itself far outweigh the number

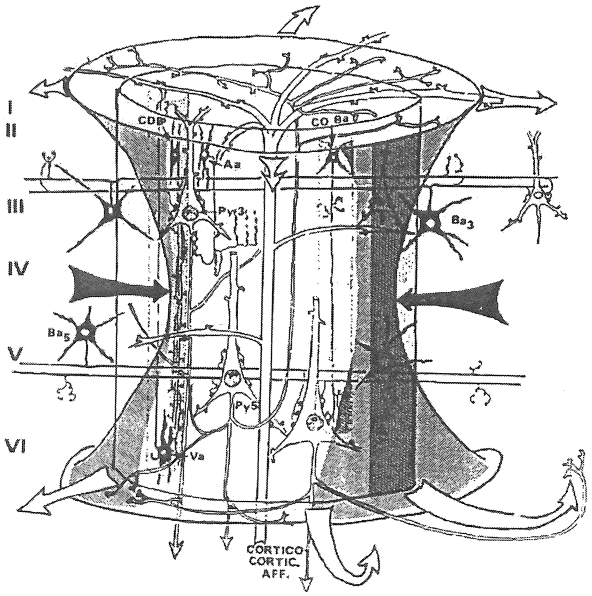

Figure 2.4: Representation of a cortical column. The white arrows show excitatory (intracortical and corticocortical) connections, and the black arrows show inhibitory. The hourglass shape shows the tendency for excitation to spread to neighbouring columns through layers I and VI, while inhibitory influence is localized to the interior layers. *Used with permission from Nunez, 2006 [32].*

that connect it to other parts of the brain. This is typically used as a modelling argument for studying models of an isolated cortex, with the possibility of extraneous input. The use of this argument must be done with care, however, as a few synchronous signals can be much more influential than a large number of asynchronous ones. Thus, sparse synchronized input from other parts of the brain may be important.

However, experiments such as those done by Gebber et al. [14], have demonstrated that the cortex is not just a slave to some sub-cortical pacemaker, and that it must be capable of sustained deterministic oscillations. Whether the circumstances for these oscillations can be met by looking at just an isolated cortex, or if mutual coupling to another structure, i.e., the thalamus, is needed is still an open question.

2.1.4 Towards measurement

Measuring temporally precise electrical activity of the human cortex is restricted to a few methods, if we limit ourselves to non-invasive measurements. The two most commonly used methods are electroencephalography (EEG), and magnetoencephalography (MEG).

EEG relies on measuring the electric fields by using electrodes on the scalp and, under some circumstances, within the cranium. The benefits of using this are that it is relatively cheap and easy to get measurements of electrical activity in the cortex with high temporal resolution. As the EEG is connected to the scalp, any signals

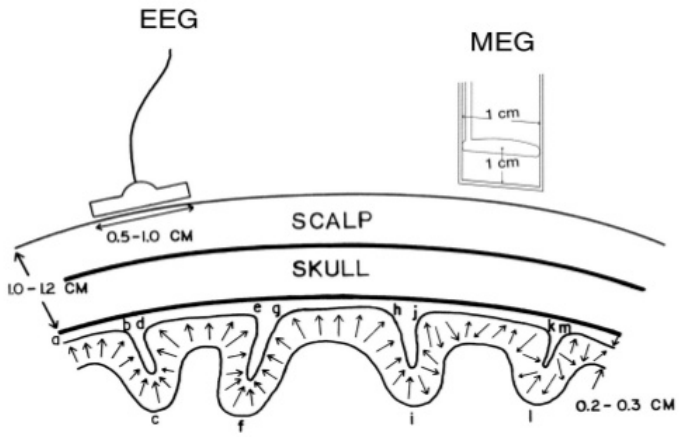

Figure 2.5: Dipole layers in the cortex. Signals must pass through CSF, skull, and scalp before being picked up by EEG or MEG. *Used with permission from Nunez, 2006 [32].*

measured are filtered through the various layers of the human cranium. This filtering can be somewhat taken into account with n-sphere models, which treat $n-1$ layers of tissue with distinct electrical properties between the cortical surface and the scalp. Some common choices are the 3-sphere (brain, skull and scalp) and the 4-sphere (brain, cerebrospinal fluid (CSF), skull, and scalp). These are approximate models, both geometrically and electrically, of the human head. While more precise geometrical information can be obtained for a given subject, the electrical properties of the tissues are more difficult to obtain on a person to person basis, and still must be approximated. Due to the fact that the relative permittivity of biological tissues varies greatly [32], small unknowns in the electrical/geometrical properties produce large variation in the electrical field, making it a difficult task to relate the electrode measurements to the underlying electrical activity with high confidence.

MEG relies on measuring magnetic fields using magnetometers outside of the head. The magnetic fields are generated by small currents within the columns of the neocortex. The main benefit of MEG is that it can provide measurement of electrical activity with the same temporal resolution of the EEG, and can give a much higher spatial resolution. The reason for this is that the relative magnetic permeability of biological tissues (in particular, the CSF, skull, and scalp) are very similar, effectively removing some of the unknown that is inherent in the EEG measurements [32].

The currents within the cortex are aligned mostly with the columns, i.e., a firing neuron produces a potential difference between the soma and the tip of the axon [32]. Since the axons of pyramidal cells are, for the most part, perpendicular to the local cortical surface, this translates into currents that are perpendicular as well.

The EEG is most sensitive to currents that are perpendicular to the scalp. The reason for this becomes clear when one considers the electric potential of a current dipole [20], and makes the connection that EEG is measuring such an electric po-

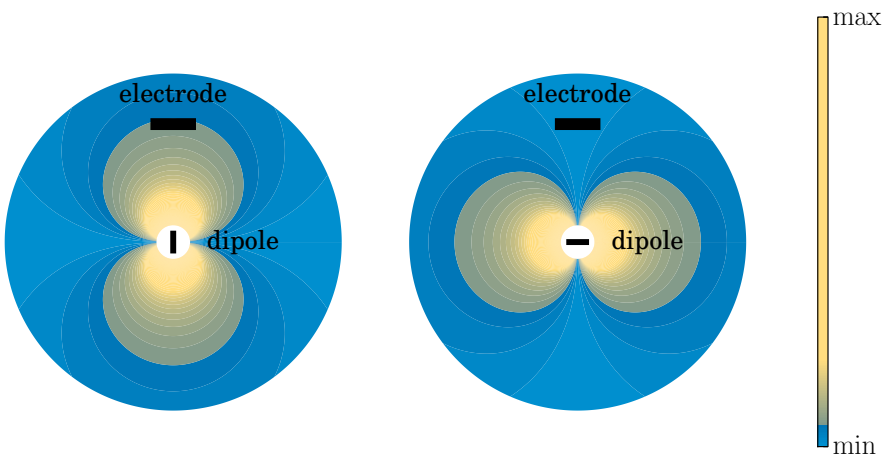

Figure 2.6: Power of the electric field for ideal current dipoles. This is proportional to $\cos^2\theta$ where θ is the angle between the dipole alignment and the position vectors [20]. *Left*: Dipoles aligned perpendicular to the scalp (in crowns of gyri) Contribute largely to electrode measurements at the scalp. *Right*: Dipoles aligned parallel to the scalp (in superficial sulci) do not contribute much to electrode measurements at the scalp.

tential. The potential is proportional to $\cos\theta$, with θ the relative angle between the dipole alignment and the position vectors, maximizing when these are parallel or antiparallel as seen in Figure 2.6. Thus, EEG readings are primarily the result of electrical activity in the crowns of the gyral surfaces as seen in Figure 2.5. Currents found in the columns of sulci are closer to parallel with the scalp. On top of the fact that this orientation produces weaker electric fields at the scalp, the fields generated from neighbouring sulcal walls tend to cancel out due to the geometry [32]. With all of this considered, the geometry of the cortical surface and the spreading of signals in the scalp, it turns out that for a discernible signal to appear in the EEG, it is required that about 6 cm^2 of synchronous activity must be occurring in the cortical gyri. This means that from scalp EEG readings alone, we are not able to resolve the dynamics of the cortex at length scales smaller than this.

The MEG is most sensitive to activity in superficial sulci of the cortex. The reason, again, comes from electromagnetic theory. Considering a magnetic field generated by a current dipole, the power of the field is proportional to $\sin^2\theta$, where θ is the relative angle between the dipole alignment and the position vectors. The power is thus maximum in the $\theta = \pm\pi/2$ direction, i.e., perpendicular to the alignment of the current. This is visualized in Figure 2.7, showing that the strongest magnetic field measurements should come from currents aligned horizontal to the scalp, i.e., in the column in a sulcus.

It is beneficial to view measurement of EEG and MEG as complementary, combining both to get the best possible (non-invasive) view of the electrical activity within the cortex. For example, Aydin et al. recently show how the combination of EEG and

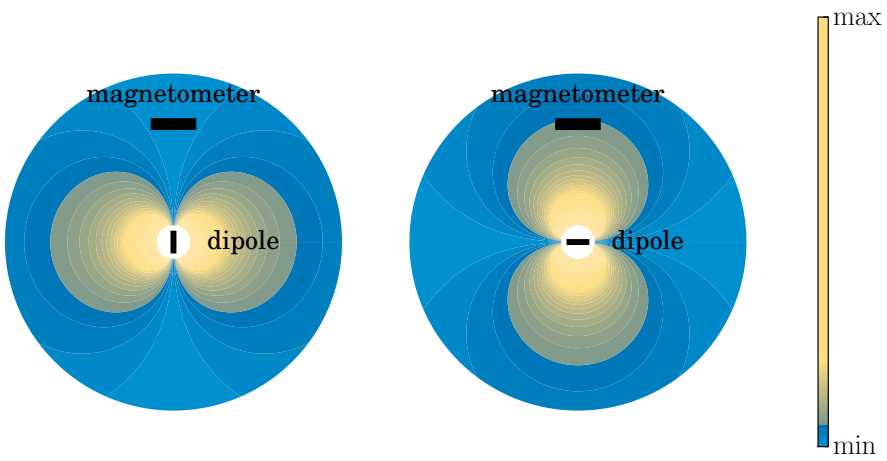

Figure 2.7: Power of the magnetic field for ideal current dipoles. This is proportional to $\sin^2\theta$ where θ is the angle between the dipole alignment and the position vectors [20]. *Left*: Dipoles aligned perpendicular to the scalp (in crowns of gyri) do not contribute much to magnetometer measurements at the scalp. *Right*: Dipoles aligned parallel to the scalp (in superficial sulci) contribute most to magnetometer measurements at the scalp.

MEG measurements can permit more conclusive results for source localization than either of the single methods alone [2].

2.1.5 EEG rhythms

When scalp EEG measurements are performed, the temporal dynamics are typically transformed to frequency space. In frequency space, different names are given to different frequency bands. In particular, there are five major divisions into which readings are binned: delta, theta, alpha, beta, and gamma in increasing order, displayed in Table 2.1.

The relative power in each of these bands at different locations of the brain can

Band	Frequency range
delta, δ	$<$ 4 Hz
theta, θ	4 - 8 Hz
alpha, α	8 - 13 Hz
beta, β	13 - 20 Hz
gamma, γ	$>$ 20 Hz

Table 2.1: The 4 major divisions in brain activity readings.

correlate with different aspects of consciousness. For example, the alpha band typically has the largest peak power over the occipital lobes when the subject is in an eyes closed resting state. This alpha peak disappears when the eyes are opened, or when the subject sets their focus to some cognitive task.

Alpha band and the lower frequencies are often the focus of scalp EEG readings. The reason for this is because of the nature of power dissipation through the skull and scalp. The resistive properties of these tissues effectively lead to a low pass filter, attenuating the higher frequencies more so than the lower. Oscillations with frequencies in the higher bands can be measured, but because of the low pass filtering, they can be seen at the scalp only when relatively large regions of the cortex are synchronously active.

Models for the electrical activity of the cortex are often not formulated at as coarse of a scale as the scalp EEG reads. It is instead typical to see models developed at the length scale of local field potentials (LFP), which can be measured only from within the cranium. LFP measures the combined activity of many dendrites at a submillimetre scale [21]. The benefit of modelling at this scale is that it is intermediary between our network understanding of neural connections and the non-invasive measurement discussed above.

It is this scale that neural fields aim to model, and so the next section will proceed with prescribing what constitutes a neural field.

2.2 Neural field models

This section will introduce the mathematics used in defining neural field models. We begin by writing a neural population as an averaged view of simple neurons, and continue by extending that with delayed spatial connections. In this progression, the relation of presynaptic firing rates to postsynaptic potentials is done in a semi-rigorous manner, with the spatiotemporal axonal connectivity added in a more heuristic way. The result is a specific combination of integrals over space and time which can model a spatially extended neural population in an averaged sense. The combination can be used to construct more complicated models involving multiple populations. The derivation here is performed from the viewpoint of postsynaptic potentials. Since postsynaptic potential is linearly proportional to the dendritic current [32], the form of the resulting operator can be applied to either postsynaptic current or potential.

The combination of integrals will then be used to construct two separate models for neural activity. The first is the most simple model involving a single population with input from an external source. The second involves two populations, and considers the soma membrane potential dynamics in addition to the postsynaptic potentials. We write this second model, Liley's model, in a more general form than it was originally derived, but make note of the explicit assumptions that lead to the partial differential equation (PDE) model of the original paper [26].

2.2.1 A brief history of neural masses

The idea that we can treat large assemblies of neurons with continuum variables seems to be first introduced by Beurle in the 1950s [3], with slight modification later by Griffith [16, 17]. These initial attempts were focused on describing the generation and propagation of large scale activity in networks of excitatory neurons with the continuum variables commonly referred to as *synaptic fields*. The models are most simply expressed through integro-differential equations (IDEs). In the 1970s, Wilson and Cowan [37, 38] extended Beurle's work to incorporate inhibitory neurons and refractory (recovery) periods as well. The addition of refractoriness can be important, since neurons are unable to fire continuously. Dynamical analysis at time scales near this refractory period ($\sim$ 1 ms) will depend heavily on this.

An important extension from Wilson and Cowan was made shortly after by Nunez [31]. Where the IDE model of Wilson and Cowan essentially contained an infinite propagation speed of the signals, Nunez's model incorporated a propagation speed in terms of a spatiotemporal lag in the integral kernel. This was analyzed for a single population model.

From here, Amari [1] started to look at pattern formation under natural assumptions for connectivity and firing functions. Amari considered models with lateral inhibition, i.e., local excitation and long range inhibition. I note here that this is a feature of some neural systems, such as that of the retina, but it is clearly different from the view of the cortex presented in Figure 2.4.

It was also around this time that Freeman published a text on the role of mesoscopic modelling in neural systems [12]. While much of Freeman's work at the time was based on linear models (i.e., motivated by electromagnetic theory), he has played an important role in the development of new approaches to the problem of relating continuous models to experimental data [13].

These seminal works on neural fields provided a basis for many years of research, during which the focus was mostly on qualitative behaviour of these models. Dynamic behaviour typically present are spatially and temporally periodic patterns [10], localized activity [22, 25], and travelling waves [34]. A very cohesive review of the dynamics of neural fields is presented in short by Coombes [8, 9], and more recently in long by Bressloff [5].

In 2001, Liley introduced a modified model of the cortex [26]. The goal here was to create a physiologically paramaterized extension of Wilson and Cowan type models. The main motivation for this extension is that the previous models focused on fields that were first order in time. When considering two interacting populations (neglecting space), this does not allow for the development of chaotic solutions. This also means that the linearized equations, when driven by white noise, will only be capable of producing a single resonance peak. Chaos and multiple spectral peaks are seen in EEG [14], so perhaps a model should exist that allows for these features.

Liley's model treats excitatory and inhibitory populations separately, based on the claim that most of the neurons in the cortex are specialized (made at the end of section 2.1.2) and chooses to model the average soma membrane potential of each population in addition to the postsynaptic potentials generated by the synaptic coupling between

them.

2.2.2 Neural field components

There are three main components that form the basis of neural field modelling,

1. Synaptic coupling,
2. Firing (transfer) functions, and
3. Spatiotemporal connectivity.

From these, models can be created that vary from simple activity models, taking the form of a single scalar equation, to models with multiple populations which can also include additional dynamics for membrane potentials.

Synaptic coupling

First, we take the postsynaptic potential to be the variable $V(t)$, $t \geq 0$. Then we define $h(t)$ to be the postsynaptic response to a single incoming incoming pulse, i.e., $V(t) = h(t)$ for a single (delta-function) input at time zero. If we now consider a train of incoming delta-function pulses as $P(t)$, then the postsynaptic response will be a convolution of $h(t)$ with this train,

$$V(t) = \int_{-\infty}^{t} \mathrm{d}\tau \, h(t-\tau)P(\tau).$$

Experimental studies, such as those performed by Freeman [12], have shown this to be a good model for single neurons, and in fact, network models of neural activity (like in the network simulator NEST [15] or the Blue Brain project [27]) employ this view for their individual elements.

Considering a neural population now, with various types of synapses, various dendrites, and multiple pulse trains, the average postsynaptic potential $\bar{V}(t)$ in response to the average population firing rate $\bar{P}(t)$ will behave in a similar manner,

$$\bar{V}(t) = \int_{-\infty}^{t} \mathrm{d}\tau \, \eta(t-\tau)\bar{P}(\tau), \tag{2.2.1}$$

with $\eta(t)$ representing population response to an average pulse rate. While the time response of a population of synapses may differ to that of a single neuron, it may have the same functional form with just different parameters [12, 39]. To simplify notation, the temporal convolution of Eq. (2.2.1) is written as the operator $*$,

$$\left(\eta * \bar{P}\right)(t) = \int_{-\infty}^{t} \mathrm{d}\tau \, \eta(t-\tau)\bar{P}(\tau). \tag{2.2.2}$$

This forms a solid base for modelling a neural population, but it is not closed in the sense that it relies on some average quantity being known. That is, knowing the

average population firing rate, we can determine the average postsynaptic potential, and vice versa. Closing the model requires another (independent) way of relating these quantities.

Firing functions

To relate the number of firing neurons (i.e., the average firing rate) to the average postsynaptic potential of a closed population, we will start from a simple model of a single neuron with a single dendrite, the so-called McCulloch-Pitts model [28]:

$$P(t) = S_{max}\Theta\big(V(t) - V_{th}\big) = \begin{cases} 0, & V(t) < V_{th} \\ S_{max}, & V(t) > V_{th} \end{cases}, \tag{2.2.3}$$

and follow a similar argument to that presented in Hutt & Atay [19]. Here, Θ is the Heaviside step function, and V_{th} is a threshold postsynaptic potential. This simple model says that if a neuron's postsynaptic potential is above a certain value, then that means it is receiving pulses at a fixed rate S_{max}. Adding to this, we can consider a distribution of dendrites on the neuron with different thresholds, $D(V_{th}, t)$. This distribution can, in general, change in time to account for refractory periods of the neuron. Incorporating this, a neuron with dendrites distributed according to D will have a firing rate given by

$$P(t) = \int_{-\infty}^{\infty} \mathrm{d}V_{th}\, D(V_{th}, t) S_{max}\Theta\big(V(t) - V_{th}\big).$$

Next we consider a population of neurons with postsynaptic potentials that follow a distribution about its average $\rho(V - \bar{V}(t))$. The expected firing rate of this population can be expressed

$$P(t) = \int_{-\infty}^{\infty} \mathrm{d}V\, \rho(V - \bar{V}(t)) \int_{-\infty}^{\infty} \mathrm{d}V_{th}\, D(V_{th}, t) S_{max}\Theta\big(V - V_{th}\big),$$

with V now representing the randomly distributed potentials at time t.

To proceed, we average the pulse activity over a time scale Δt, assuming that the postsynaptic potentials vary on a time scale greater than this,

$$\begin{aligned} \bar{P}(t) &= \frac{1}{\Delta t} \int_{t}^{t+\Delta t} \mathrm{d}\tau\, P(\tau) \\ &\approx \int_{-\infty}^{\infty} \mathrm{d}V\, \rho(V - \bar{V}(t)) \int_{-\infty}^{\infty} \mathrm{d}V_{th}\, \bar{D}(V_{th}, t) S_{max}\Theta\big(V - V_{th}\big). \end{aligned}$$

The argument in the Heaviside function can be used, and the limits of integration adapted, and a general expression for the average firing rate of the population is obtained

$$\bar{P}(t) = S_{max} \int_{-\infty}^{\infty} \mathrm{d}V\, \rho(V) \int_{-\infty}^{V+V(t)} \mathrm{d}V_{th}\, \bar{D}(V_{th}, t).$$

If we consider $\bar{D}$ to be constant in time, $\bar{D}(V_{th}, t) = \bar{D}(V_{th})$ then we can rewrite the average firing rate in terms of the postsynaptic potential, calling it the *firing function*

$$S[\bar{V}(t)] = S_{max} \int_{-\infty}^{\infty} \mathrm{d}V\, \rho(V) \int_{-\infty}^{V+\bar{V}(t)} \mathrm{d}V_{th}\, \bar{D}(V_{th}). \tag{2.2.4}$$

This closes the model, Eq. (2.2.1), as we can now write

$$V(t) = \eta * S \circ V(t) \tag{2.2.5}$$

Now, if we assume a normal distribution of postsynaptic potentials,

$$\rho(V) = \frac{1}{\sigma_{PSP}\sqrt{2\pi}} \exp\left(-\frac{V^2}{2\sigma_{PSP}^2}\right),$$

and a normal distribution of synapses about an average threshold $\bar{V}_{th}$,

$$D(V_{th}) = \frac{1}{\sigma_{syn}\sqrt{2\pi}} \exp\left(-\frac{(V_{th} - \bar{V}_{th})^2}{2\sigma_{syn}^2}\right),$$

then the firing function takes the form

$$S(V) = \frac{S_{max}}{2}\left(1 + \mathrm{erf}\left(\frac{V - \bar{V}_{th}}{\sqrt{2}\sigma}\right)\right), \tag{2.2.6}$$

with erf being the Gaussian error function, and $\sigma^2 = \sigma_{PSP}^2 + \sigma_{syn}^2$.

This process of going from a single McCulloch-Pitts neuron to population firing function is displayed in Figure 2.8. While Eq. (2.2.6) holds exactly for normally distributed statistics, it is generally replaced with another sigmoidal form that roughly has the same shape. This is acceptable because the assumption on the dendrite distribution is weak. Were it replaced with some other distribution, the exact equation would not hold, but since S is essentially a scaling of cumulative distribution functions, the sigmoidal shape should remain.

Spatiotemporal connectivity

The previous two subsections have made no mention of the spatial extent of the neural population, aside from the dynamical equations being locally averaged over cortical columns. Now we introduce a synaptic coupling strength w which can be either positive, representing dominance of excitatory synaptic connections, or negative, representing dominance of inhibitory synapses

$$\bar{V}(t) = w\,\eta * S \circ \bar{V}(t).$$

This now allows us to consider continuous spatial coupling of neural populations. Taking our averaged postsynaptic potential to be a function of both space and time, $\bar{V}(\mathbf{x}, t)$, $x \in \Omega$, we extend the coupling strength to be a function of two spatial

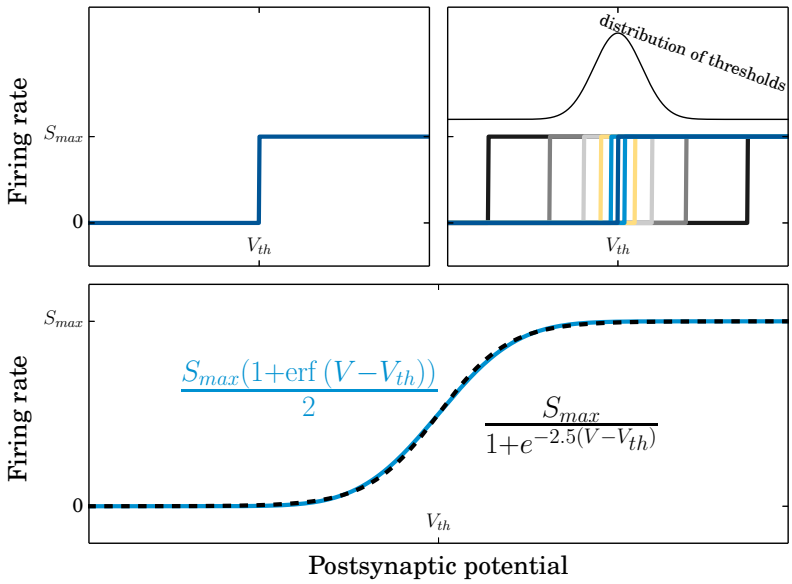

Figure 2.8: *Top left:* McCulloch-Pitts model for a single neuron. *Top right:* Many McCulloch-Pitts neurons with firing thresholds distributed according to a normal distribution. *Bottom:* Effective firing function for a normally distributed population of McCulloch-Pitts neurons (Gaussian error function) compared to a sigmoid with a simpler functional form.

coordinates $w(\mathbf{x}, \mathbf{x}')$, from source $\mathbf{x}'$ to destination $\mathbf{x}$. Thus, the average postsynaptic potential at position x can be taken as a sum over all of the source positions in the domain

$$\bar{V}(\mathbf{x}, t) = \eta * \int_{\Omega} \mathrm{d}^n x'\, w(\mathbf{x}, \mathbf{x}') S \circ \bar{V}(\mathbf{x}', t)$$

noting that n is the spatial dimension of Ω.

This model says that the communication between all neurons within the domain is instantaneous. This is physically not plausible, so a temporal delay that is dependent on source and destination locations, $s(\mathbf{x}, \mathbf{x}')$, is introduced

$$\begin{aligned}\bar{V}(\mathbf{x}, t) &= \eta * \int_{\Omega} \mathrm{d}^n x\, w(\mathbf{x}, \mathbf{x}') S \circ \bar{V}(\mathbf{x}', t - s(\mathbf{x}, \mathbf{x}')) \\ &= \eta * \int_{-\infty}^{\infty} \mathrm{d}t' \int_{\Omega} \mathrm{d}^n x' \underbrace{w(\mathbf{x}, \mathbf{x}')\delta(t - t' + s(\mathbf{x}, \mathbf{x}'))}_{K(\mathbf{x}, \mathbf{x}', t - t')} S \circ \bar{V}(\mathbf{x}', t'),\end{aligned}$$

with $\delta(\cdot)$ the Dirac delta function. The physical interpretation of this when we consider a constant axonal transmission speed c for the entire field is displayed in Figure 2.9. Writing the equation with the delta function leads to the notion of spatiotemporal connectivity

$$K(\mathbf{x}, \mathbf{x}', t) = w(\mathbf{x}, \mathbf{x}')\delta\left(t + s(\mathbf{x}, \mathbf{x}')\right), \tag{2.2.7}$$

coupling points in space and time.

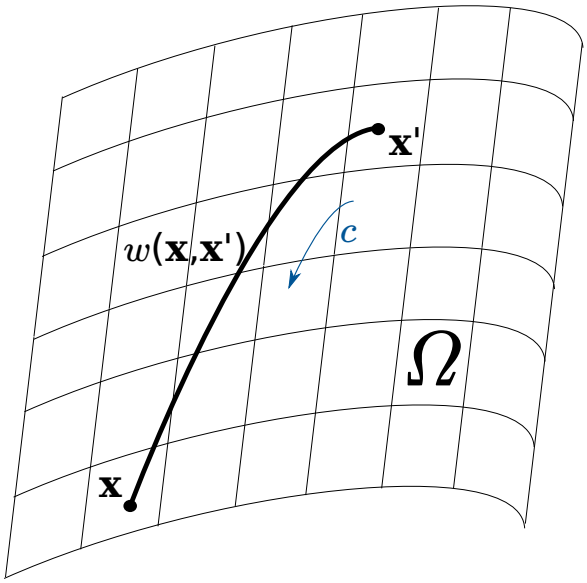

Figure 2.9: View of spatiotemporal connectivity on 2D domain Ω. Neurons at $\mathbf{x}'$ are connected to neurons at $\mathbf{x}$ with coupling strength $w(\mathbf{x}, \mathbf{x}')$. For signals propagating with a constant axonal speed c, the influence of this connection is delayed by $s(\mathbf{x}, \mathbf{x}') = \|\mathbf{x} - \mathbf{x}'\|/c$.

With the spatiotemporal connectivity, we define the spatiotemporal integral operator, $\otimes$, as

$$(K \otimes g)(\mathbf{x}, t) = \int_{-\infty}^{\infty} \mathrm{d}t' \int_{\Omega} \mathrm{d}x_1' x_2' \, K(\mathbf{x}, \mathbf{x}', t - t') \, g(\mathbf{x}', t') \,, \tag{2.2.8}$$

leading to a very concise notation for a model of the averaged postsynaptic potential

$$\bar{V}(t) = \eta * K \otimes S \circ \bar{V}(t).$$

This is the specific combination of integrals that so often arises in neural field modelling,

$$\eta * K \otimes S\circ \tag{2.2.9}$$

being able to describe elements in the models from Amari [1] to that of Liley [26].

2.3 Scalar neural field

The single equation IDE,

$$u(\mathbf{x}, t) = \eta * \big(K \otimes S \circ u(\mathbf{x}, t) + p\big). \tag{2.3.1}$$

This equation has shown up in many papers, originating back to Amari in 1977 [1] who considered it in one spatial dimension without the presence of delays, $s(\mathbf{x}, \mathbf{x}') = 0$.

Since there is not much more to say about this model that has not been men-

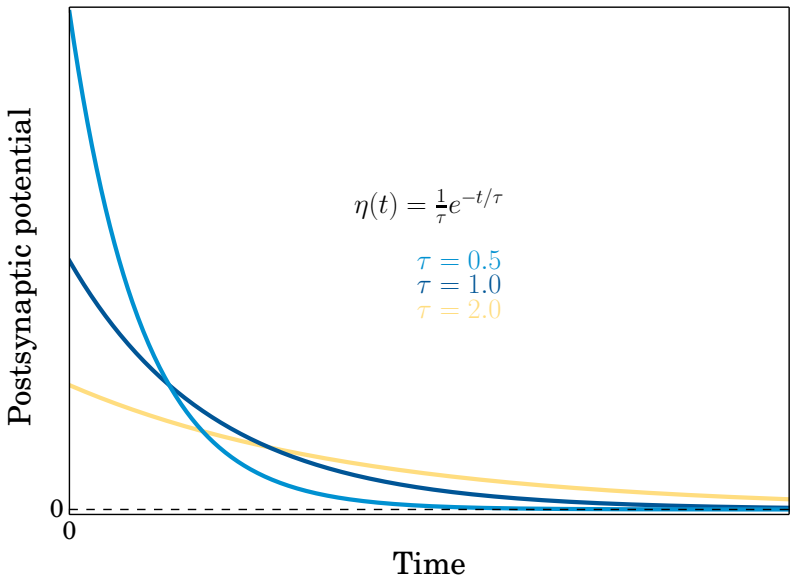

Figure 2.10: The postsynaptic potential response $\bar{V}(t)$ of neurons with a single exponential time scales in response to a delta function input (i.e., a pulse). These are the solution to Eq. (2.2.1) with $\bar{P}(t) = \delta(0)$. Note that the rise of this response is instantaneous, which is an unphysical feature.

tioned in the component derivations above, we give some specific instances of relevant components that will be analyzed in the coming chapter.

2.3.1 Specific components

For the firing function, work in this thesis makes use exclusively of sigmoids of the form

$$S(x) = \frac{S_{max}}{1 + e^{-C(x-\theta)}}. \tag{2.3.2}$$

The three parameters relating to the average firing threshold, θ, the maximal firing rate S_{max} and the steepness at threshold C. A specific instance of this function is plotted in the bottom panel of Figure 2.8, alongside the more formal derivation of the error function sigmoid previously discussed.

For synaptic connectivity, there are a few common choices. The first and most simple is the single exponential time scale

$$\eta(t) = \frac{1}{\tau}e^{-t/\tau}. \tag{2.3.3}$$

This model synapse has been found to work well for individual neurons as in, and also for neural populations.

The main flaw of the single exponential synapse is that the dendritic response in the postsynaptic neuron is inherently discontinuous, seen in Figure 2.10. That

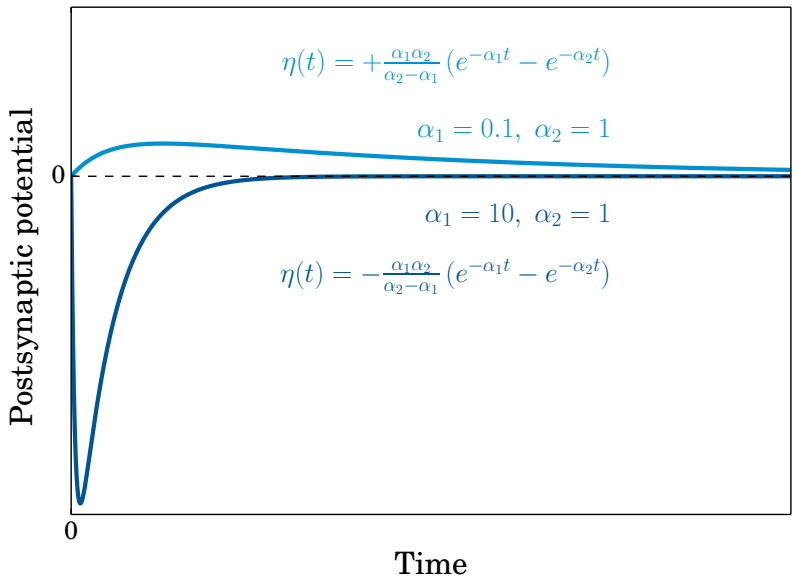

Figure 2.11: The postsynaptic potential response $\bar{V}(t)$ of postsynaptic neurons with two exponential time scales in response to a delta function input (i.e., a pulse). These are the solution to Eq. (2.2.1) with $\bar{P}(t) = \delta(0)$. Note that one is excitatory (weighted with $+$) and the other is inhibitory (weighted with $-$). In neural field models, these weights are incorporated into the connectivity $w(\mathbf{x}, \mathbf{x}')$ rather than the effective synapse $\eta(t)$.

is, when the postsynaptic neurons feel a pulse, the postsynaptic potential instantly jumps to a new value and then exponentially decays. This is unrealistic, as dendritic currents and postsynaptic potentials are observed to rise continuously in response to a single input (Kandel et al. [21] p. 274).

To be able to tune both the rise and fall times of the postsynaptic potential, another exponential time scale can be incorporated into the synapse,

$$\eta(t) = \frac{\alpha_1\alpha_2}{\alpha_2 - \alpha_1}\left(e^{-\alpha_1 t} - e^{-\alpha_2 t}\right). \tag{2.3.4}$$

In Figure 2.11, the dendritic response to an excitatory and an inhibitory synapse with two different parameter sets are plotted to show this.

If we take the synapse with two exponential time scales from Eq. (2.3.4) and let the parameters approach each other in value, $\alpha \equiv \alpha_1 \to \alpha_2$, then we end up with what is called the *alpha function* synapse

$$\eta(t) = \alpha^2 t e^{-\alpha t}. \tag{2.3.5}$$

The alpha function synapse is nice from a modelling point of view because it only has a single parameter which modifies both the rise and the fall of the dendritic response curve. As mentioned earlier, this is closer to reality than the single exponential model. Sometimes however, having both the rise and fall manipulated through a

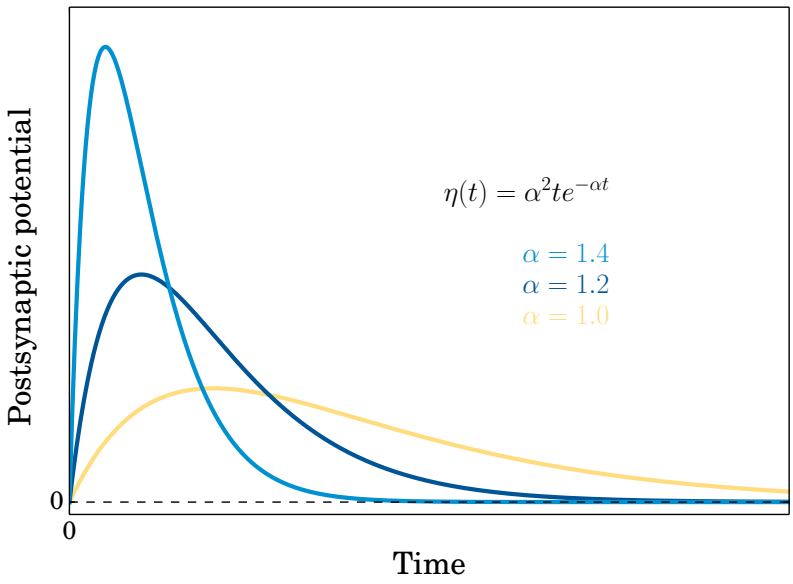

Figure 2.12: The postsynaptic potential response $\bar{V}(t)$ of postsynaptic neurons with the alpha function synapse in response to a delta function input (i.e., a pulse). These are the solution to Eq. (2.2.1) with $\bar{P}(t) = \delta(0)$.

single parameter is not enough, and we must revert back to the double exponential model. This is exactly the case when one wants to parameterize a model to match general anaesthetic agents such as isoflurane that are known to prolong the rise time of inhibitory postsynaptic potential much less than the decay time. Having the two exponential time scales was shown to be necessary by Bojak & Liley [4] to correctly reproduce EEG spectra in Liley's model.

Finally we have the spatiotemporal connectivity. This thesis will exclusively use constant, homogeneous, and isotropic transmission speed throughout. That is, the delay time will always have the form

$$s(\mathbf{x}, \mathbf{x}') = \frac{\|\mathbf{x} - \mathbf{x}'\|}{c}, \tag{2.3.6}$$

with transmission speed c, as in the schematic of Figure 2.9. Taking the limit $c \to \infty$ results in instantaneous communication between any two points, recovering the often studied neural field without delay. This leaves just the connection weight $w(\mathbf{x}, \mathbf{x}')$ to be specified.

Many simplifying assumptions on w can be used for tractable analysis. We can use homogeneous connections

$$w(\mathbf{x}, \mathbf{x}') = w(\mathbf{x} - \mathbf{x}'),$$

implying that the connection weight depends solely on the relative position of $\mathbf{x}$ and $\mathbf{x}'$. Even more restrictive is if the connections are also isotropic

$$w(\mathbf{x} - \mathbf{x}') = w(\|\mathbf{x} - \mathbf{x}'\|),$$

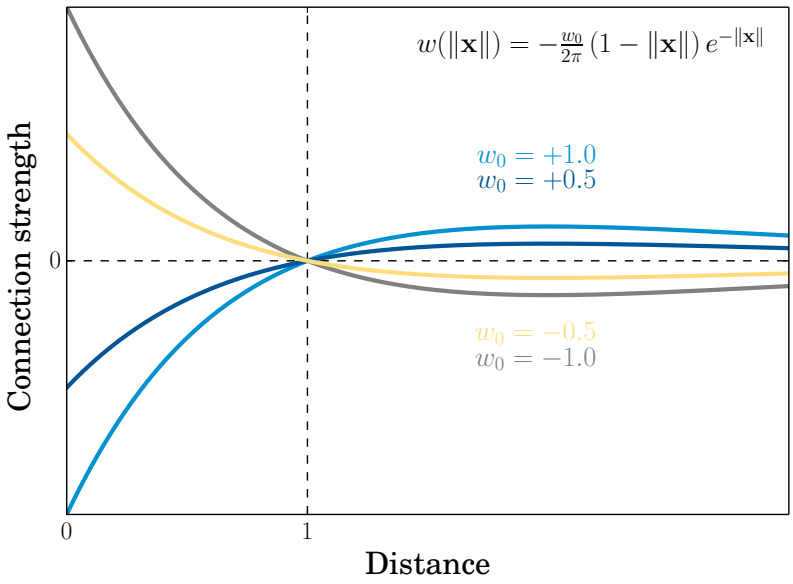

Figure 2.13: Wizard hat connectivity with varying parameter. Positive connection strength indicates dominance of excitatory connections, negative indicates dominance of inhibitory connections. Zero value can either mean there are no connections at that distance or the excitatory an inhibitory perfectly balance. The single parameter w_0 can represent either lateral excitation or lateral inhibition connectivities.

saying that the connection weight only depends on the distance between points $\mathbf{x}$ and $\mathbf{x}'$, not the direction. Analysis presented in the next chapter is done with homogeneous and isotropic connectivities, but extends in a straightforward way if the isotropy condition is relaxed, and for specific symmetries of the connectivity.

A useful property for connectivities is to have excitatory and inhibitory dominance differ with length scale, in accordance with with anatomical observations as in Stepanyants et al. [36]. In two dimensions, the *wizard hat* connectivity

$$w(\mathbf{x}, \mathbf{x}') = -\frac{w_0}{2\pi}\,(1 + \|\mathbf{x} - \mathbf{x}'\|)\, e^{-\|\mathbf{x}-\mathbf{x}'\|}, \tag{2.3.7}$$

is very convenient for demonstrating this. The single parameter can qualitatively model two distinct regimes, lateral inhibition ($w_0 < 0$) and lateral excitation ($w_0 > 0$) connectivities, demonstrated in Figure 2.13.

One thing to note is that while the single parameter is convenient as a model, the distance where the dominance switches from excitation to inhibition (or vice versa) remains one. This is fine in the qualitative sense for a single population model, as the the system can be scaled around this length, but would be problematic with the use of multiple populations with different length scales. Adding additional parameters is one way to proceed, or we can go with something different altogether.

As that something different, we combine two exponentially decaying connectivities with different strengths, different signs, and different length scales to come up with a

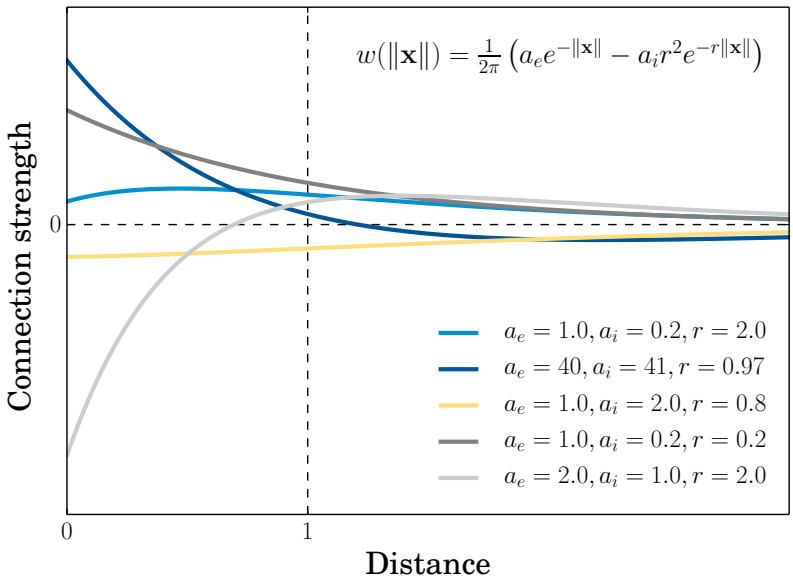

Figure 2.14: Double exponential connectivity with varying parameters. The addition of parameters makes the model more versatile than the single parameter wizard hat.

more robust connectivity

$$w(\mathbf{x}, \mathbf{x}') = \frac{1}{2\pi}\left(a_e e^{-\|\mathbf{x}-\mathbf{x}'\|} - a_i r^2 e^{-r\|\mathbf{x}-\mathbf{x}'\|}\right). \tag{2.3.8}$$

The three parameters in this model are the strength of excitatory connections a_e, strength of inhibitory connections a_i, and a characteristic length scale r. Varying these three parameters can produce the lateral excitation and inhibition connectivities qualitatively similar to the wizard hat, but can also produce purely excitatory and purely inhibitory connectivities that are non-monotonic.

2.4 Liley's neural field model

In 2001, Liley et al. proposed a neural population model combining two neural populations to model the excitatory pyramidal cells and inhibitory pyramidal cells of human neocortex [26]. One major difference from this model compared to the above is that it treats the dynamics of postsynaptic potentials separately from the dynamics of the soma membrane potential.

2.4.1 General form

The main observable of this model is the soma membrane potentials of the two populations, and it is these quantities that leads to the synaptic activity. Thus, firing functions will take, as input, the soma membrane potentials rather than the post-

synaptic potentials that the scalar model did. The dynamics of the postsynaptic potentials otherwise follow the same equations. The dynamics of the soma membrane potentials involve a shifted-inverted mass action coupling to the scaled postsynaptic potentials, and are taken to be purely local.

A general form of the model, with $h_k(\mathbf{x},t)$ being the soma membrane potential of population $k=e,i$ at position $\mathbf{x}$ and time t, and the post synaptic potentials $I_{jk}(\mathbf{x},t)$ of neurons between populations $j=e,i$ and k, can be written

$$\begin{aligned} h_k(\mathbf{x},t) &= \eta_k * \left(h_k^r + \sum_j \frac{h_{jk}^{eq} - h_k(\mathbf{x},t)}{\left|h_{jk}^{eq} - h_j^r\right|} I_{jk}(\mathbf{x},t) \right) \\ I_{jk}(\mathbf{x},t) &= \eta_{jk} * \left(K_{jk} \otimes S_j \circ h_j(\mathbf{x},t) + p_{jk} \right), \end{aligned} \tag{2.4.1}$$

using the temporal and spatiotemporal integral operators defined in Section 2.2.2. Here, the spatiotemporal connectivities and effective synapses have been given subscripts that tell from which population to which population the connection is occurring.

The equation for the soma membrane potentials is interpreted as follows. The η_k represent a temporal convolution kernel for the dynamics of the soma membrane potential of population k. The soma membrane potentials want to relax to their resting membrane potential h_k^r, but are being forced by the postsynaptic potentials. This forcing consists of a mass action coupling between the deviation of membrane potential from its reversal potential, $h_{jk}^{eq} - h_k(\mathbf{x},t)$, normalized by the relative difference between resting and reversal potentials, $\left|h_{jk}^{eq} - h_j^r\right|$, and the postsynaptic potential originating from population j, $I_{jk}(\mathbf{x},t)$.

2.4.2 Specific form of components

To obtain the specific model introduced by Liley et al. [26], we introduce the specific temporal and spatiotemporal connectivity kernels.

For the soma membrane potentials, the η_k have the same form, but different parameters for the time scale τ_k,

$$\eta_k(t) = \frac{1}{\tau_k} e^{-t/\tau_k}. \tag{2.4.2}$$

This is the same as the single exponential synapse that was proposed in Eq. (2.3.3), but when applied here it is more physiologically justified as the soma membrane potential can rise much faster than that of the postsynaptic potentials.

The synaptic convolution kernels for the postsynaptic potentials all have an alpha function form, with differing time scales γ_{jk},

$$\eta_{jk}(t) = \gamma_{jk}^2 t e^{-\gamma_{jk} t}. \tag{2.4.3}$$

As discussed, this is the simplest way of obtaining the proper qualitative behaviour

of the postsynaptic potentials.

The spatiotemporal connectivities are different depending on the source population (first index). The inhibitory population i, representing the interneurons, has only pure local connections written as

$$K_{ik}(\mathbf{x}, \mathbf{x}', t - t') = \exp(1)\Gamma_{ik}\frac{N_{ik}^{\beta}}{2\pi}\delta^2(\mathbf{x} - \mathbf{x}')\delta(t - t'), \tag{2.4.4}$$

with the postsynaptic potential peak amplitude Γ_{ik}, the number of local intracortical synapses N_{ik}^{β} from i to k, and $\delta^2(\mathbf{x}) \equiv \delta(x_1)\delta(x_2)$ the two dimensional delta function.

The excitatory population e, representing the pyramidal cells, does have spatially extending connections in addition to its local connections. The spatiotemporal connectivity kernel has a strange form, with the explanation to follow

$$\begin{aligned} K_{ek}(\mathbf{x}, \mathbf{x}', t - t') = \Gamma_{ek}\Bigg(&\frac{N_{ek}^{\alpha}\Lambda^2}{3\pi}K_0\left(\sqrt{2/3}\,\Lambda\|\mathbf{x} - \mathbf{x}'\|\right)\delta\left(t - t' + \|\mathbf{x} - \mathbf{x}'\|/v\right) \\ &+ \frac{N_{ek}^{\beta}}{2\pi}\delta^2(\mathbf{x} - \mathbf{x}')\delta(t - t')\Bigg)\exp(1). \end{aligned} \tag{2.4.5}$$

In this connectivity, we have:

- K_0, the modified Bessel function of the second kind,
- Γ_{ek}, the postsynaptic potential peak amplitude,
- N_{ek}^{α}, the number of cortico-cortico synapses from e to k,
- Λ, spatial decay scale for connectivity,
- v, axonal transmission speed, and
- N_{ek}^{β}, the number of local intracortical synapses from e to k.

The modified Bessel function of the second kind is used for two reasons: i) it *looks* similar to an exponential, and ii) with all of the other kernels as specified, it permits a PDE formulation of the model when $\Omega = \mathbb{R}^2$. Both of these statements are quantified in Appendix B, with the key being that in this form, the Fourier-Laplace transform is a rational function, which allows the delayed integral to be written as a damped wave equation.

With all of the kernels as specified, we can now write Liley's model in the form in which it was originally presented

$$\begin{aligned} \tau_k\frac{\partial}{\partial t}h_k(\mathbf{x}, t) &= h_k^r - h_k(\mathbf{x}, t) + \sum_j \frac{h_{jk}^{eq} - h_k(\mathbf{x}, t)}{\left|h_{jk}^{eq} - h_j^r\right|}I_{jk}(\mathbf{x}, t) \\ \left(\frac{\partial}{\partial t} + \gamma_{jk}\right)^2 I_{jk}(\mathbf{x}, t) &= \exp(1)\Gamma_{jk}\gamma_{jk}\left[N_{jk}^{\beta}S_j \circ h_j(\mathbf{x}, t) + \phi_{jk}(\mathbf{x}, t) + p_{jk}\right] \\ \left[\left(\frac{\partial}{\partial t} + v\Lambda\right)^2 - \frac{3}{2}v^2\nabla^2\right]\phi_{ek}(\mathbf{x}, t) &= N_{ek}^{\alpha}v^2\Lambda^2 S_e \circ h_e(\mathbf{x}, t) \\ \phi_{ik}(\mathbf{x}, t) &= 0, \end{aligned} \tag{2.4.6}$$

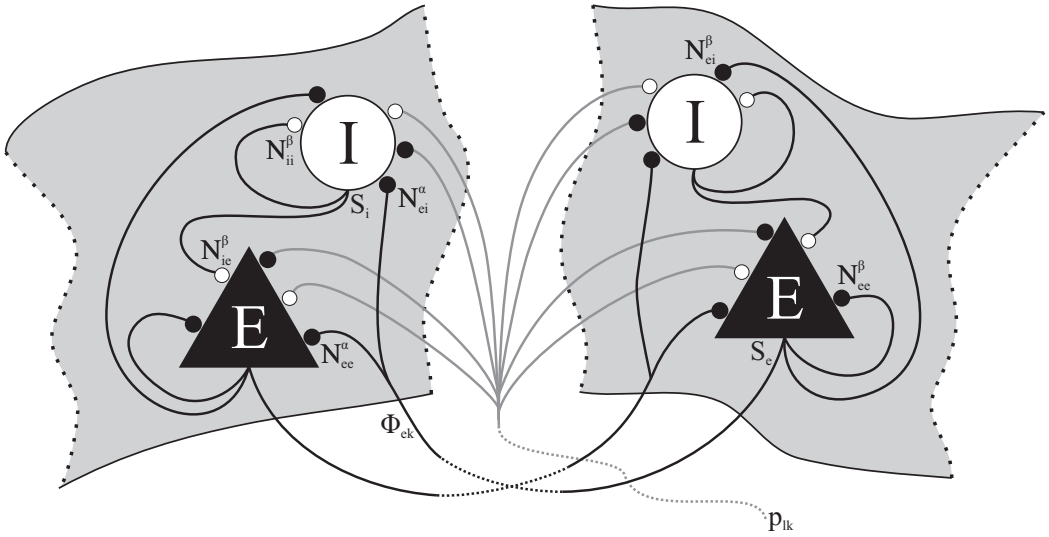

Figure 2.15: A schematic view of Liley's model, Eq. (2.4.6). This shows the synaptic coupling between the two populations. Inhibitory synapses are coloured white, and excitatory coloured black. The excitatory population has direct coupling to other regions in space, while the inhibitory population has only local. External input to this model can be excitatory or inhibitory, and can act on either of the excitatory or inhibitory populations. *Used with permission from Frascoli, 2011 [11].*

with the firing functions written as our sigmoid

$$S_k(x) = S_k^{max}\left[1 + \exp\left(-\sqrt{2}\frac{x-\mu_k}{\sigma_k}\right)\right]^{-1}, \tag{2.4.7}$$

maximal firing rate, threshold, and variance parameters dependent on population.

The schematic view of everything discussed above is found in Figure 2.15, and a quick summary of the parameters is given in Table 2.2.

2.5 Summary

The state variables in the two different models have physiologically relevant interpretations. As a quick reminder, they are restated here.

u in the scalar neural field is thought of as a locally averaged soma membrane potential for a single population that can contain both excitatory and inhibitory synapses. This local average is considered to be at the scale of micro to macrocolumns.

h_j in Liley's model refer to locally averaged membrane potentials of separate populations that are purely excitatory ($j = e$) or inhibitory ($j = i$) in nature. The I_{jk} have the same interpretation as the u in the scalar field, but now may be different depending on the origin $j = e, i$ and destination $k = e, i$. Again, the local averages are considered to be at the scale of micro to macrocolumns.

The macrocolumn scale at which these models are relevant is most comparable to data acquired by LFP measurements [21]. They can be compared to the more coarse

Parameter	Definition	Minimum	Maximum	Units
h_e^r	resting excitatory membrane potential	-80	-60	mV
h_i^r	resting inhibitory membrane potential	-80	-60	mV
τ_e	passive excitatory membrane decay time	5	150	ms
τ_i	passive inhibitory membrane decay time	5	150	ms
h_{ee}^{eq}	excitatory reversal potential	-20	10	mV
h_{ei}^{eq}	excitatory reversal potential	-20	10	mV
h_{ie}^{eq}	inhibitory reversal potential	-90	$h_k^r - 5$	mV
h_{ii}^{eq}	inhibitory reversal potential	-90	$h_k^r - 5$	mV
Γ_{ee}	EPSP peak amplitude	0.1	2.0	mV
Γ_{ei}	EPSP peak amplitude	0.1	2.0	mV
Γ_{ie}	IPSP peak amplitude	0.1	2.0	mV
Γ_{ii}	IPSP peak amplitude	0.1	2.0	mV
γ_{ee}	EPSP characteristic rate constant‡	100	1000	s^{-1}
γ_{ei}	EPSP characteristic rate constant‡	100	1000	s^{-1}
γ_{ie}	IPSP characteristic rate constant‡	10	500	s^{-1}
γ_{ii}	IPSP characteristic rate constant‡	10	500	s^{-1}
N_{ee}^{α}	no. of cortico-cortical synapses, target excitatory	2000	5000	–
N_{ei}^{α}	no. of cortico-cortical synapses, target inhibitory	1000	3000	–
N_{ee}^{β}	no. of excitatory intracortical synapses	2000	5000	–
N_{ei}^{β}	no. of excitatory intracortical synapses	2000	5000	–
N_{ie}^{β}	no. of inhibitory intracortical synapses	100	1000	–
N_{ii}^{β}	no. of inhibitory intracortical synapses	100	1000	–
v	axonal conduction velocity	100	1000	$\mathrm{cm\,s}^{-1}$
$1/\Lambda$	decay scale of cortico-cortical connectivity	1	10	cm
$S_e^{\max}$	maximum excitatory firing rate	50	500	s^{-1}
$S_i^{\max}$	maximum inhibitory firing rate	50	500	s^{-1}
μ_e	excitatory firing threshold	-55	-40	mV
μ_i	inhibitory firing threshold	-55	-40	mV
σ_e	standard deviation of excitatory firing threshold	2	7	mV
σ_i	standard deviation of inhibitory firing threshold	2	7	mV
p_{ee}	extracortical synaptic input rate	0	10000	s^{-1}
p_{ei}	extracortical synaptic input rate	0	10000	s^{-1}

Table 2.2: Meaning and ranges for parameters of Liley's model.

spatial data obtained by EEG & MEG by using spatial blurring filters on the domain of the neural field. Finally, network models of neurons can be spatially and temporally averaged to get space and time scales comparable to the neural field scales.

On that final note, there are a few cases where neural field models can be formally derived from the explicit averaging of network models, such as Brunel & Wang [6], and more recently Laing [24], and Zandt et al. [40]. It is reiterated that the models studied in this thesis do not have a formal equivalence to underlying network models, rather they are semi heuristic in nature.

Bibliography

[1] Amari, S. Dynamics of pattern formation in lateral-inhibition type neural fields. *Biological Cybernetics 27*, 2 (1977), 77–87.

[2] Aydin, U., Vorwerk, J., Dümpelmann, M., Küpper, P., Kugel, H., Wellmer, J., Kellinghaus, C., Haueisen, J., Rampp, S., Stefan, H., and Wolters, C. H. Combined EEG/MEG Can Outperform Single Modality EEG or MEG Source Reconstruction in Presurgical Epilepsy Diagnosis. *PLoS ONE 10*, 3 (2014), e0118753.

[3] Beurle, R. L. Properties of a Mass of Cells Capable of Regenerating Pulses. *Philosophical Transactions of the Royal Society B 240*, 669 (1956), 55–94.

[4] Bojak, I., and Liley, D. Modeling the effects of anesthesia on the electroencephalogram. *Physical Review E 71*, 4 (2005), 1–22.

[5] Bressloff, P. C. Spatiotemporal dynamics of continuum neural fields. *Journal of Physics A 45*, 3 (2012), 033001.

[6] Brunel, N., and Wang, X. J. Effects of neuromodulation in a cortical network model of object working memory dominated by recurrent inhibition. *Journal of Computational Neuroscience 11*, 1 (2001), 63–85.

[7] Chayer, C., and Freedman, M. Frontal lobe functions. *Current Neurology and Neuroscience Reports 1*, 6 (2001), 547–552.

[8] Coombes, S. Waves, bumps, and patterns in neural field theories. *Biological Cybernetics 93*, 2 (2005), 91–108.

[9] Coombes, S. Large-scale neural dynamics: simple and complex. *NeuroImage 52*, 3 (2010), 731–739.

[10] Ermentrout, G. B., and Cowan, J. D. A mathematical theory of visual hallucination patterns. *Biological Cybernetics 34* (1979), 137–150.

[11] Frascoli, F., van Veen, L., Bojak, I., and Liley, D. T. Metabifurcation analysis of a mean field model of the cortex. *Physica D 240*, 11 (2011), 949–962.

[12] Freeman, W. *Mass action in the nervous system*. Academic Press, New York, 1975.

[13] Freeman, W. J. Neurodynamics: An exploration in mesoscopic brain dynamics. In *Perspectives in neural computing*. Springer-Verlag London Berlin Heidelberg, 2000.

[14] Gebber, G. L., Zhong, S., Lewis, C., and Barman, S. M. Human brain alpha rhythm: nonlinear oscillation or filtered noise. *Brain Research 818*, 2 (1999), 556–560.

[15] Gewaltig, M.-O., and Diesmann, M. NEST (Neural Simulation Tool). *Scholarpedia 2*, 4 (2007), 1430.

[16] Griffith, J. S. A field theory of neural nets: I. Derivation of field equations. *Bulletin of Mathematical Biophysics 25* (1963), 111–120.

[17] Griffith, J. S. A field theory of neural nets: II. Properties of the field equations. *Bulletin of Mathematical Biophysics 27* (1965), 187–195.

[18] Hodgkin, A. L., and Huxley, A. F. A quantitative description of membrane current and its application to conduction and excitation in nerve. *The Journal of Physiology 117*, 4 (1952), 500–544.

[19] Hutt, A., and Atay, F. M. Analysis of nonlocal neural fields for both general and gamma-distributed connectivities. *Physica D 203* (2005), 30–54.

[20] Jackson, J. D. *Classical Electrodynamics*, 3 ed. Wiley, New York, 1998.

[21] Kandel, E. R., Schwartz, J. H., and Jessell, T. M. *Principles of Neural Science*. McGraw-Hill, 2000.

[22] Kishimoto, K., and Amari, S. Existence and stability of local excitations in homogeneous neural fields. *Journal of Mathematical Biology 7*, 4 (1979), 303–318.

[23] Koechlin, E., Ody, C., and Kouneiher, F. The architecture of cognitive control in the human prefrontal cortex. *Science 302*, 5648 (2003), 1181–1185.

[24] Laing, C. R. Derivation of a neural field model from a network of theta neurons. *Physical Review E 90*, 1 (2014), 1–5.

[25] Laing, C. R., Troy, W. C., Gutkin, B., and Ermentrout, G. B. Multiple bumps in a neuronal model of working memory. *SIAM Journal on Applied Mathematics 63*, 1 (2002), 62–97.

[26] Liley, D. T. J., Cadusch, P. J., and Dafilis, M. P. A spatially continuous mean field theory of electrocortical activity. *Network Computation in Neural Systems 13*, 1 (2002), 67–113.

[27] Markram, H. The blue brain project. *Nature reviews. Neuroscience 7*, 2 (2006), 153–160.

[28] McCulloch, W. S., and Pitts, W. H. A logical calculus of ideas imminent in nervous activity. *Bulletin of Mathematical Biophysics 5* (1943), 115–133.

[29] Mountcastle, V. Modality and topographic properties of single neurons of cat's somatic sensory cortex. *Journal of Neurophysiology 20*, 4 (1957), 408–434.

[30] Mountcastle, V. B. The columnar organization of the neocortex. *Brain 120*, 4 (1997), 701–722.

[31] Nunez, P. The brain wave equation: A model for the EEG. *Mathematical Biosciences 21* (1974), 279–297.

[32] Nunez, P., and Srinivasan, R. *Electric Fields of the Brain. The Neurophysics of EEG*, 2 ed. Oxford University Press, Oxford, 2006.

[33] Petroff, O. A. C. Book Review: GABA and Glutamate in the Human Brain. *The Neuroscientist 8*, 6 (2002), 562–573.

[34] Pinto, D. J., and Ermentrout, G. B. Spatially structured activity in synaptically coupled neuronal networks: i. traveling fronts and pulses. *SIAM Journal on Applied Mathematics 62*, 1 (2001), 206–225.

[35] Rakic, P. Confusing cortical columns. *PNAS 105*, 34 (2008), 12099–12100.

[36] Stepanyants, A., Martinez, L. M., Ferecskó, A. S., and Kisvárday, Z. F. The fractions of short- and long-range connections in the visual cortex. *PNAS 106*, 9 (2009), 3555–3560.

[37] Wilson, H. R., and Cowan, J. D. Excitatory and Inhibitory Interactions in Localized Populations of Model Neurons. *Biophysical Journal 12*, 1 (1972), 1–24.

[38] Wilson, H. R., and Cowan, J. D. A mathematical theory of the functional dynamics of cortical and thalamic nervous tissue. *Kybernetik 13*, 2 (1973), 55–80.

[39] Wright, J. J. EEG simulation: variation of spectral envelope, pulse synchrony and approximately 40 Hz oscillation. *Biological Cybernetics 76*, 3 (1997), 181–194.

[40] Zandt, B.-J., Visser, S., van Putten, M. J. A. M., and ten Haken, B. A neural mass model based on single cell dynamics to model pathologies. *Journal of Computational Neuroscience 37*, 3 (2014), 549–568.

Chapter 3

Dynamical systems

3.1 Finite dimensional dynamical systems 34
3.1.1 Equilibrium solutions 35
3.1.2 Hopf bifurcation 36
3.1.3 Periodic solutions 38
3.2 Infinite dimensional systems 40
3.2.1 Equilibrium solutions 40
3.2.2 Linear stability 41
3.2.3 Bifurcation from dispersion relation 42
3.3 Bifurcations with symmetry 43
3.3.1 General problem 43
3.3.2 $D_4 \ltimes T^2$ Hopf bifurcation 44
3.4 Continuation 47
3.4.1 General methods 49
3.4.2 Applied to equilibria 51
3.4.3 Applied to bifurcations of equilibria 52
3.4.4 Applied to periodic orbits 53
3.4.5 Applied to continuous dispersion relations 54
3.4.6 Applied to bifurcations of SHE 54
3.5 Summary 56
Bibliography 56

This chapter will focus on presenting the formulations of dynamical systems that will be used throughout the remainder of the thesis. There are two viewpoints that

must be introduced to follow our analysis, that of finite dimensional dynamical systems (i.e., ODEs), and infinite dimensional (i.e., spatially extended and/or delayed) systems. Bifurcations are discussed from the finite dimensional viewpoint. For the infinite dimensional case, the linear stability of perturbations with respect to all possible Fourier wave modes leads to dispersion relations. On the infinite plane, an infinite number of wave modes destabilize simultaneously, corresponding to a degree of freedom in the orientation of the waves. Restricting this orientational freedom to wave modes in two directions orthogonal to each other restricts the dimensionality at bifurcation, allowing for progress to be made through the use of symmetric bifurcation theory.

3.1 Finite dimensional dynamical systems

For the purposes of this thesis, a finite dimensional dynamical system is taken to be a system of ordinary differential equations (ODEs) of the form

$$\begin{aligned} \dot{u} &= f(u,\alpha), \quad u(0) = u_0, \\ \dot{\alpha} &= 0, \end{aligned} \tag{3.1.1}$$

where $u(t) \in \mathbb{R}^n$ represents the state vector at time $t \in [0,\infty)$, and $\alpha \in \mathbb{R}^m$ a vector of parameters, so $f : \mathbb{R}^{n+m} \to \mathbb{R}^n$ and is taken to be *smooth enough* such that any derivatives used below are well defined. This view, the separation of parameters and state, is most useful when there are aspects of the system that do not change in time, or change on a time scale that is much longer than the time scales that we are interested in studying.

Another way to view such a dynamical system is via the flow, ϕ. A finite dimensional dynamical system on $\mathbb{R}^N$ is a continuously differentiable function $\phi : \mathbb{R}^N \times \mathbb{R} \to \mathbb{R}^N$ such that $\phi(X,t)$ satisfies

1. $\phi(X,0) : \mathbb{R}^N \to \mathbb{R}^N$ is the identity function $\phi(X,0) = X$
2. The composition $\phi(X,t) \circ \phi(X,s) = \phi(X,t+s)$ holds for each $t,s \in \mathbb{R}$

The connection to the ODEs in Eq. (3.1.1) is that the flow satisfies the equation, i.e., $\partial_t \phi(u,t) = f(\phi(u,t))$. With this equivalence, 1 is satisfied by the initial condition, and 2 is satisfied if f satisfies the existence and uniqueness criteria for ODEs, thus the definition holds with $N = n+m$ and $X = [u,\alpha]^T$. The reason for including this definition is because the discussion of aspects of periodic solutions follow more naturally from the viewpoint of a flow. Specifically, both the computation and stability analysis of periodic solutions make use of the differential of the flow with respect to the initial state.

3.1.1 Equilibrium solutions

An equilibrium is a solution to Eq. (3.1.1) that does not change in time. That is, it satisfies

$$f(u, \alpha) = 0 \tag{3.1.2}$$

Without loss of generality, we can assume a solution to eq. (3.1.2) to be at $u = 0$, $\alpha = 0$. We Taylor expand the vector function $f(u, 0)$ as

$$f(u, 0) = Au + \frac{1}{2}B(u, u) + \frac{1}{6}C(u, u, u) + O\left(||u||^4\right), \tag{3.1.3}$$

with elements of the different order terms

$$A_{ij} = \partial_{u_j} f_i, \tag{3.1.4a}$$

$$B_i(u, v) = \sum_{j,k} \left(\partial_{u_j}\partial_{u_k} f_i\right) u_j v_k, \tag{3.1.4b}$$

$$C_i(u, v, w) = \sum_{j,k,l} \left(\partial_{u_j}\partial_{u_k}\partial_{u_l} f_i\right) u_j v_k w_l, \tag{3.1.4c}$$

for indices $i, j, k = 1 \ldots n$. Partial differentiation is indicated by ∂, with each evaluated at the zero state, i.e.,

$$\partial_{u_j}\partial_{u_k} f_i = \left.\frac{\partial^2 f_i}{\partial u_j \partial u_k}\right|_{u,\alpha=0}.$$

As written, A is thus a matrix, while B and C are vectors.

We can then analyze the linear stability of the equilibrium by looking at the eigenvalues of the Jacobian A. In particular, we can define three subspaces from the eigenvalue equation $(\lambda I - A)\, v = 0$:

- Stable eigenspace $\mathcal{S}$: The subspace spanned by the generalized eigenvectors corresponding to the eigenvalues λ with $\mathrm{Re}\lambda < 0$.
- Center eigenspace $\mathcal{C}$: The subspace spanned by the generalized eigenvectors corresponding to the eigenvalues λ with $\mathrm{Re}\lambda = 0$.
- Unstable eigenspace $\mathcal{U}$: The subspace spanned by the generalized eigenvectors corresponding to the eigenvalues λ with $\mathrm{Re}\lambda > 0$.

Depending on the dimensionality of these subspaces, we describe the equilibrium in one of three ways: An equilibrium solution is called *stable* if $\dim \mathcal{S} = \dim A$. It is called *unstable* if $\dim \mathcal{U} > 0$, and it is called *neutrally stable* if $\dim \mathcal{S} + \dim \mathcal{C} = \dim A$.

The nonlinear system (3.1.2) has invariant manifolds that correspond to each of the linear subspaces, and the subspaces are locally tangent to these manifolds at the equilibrium. An *invariant manifold* is a space that is invariant under the flow ϕ. That is to say, points starting within an invariant manifold will remain within it for all time.

Examples of invariant manifolds are equilibria, periodic orbits, and the stable, unstable and center manifolds of these solutions. Stable manifolds of an equilibrium solution u can be defined as $\omega = \{\, u_0 \mid \lim_{t\to\infty} \phi(u_0, t) = u \,\}$, and the unstable mani-

fold as $\alpha = \{ u_0 \mid \lim_{t\to\infty} \phi(u_0, -t) = u \}$. Further discussion of invariant manifolds is deferred to Wiggins [14].

An equilibrium is said to be *hyperbolic* if the linearization only contains stable and unstable subspaces, i.e., $\dim \mathcal{C} = 0$. An equilibrium that lacks hyperbolicity is called a *local bifurcation point*. At local bifurcation points, new solutions can emerge, with their properties being determined by the nature of the eigenvalue(s) causing the bifurcation, and by the so-called normal form coefficients. The dynamics near a bifurcation point can be understood by transforming the equations to their normal form on the center manifold. This normal form transformation involves transformation to coordinates that approximately cover the center manifold. It consists of near-identity transformations that eliminate terms in the Taylor expanded vector field (Eq. (3.1.3)) order by order.

The *codimension* of an equilibrium bifurcation is the number of conditions (in addition to Eq. (3.1.2)) that must be met for the bifurcation to occur. These are conditions on either the eigenvalues or the normal form coefficients. The codimension is also the number of parameters that need to be varied (in general) to see the bifurcation. For example, in a model with many parameters, it is very unlikely to see an equilibrium at a Hopf bifurcation (codimension 1) for a fixed parameter set, but adding a single degree of freedom that can be varied can allow us to satisfy both the equilibrium equation and the $\lambda_c = i\omega_c$ condition if f (and A) will permit this.

The next subsection shows how this can be done in a procedural manner for a Hopf bifurcation, which has a center manifold corresponding to a pair of complex conjugate eigenvectors with the eigenvalues $\lambda_c = \pm i\omega_c$. This particular bifurcation is chosen because it plays a role in the generation of temporal oscillations which come up frequently in neural models.

Further discussion of center manifold transformations in general is left to Wiggins [14] and Kuznetsov [11]. Also, Kuznetsov [12] provides succinct expressions for computing normal form coefficients for all equilibrium bifurcations up to codimension 2. It is the value of the coefficients that we are interested in, so we look at methods like Kuznetsov [12] more closely.

3.1.2 Hopf bifurcation

This subsection follows the idea presented in Kuznetsov [12], relying on the fact that we already *know* what the normal form equation should look like, and just want to compute the normal form coefficients.

In general, we write the restriction to the center manifold as

$$u = H(w), \quad H : \mathbb{R}^{n_c} \to \mathbb{R}^n, \tag{3.1.5}$$

and the (known) restricted equation as

$$\dot{w} = G(w), \quad G : \mathbb{R}^{n_c} \to \mathbb{R}^{n_c}, \tag{3.1.6}$$

where G is a polynomial expansion, the coefficients of which are the normal form

coefficients, and n_c is the dimension of the center manifold ($n_c = 2$ for the Hopf bifurcation).

If we substitute Eqs. (3.1.5) and (3.1.6) into Eq. (3.1.1), we obtain the *homological equation*

$$H_w(w)G(w) = f(H(w)), \tag{3.1.7}$$

Expanding H in terms of w,

$$H(w) = \sum_{\nu \geq 1} \frac{1}{\nu!} h_\nu w^\nu, \tag{3.1.8}$$

substituting this into the homological equation, and comparing terms order by order gives systems of linear equations to be solved for the h_ν. These linear systems are in fact singular, so applying Fredholm's alternative is required to ensure solvability of the systems. *Fredholm's alternative* states that for L a singular matrix, $Lu = b$ will have a solution iff $\langle p, b \rangle = 0$, for all p in the null space of the adjoint matrix, $\bar{L}^T p = 0$. Applying this to each order equation will give solvability conditions on any unknown coefficients that are present in $G(w)$. Values for these coefficients can be used to determine the criticality and stability of branching solutions.

For a stable equilibrium becoming unstable through the increase of a parameter β through bifurcation point β_c, the *criticality* of branching solutions refers to which values of β the branching solutions exist in the neighbourhood of the bifurcation. A *subcritical* branch exists for $\beta < \beta_c$, and a *supercritical* branch exists for $\beta > \beta_c$.

At a Hopf bifurcation with critical eigenvalues $\lambda = \pm i\omega_c$, we define the left and right (complex) eigenvectors of the Jacobian

$$Aq = i\omega_c q, \quad A^T p = i\omega_c p \tag{3.1.9}$$

and normalize them according to

$$\langle p, q \rangle \equiv \bar{p}^T q = 1, \tag{3.1.10}$$

noting the standard inner product for complex vector arguments.

The normal form of the Hopf bifurcation (in complex coordinate w) comes from Hopf's 1942 paper [8, 9]

$$G(w) = i\omega_c w + l_1 w |w|^2 + \mathcal{O}\left(|w|^4\right), \; w \in \mathbb{C}^1. \tag{3.1.11}$$

Applying Fredholm's alternative to each order solution of the homological equation will eventually show that the normal form coefficient l_1 is

$$l_1 = \frac{1}{2}\mathrm{Re}\langle p, C(q,q,\bar{q}) + B(\bar{q}(2i\omega_c I_n - A)^{-1}B(q,q)) - 2B(q, A^{INV}B(q,\bar{q})\rangle, \tag{3.1.12}$$

with I_n the $n \times n$ identity, and the notation $A^{INV}b$ representing the solution x to the nonsingular system

$$\begin{bmatrix} A & q \\ \bar{p}^T & 0 \end{bmatrix} \begin{bmatrix} x \\ s \end{bmatrix} = \begin{bmatrix} b \\ 0 \end{bmatrix} \tag{3.1.13}$$

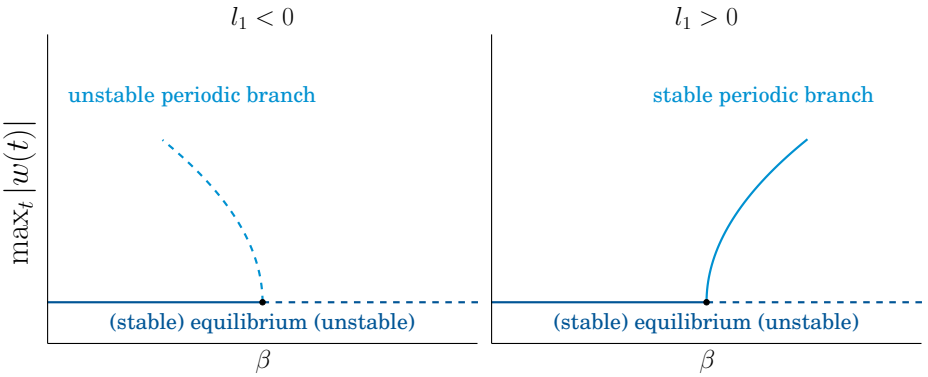

Figure 3.1: Unfolding (branching) diagrams for the Hopf bifurcation. An equilibrium undergoing a Hopf bifurcation will produce a finite amplitude limit cycle (periodic orbit). The sub/super-criticality and stability of the emerging limit cycle is determined by the parameter dependent unfolding in Eq. (3.1.14).

Furthermore, if $l_1 \neq 0$ and Eq. (3.1.1) depends smoothly on a parameter α_1, it can be shown that the cubic truncation of the restriction to the parameter-dependent center manifold is topologically equivalent to the normal form

$$\dot{w} = (\beta + i\omega_c)w + l_1 w\,|w|^2\,. \tag{3.1.14}$$

It is this parameter dependent normal form that allows us to determine the branching diagram of the Hopf bifurcation.

The nature of the Hopf bifurcation depends on the value of l_1. For $l_1 < 0$, the bifurcation is called *subcritical*, and decreasing β through zero takes an equilibrium from unstable to stable, and produces an unstable limit cycle. For $l_1 > 0$, the Hopf bifurcation is called *supercritical*, and increasing β through zero takes an equilibrium from stable to unstable, and produces a branch of stable limit cycles. This is best demonstrated visually, as in Figure 3.1.

The method described within this section can be applied to bifurcations of any codimension, but the analysis quickly gets complicated as n_c increases. As the codimension increases, the number of normal form coefficients also increases. This adds to the number of possibilities for the number of unfolding diagrams. Also with increasing codimension, comes increasing complexity of the formulae for computing the coefficients. The computation coefficients for all generic equilibria bifurcations with a codimension less than 3 is presently well established, and we can look to Kuznetsov [12] for useful expressions to evaluate their numerical values.

3.1.3 Periodic solutions

Periodic solutions to Eq. (3.1.1) can be expressed in terms of the flow

$$u - \phi(u, T, \alpha) = 0, \tag{3.1.15}$$

where $T > 0$ is the minimal time to satisfy this equation, and we have made the parameter dependence explicit, i.e., $X = [u^T, \alpha]^T \in \mathbb{R}^{n+m}$ has been expanded in the flow's arguments. As there are very few systems for which solutions to this equation can be determined analytically, numerical methods are key for finding solutions. The method we make use of treats this as a problem in $n+1$ unknowns, by including T in the state vector, and is described in more detail in Section 3.4.4. To summarize here, one can integrate the system of ODEs for a time T, and perform a Newton update on the $n+1$ dimensional system based on the residual of the left hand side of Eq. (3.1.15).

However, there is a problem with doing this, in that there are only n equations in the $n+1$ unknowns. This leads to an infinite number of solutions, which correspond to the starting point that can be anywhere along the periodic orbit. To handle this, an extra condition must be introduced to effectively fix the phase of the solution. In general, this can be written as

$$P(u, t) = 0, \tag{3.1.16}$$

where P can fix a Poincaré plane of intersection, or represent some integral constraint over the time-course of the periodic solution [11]. If we are dealing with a large system of equations, then in practice it is more convenient to simply remove the direction of the flow from the Newton update step. We will elaborate on this approach in the computational section.

What can be done once a periodic solution has been found? Difference equations (i.e., the map $u^{k+1} = \phi(u^k, t, \alpha)$) can be linearized and split up into different eigenspaces similar to what was done with ODEs at equilibrium in Eq. (3.1.3). The main modification that needs to be made for maps is with the linear stability, looking at $\partial_u \phi(u, T, \alpha)$. Upon evaluation at an exact periodic solution u, $\partial_u \phi(u, T, \alpha)$ is called the *monodromy matrix*. Linear stability analysis of a periodic solution u corresponds to the eigenvalue problem

$$[\partial_u \phi(u, T, \alpha)]\, v = \mu v. \tag{3.1.17}$$

The monodromy matrix will always have one eigenvalue $\mu = 1$, and this corresponds to perturbations along the periodic solution. Stable, center, and unstable eigenspaces are now determined by eigenvalues μ with $|\mu| < 1, |\mu| = 1$, and $|\mu| > 1$ respectively. μ are called the *Floquet multipliers*, as Eq. (3.1.17) represents a linear system with time-periodic coefficients, analyzed originally by Floquet [3].

Generic bifurcations of the periodic cycle come in three flavours: $\mu = 1$, $\mu = -1$, and $\mu_{1,2} = e^{\pm i\theta_0}$. The listed bifurcations are called *fold*, *flip* and *torus*, respectively. The fold bifurcation involves the spontaneous generation of a stable and unstable periodic solution. The flip is also known as *period doubling*, and involves the destabilization of an existing periodic orbit, and the generation of a new periodic solution with a different period. The torus bifurcation involves the destabilization of an existing periodic orbit, and the generation of either i) a new periodic orbit or ii) a dense torus of trajectories.

3.2 Infinite dimensional systems

While the previous section was dealing with a finite number of state variables, this section extends some of those ideas to infinite dimensional systems. Infinite dimensional systems arise predominantly in two ways: i) by the addition of time delays, or ii) by extending the state variables to depend on continuous variables other than time. We will use both views of the infinite dimensionality in this thesis. The scalar neural field uses both i and ii. The integral formulation of Liley's model uses i and ii, but its formulation as the PDE system requires only ii.

The most general way we write an evolution equation for a smooth, autonomous, spatially extended, parameter dependent system is

$$u_t = f(u, u^t, \alpha). \tag{3.2.1}$$

This differs from the finite dimensional case without delays, as we now consider $u(\mathbf{x}, t)$ to have n components defined for $\mathbf{x} \in \mathbb{R}^d$ and $t \in [0, \infty)$, $u^t = \{u(\mathbf{x}, \tau) : \tau < t\}$ is the trajectory of the past solution, α the set of m parameters, and a functional operator $f : \mathbb{R}^n \times \mathcal{C}^1(\mathbb{R}^n) \times \mathbb{R}^m \to \mathbb{R}^n$. The functional operator can incorporate partial derivatives of the spatial coordinates, and integrals over the spatial or (past) time domains.

3.2.1 Equilibrium solutions

The idea of an equilibrium solution remains the same as in the finite dimensional case, it is a solution that does not change in time.

Generally, equilibrium solutions can depend on space. In terms of our general definition for infinite dimensional systems, we have

$$f(u, u, \alpha) = 0 \tag{3.2.2}$$

for $u(\mathbf{x})$. It is important to note that the time history is evaluated at the equilibrium solution as well. A *spatially homogeneous equilibrium*, or *SHE*, is an equilibrium that in addition to satisfying Eq. (3.2.2), does not vary with space as well, satisfying

$$\nabla_x u = 0.$$

These types of equilibria are very important in the study of infinite dimensional systems, as they often represent resting or ground state solutions that the system will tend to in some parameter regimes. These solutions are easier to find numerically than space dependent equilibria. Through continuation methods parameters can be varied until a bifurcation of the SHE occurs, and a new type of solution branch, can then be picked up and continued as well. This process allows us to study the dynamics of the system, gradually building up the complexity of the solutions.

For spatially extended systems, the equation for SHE reduces to a finite dimensional one similar to Eq. (3.1.2). Stability with respect to spatially homogeneous modes can be obtained by studying the linearization of Eq. (3.2.1) about the SHE,

subject to spatially homogeneous perturbations. For non-delayed systems, this will also be a finite dimensional (i.e., polynomial) problem, but in general when space-dependent delays are present, transcendental equations (i.e., involving irreducible fractional exponents), may arise.

SHE are also important for the study of spatially localized solutions and travelling waves. These solutions can be studied from the view of *homoclinic* and *heteroclinic* connections, respectively. A *homoclinic* orbit is a solution that connects the unstable manifold of an equilibrium to the stable manifold of the same equilibrium. A *heteroclinic* orbit is a solution that connects the unstable manifold of an equilibrium to the stable manifold of a different equilibrium. Localized solutions connect a SHE to itself in a one dimensional spatial domain (homoclinic in space), and wave fronts connect one SHE to another (heteroclinic in space), also in a one dimensional spatial domain. We do not look at these types of solutions in this thesis, as they have been studied quite extensively in neural field models [1].

3.2.2 Linear stability

To linearize a spatially extended system about a general solution $u_0(\mathbf{x}, t)$, we substitute

$$u(\mathbf{x}, t) = u_0(\mathbf{x}, t) + \epsilon u_1(\mathbf{x}, t)$$

into Eq. (3.2.1) and look at the terms proportional to ϵ. This gives

$$\frac{\partial u_1}{\partial t} = f_u(u_0, u_0^t, \alpha)u_1.$$

The linear stability of infinite dimensional systems can be investigated by looking at perturbations of the form

$$u_1(\mathbf{x}, t) = \varphi(\mathbf{x})e^{\lambda t},$$

with $\lambda \in \mathbb{C}$. The general case of stability is beyond the scope of this thesis, but rather we will look at the linear stability of SHE with respect to spatial Fourier modes with specific wave vectors $\mathbf{k} \in \mathbb{R}^2$. This is written as

$$u_1(\mathbf{x}, t) = q(\mathbf{k})e^{i\mathbf{k}\cdot\mathbf{x}}e^{\lambda t} \tag{3.2.3}$$

Substituting this into Eq. (3.2.1) will result in a system of equations that relates λ and $\mathbf{k}$, the *dispersion relation*. Looking at perturbations with $\mathbf{k} = \mathbf{0}$ gives linearized dynamics of the spatially homogeneous modes.

Dispersion relations

After the substitution of Eq. (3.2.3), a dispersion relations can be obtained, written to satisfy some equation of the form

$$F(\lambda, \mathbf{k}, \alpha) = 0.$$

For PDEs, and systems without delays, the dispersion relation can be reduced to a scalar equation which is polynomial in λ. Systems that include delays can be much more unpredictable in the form of F, but F can generally be reduced to a scalar equation with nonlinear dependence on λ. For example, the double exponential connectivities used in the scalar neural field result in a dispersion relation with terms that have a rational exponents.

For systems that are spatially homogeneous and isotropic, the dispersion relation will depend only on the magnitude $k = \|\mathbf{k}\|$ and not the direction of the wavevector,

$$F(\lambda, k, \alpha) = 0. \tag{3.2.4}$$

The following analysis presented proceeds with this case. We think of the set of solutions to this equation as

$$\Lambda = \{\, \lambda \mid F(\lambda, k, \alpha) = 0 \,\}. \tag{3.2.5}$$

There will be a certain (generally unknown) number of continuous branches that satisfy Eq. (3.2.4), and can thus be locally parameterized by k.

$$\Lambda^{CONT} = \left\{ \lambda \;\middle|\; F(\lambda(k), k, \alpha) = 0,\ \lambda(k) = \lim_{\epsilon \to 0} \lambda(k \pm \epsilon) \right\}. \tag{3.2.6}$$

In addition to this, there also exists the possibility of discrete solutions to the dispersion relation where λ can not be parameterized with k, and we denote this

$$\Lambda^{DISC} = \Lambda \setminus \Lambda^{CONT}. \tag{3.2.7}$$

3.2.3 Bifurcation from dispersion relation

Two specific bifurcations that arise from the destabilization of a continuous dispersion relation Λ^{CONT} are the *Turing* and the *dynamic Turing* bifurcations. The first occurs when a real valued branch of the continuous dispersion relation crosses the $\operatorname{Re}\lambda = 0$ threshold, and the second for a complex valued branch crossing this threshold, both while changing some parameter, say γ. Similar to the fold and the Hopf bifurcations of the finite dimensional system, the Turing bifurcation has the potential to produce steady state solutions, and the dynamic Turing to produce temporally oscillating solutions. But now, the spatial scale of these bifurcating solutions is dependent on the wave vector causing the destabilization, k_c. This is shown for the dynamic Turing bifurcation in Figure 3.2.

If space is one dimensional, $\mathbb{R}$, then there are at most 2 k_1 values that satisfy $k = \|\mathbf{k}\| = |k_1|$. In spatial dimensions greater than one, we have $k = \|\mathbf{k}\| = \sqrt{k_1^2 + k_2^2}$ (for example with Euclidean norm in $\mathbb{R}^2$) which has a degree of freedom giving rise to an infinite correspondence between k and its components k_j.

We do not have the tools to address bifurcations that have infinite dimension, however we can apply ideas from symmetry to help with this problem.

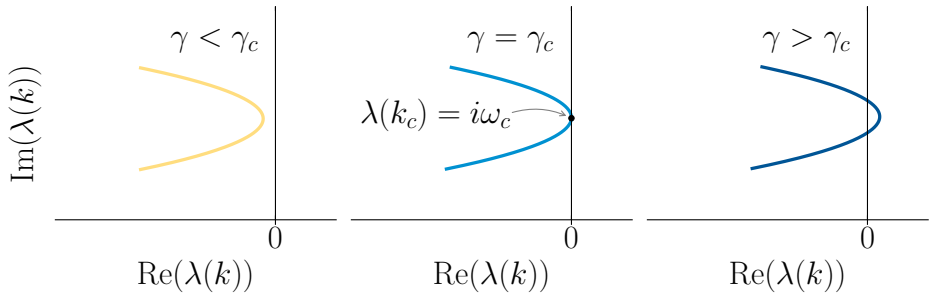

Figure 3.2: What happens in a dynamic Turing bifurcation. As a parameter is increased through γ_c, a portion of a complex conjugate branch becomes unstable, with wave number k_c and angular frequency ω_c leading the way.

3.3 Bifurcations with symmetry

One way that we can circumvent the infinite dimensionality of bifurcations that arise from the dispersion relations in two dimensional space is to look for solutions that are symmetric with respect to subgroups of the Euclidean symmetry. Euclidean symmetries are an important group of symmetries that are present in models that are homogeneous and isotropic, such as specific instances of the scalar neural field and Liley's model described in Chapter 2. This section will lay out the formulation of bifurcation problems in the presence of symmetry, and then look at a specific symmetric bifurcation, the $D_4 \ltimes T^2$ symmetric Hopf bifurcation.

3.3.1 General problem

For finite dimensional dynamical systems, it is intuitive that low codimension bifurcations arise more commonly than higher codimension. For example, if we think of a bifurcation in which n complex conjugate eigenvalues cross the imaginary axis together, this would involve the vector field of Eq. (3.1.2) to satisfy n additional constraints simultaneously, an unlikely scenario in the general case.

However, when symmetries are present, in either finite or infinite dimensional systems, we often find the multiplicity of certain eigenvalues to increase. Fortunately, while symmetries do generally increase the number of bifurcating modes, these modes are confined to moving together, and so do not increase the codimension of a given bifurcation. For instance, if one mode satisfies the bifurcation condition, then all of the related symmetric modes must satisfy the condition as well. The symmetries also play a role in restricting the terms that are possible in the normal form on the centre manifold. The result is that symmetric bifurcations will have more complicated normal forms than non-symmetric ones, but the situation is more manageable than when dealing with higher codimension bifurcations.

The useful formulation of symmetric bifurcations presented here is thanks to Golubitsky & Stewart [5]. For this view, we consider an evolution equation written as

$$\partial_t v = f(v) \tag{3.3.1}$$

for $v \in V$ and $f : V \to V$. This can be seen to be the finite dimensional dynamical system Eq. (3.1.1), or the infinite dimensional one, Eq. (3.2.1), depending on the interpretation of V.

We consider the case when f commutes with the action of some Lie group Γ, i.e.,

$$f(\gamma v) = \gamma f(v), \ \gamma \in \Gamma,$$

For bifurcations with symmetry Γ, a bifurcating branch will have less symmetry than Γ. This is referred to as *spontaneous symmetry breaking*. If Γ acts on V, then

$$\Sigma_v = \{ \sigma \in \Gamma \mid \sigma v = v \}$$

is called the *isotropy subgroup*. The *fixed-point subspace* of a subgroup $\Sigma \subset \Gamma$ is

$$V^\Sigma = \{ v \in V \mid \sigma v = v, \ \forall \sigma \in \Sigma \},$$

and it consists of all points in V whose symmetries include Σ.

The most important thing to gather from these definitions is that if $f : V \to V$ commutes with Γ, then $f : V^\Sigma \to V^\Sigma$. That is, solutions that have the symmetry of an isotropy subgroup of Γ remain in their isotropy subgroup under the application of f. This is the key aspect that allows one to formulate normal form equations for symmetric systems undergoing bifurcation.

We do not work with symmetric bifurcation theory directly in this thesis. Instead, we rely on normal forms that have already been formulated and studied in the presence of symmetry, and look at how we can compute the normal form coefficients from our neural field models.

3.3.2 $D_4 \ltimes T^2$ Hopf bifurcation

The symmetric bifurcation that this thesis revolves around is the Hopf bifurcation on a periodic square, and it arises as follows.

Solutions to spatially extended equations that are homogeneous and isotropic on $\mathbb{R}^2$ are equivariant under the group of continuous translations T^2 and continuous rotations and reflections $O(2)$. Combined, these make the Euclidean symmetry group $E(2) = O(2) \ltimes T^2$. The dispersion relations with this symmetry group are continuous functions of the wavenumber k, and destabilization involves the loss of stability of an infinite number of wave modes. As this is impractical from the viewpoint of bifurcation analysis, the Euclidean symmetry can be restricted to sub-symmetries. There are many ways to do this, one of which is to restrict to tiling patterns of the plane, the symmetries $D_n \ltimes T^2$, with D_n being the dihedral group with n rotations and n reflections. $D_2 \ltimes T^2$ refers to lattices with a rhomboid symmetry (there are a few of them, such as the rectangles with different side lengths), $D_4 \ltimes T^2$ a lattice with square symmetry, and $D_6 \ltimes T^2$ a lattice with hexagonal symmetry. The main reason we would decompose into these specific symmetries, is to preserve the translational part of the Euclidean symmetry which will allow for travelling wave modes.

When a complex branch of the continuous dispersion relation destabilizes as in

Figure 3.2, and we restrict our view to the $D_4 \ltimes T^2$ symmetric modes, we effectively restrict our view to the spatial domain $[0, L_c]^2$ with $L_c = 2\pi/k_c$, and the temporal domain $[0, T_c]$ with $T_c = 2\pi/\omega_c$. The multiplicity of the complex conjugate pair causing the destabilization will be 4, corresponding to the complex valued eigenmodes

$$\begin{aligned} \phi_1 &= e^{i(\omega_c t + k_c x_1)}, \\ \phi_2 &= e^{i(\omega_c t - k_c x_1)}, \\ \phi_3 &= e^{i(\omega_c t + k_c x_2)}, \\ \phi_4 &= e^{i(\omega_c t - k_c x_2)}, \end{aligned} \tag{3.3.2}$$

so this means that the codimension of the bifurcation will still be 1, but the dimension of the center eigenspace will be 8.

Normal form & unfolding

The normal form for the $D_4 \ltimes T^2$ Hopf bifurcation was originally studied by Silber & Knobloch [13]. Their analysis determined that the cubic truncation of the normal form can be written in terms of four complex-valued amplitudes $A_j \in \mathbb{C}$,

$$\begin{aligned} \dot{A}_1 &= (\beta + i\omega_c) A_1 + A_1 \left[a_1 |A_2|^2 + a_2 \left(|A_1|^2 + |A_2|^2\right) + a_3 \left(|A_3|^2 + |A_4|^2\right)\right] \\ &\quad + a_4 \bar{A}_2 A_3 A_4 \\ \dot{A}_2 &= (\beta + i\omega_c) A_2 + A_2 \left[a_1 |A_1|^2 + a_2 \left(|A_1|^2 + |A_2|^2\right) + a_3 \left(|A_3|^2 + |A_4|^2\right)\right] \\ &\quad + a_4 \bar{A}_1 A_3 A_4 \\ \dot{A}_3 &= (\beta + i\omega_c) A_3 + A_3 \left[a_1 |A_4|^2 + a_2 \left(|A_3|^2 + |A_4|^2\right) + a_3 \left(|A_1|^2 + |A_2|^2\right)\right] \\ &\quad + a_4 \bar{A}_4 A_1 A_2 \\ \dot{A}_4 &= (\beta + i\omega_c) A_4 + A_4 \left[a_1 |A_3|^2 + a_2 \left(|A_3|^2 + |A_4|^2\right) + a_3 \left(|A_1|^2 + |A_2|^2\right)\right] \\ &\quad + a_4 \bar{A}_3 A_1 A_2, \end{aligned} \tag{3.3.3}$$

with complex valued normal form coefficients $a_k \in \mathbb{C}$. Through application of the Equivariant Hopf Theorem [4], it was determined that there are five periodic solutions that are guaranteed to emerge from this bifurcation. The five solutions are called: standing roll (SR), travelling roll (TR), travelling square (TS), standing square (SS), and alternating roll (AR). These five solutions are shown in Figures 3.3-3.5, and the ways in which they are related to the amplitudes A_j are given in Table 3.1. Also in the table are the amplitudes of each solution in terms of the normal form coefficients and the unfolding parameter. Increasing the unfolding parameter through zero causes the SHE to go from stable to unstable, so the criticality of solutions is given by the sign of the denominator. For example, $\mathrm{Re}(a_1 + 2a_2 + 2a_3 - a_4) > 0$ implies a real valued amplitude for AR when $\beta < 0$, thus the AR branch would bifurcate subcritically. With known normal form coefficients, this can be applied to each of the five branches, giving the complete picture of criticality.

Considering all of the criticality conditions in Table 3.1 and all of the stability results in [13] together, Silber & Knobloch determine that there are 34 qualitatively

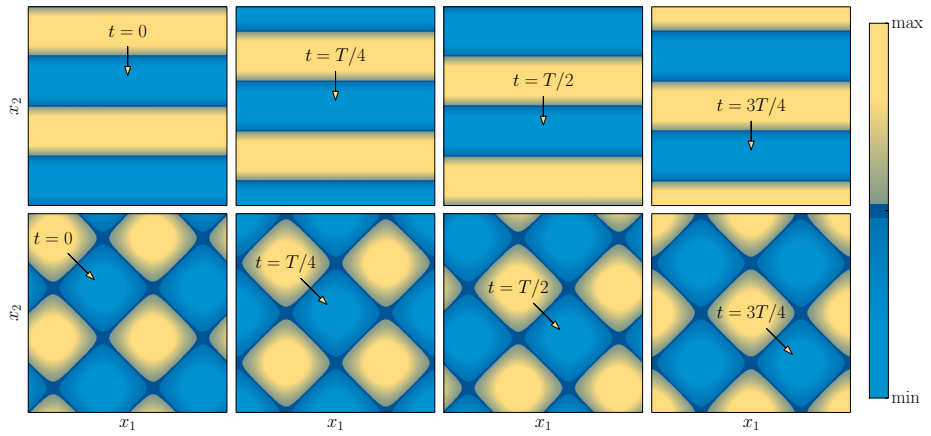

Figure 3.3: Time dependent snapshots of travelling modes that bifurcate from the $D_4 \ltimes T^2$ symmetric Hopf bifurcation. Spatial domain is $[0, 2L_c]^2$. *Top*: Travelling roll (TR). *Bottom*: Travelling square (TS).

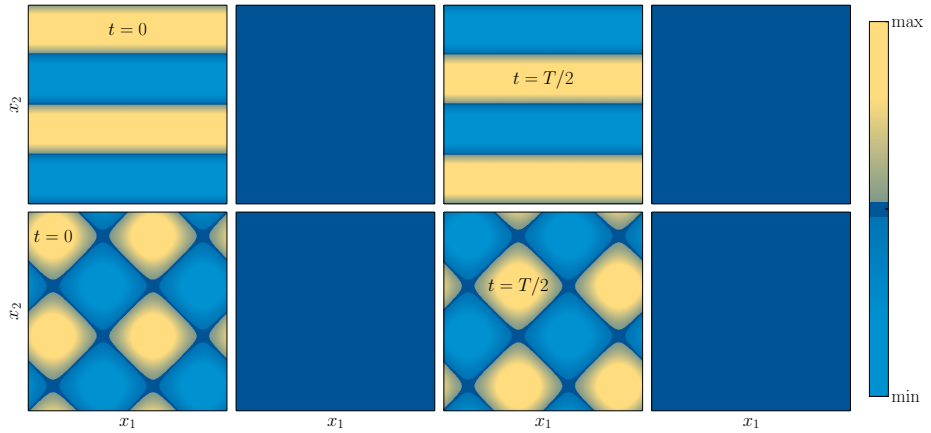

Figure 3.4: Time dependent snapshots of standing modes that bifurcate from the $D_4 \ltimes T^2$ symmetric Hopf bifurcation. Spatial domain is $[0, 2L_c]^2$. *Top*: Standing roll (SR). *Bottom*: Standing square (SS).

Solution	**Amplitudes**	**Criticality condition**
TR	$A_1 \neq 0,\ A_2 = A_3 = A_4 = 0$	$\lvert A_1\rvert^2 = -\beta/\operatorname{Re}(a_2)$
SR	$A_1 = A_2 \neq 0,\ A_3 = A_4 = 0$	$\lvert A_1\rvert^2 = -\beta/\operatorname{Re}(a_1 + 2a_2)$
TS	$A_1 = A_3 \neq 0,\ A_2 = A_4 = 0$	$\lvert A_1\rvert^2 = -\beta/\operatorname{Re}(a_2 + a_3)$
SS	$A_1 = A_2 = A_3 = A_4 \neq 0$	$\lvert A_1\rvert^2 = -\beta/\operatorname{Re}(a_1 + 2a_2 + 2a_3 + a_4)$
AR	$A_1 = A_2 = -iA_3 = -iA_4$	$\lvert A_1\rvert^2 = -\beta/\operatorname{Re}(a_1 + 2a_2 + 2a_3 - a_4)$

Table 3.1: The five guaranteed solutions emerging from the $D_4 \ltimes T^2$ symmetric Hopf bifurcation. Given are the nontrivial amplitudes that contribute to the solution, and the amplitude condition that gives criticality.

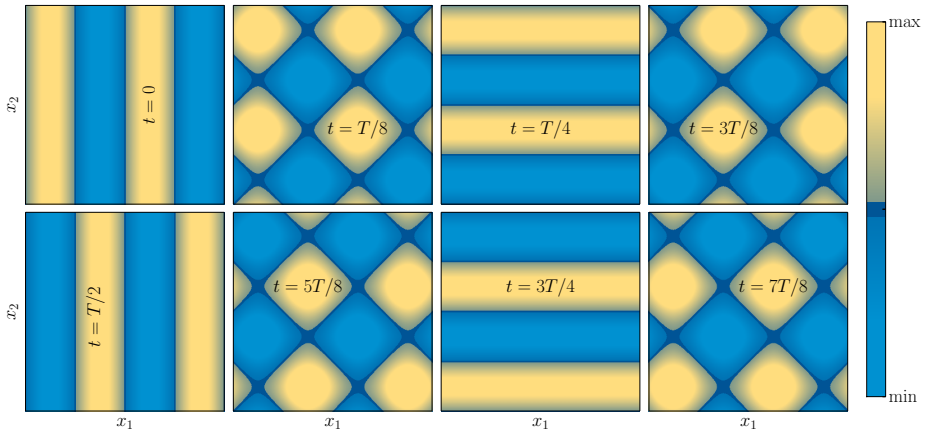

Figure 3.5: Time dependent snapshots of the alternating roll (AR) solution that bifurcates from the $D_4 \ltimes T^2$ symmetric Hopf bifurcation. Spatial domain is $[0, 2L_c]^2$.

different regions for the unfolding diagrams for $\operatorname{Re} a_4 > 0$. For $\operatorname{Re} a_4 < 0$, additional unfoldings can be obtained simply by swapping the branches of SS and AR. All of these unfolding possibilities are shown in Figure 3.6, which is reproduced from [13].

Later in the thesis, we will see the stable travelling rolls and alternating rolls from direct numerical simulation of the scalar neural field, and we will explicitly compute a branch of standing square waves in Liley's model.

3.4 Continuation

Continuation methods form the bulk of the numerical computation for almost all things discussed above. This is because:

1. The main idea underlying continuation is simple,
2. The simple idea is extensible, and
3. Quadratic convergence of Newton's method makes for fast algorithms.

Continuation aims to find one parameter families of solutions to underdetermined equations of the form

$$g(U, \beta) = 0, \tag{3.4.1}$$

where what g, U, and β represent change depending on context, but $\beta \in \mathbb{R}$ is always consistent. For example, $g(U, \beta)$ can be the equilibria described by Eq. (3.1.2), or the periodic solutions described by Eq. (3.1.15). The main continuation problems needed for this thesis are described in the upcoming *Applied to* Sections 3.4.2–3.4.6.

If a solution is known for a particular value of β, continuation can be applied to find how that solution changes with β. Sometimes, a continuous family of solutions may not be monotonic with respect to β, which will cause certain continuation methods to fail. When this happens, it often suffices to change to a *better* continuation method. These ideas seem to have originated with Keller [10].

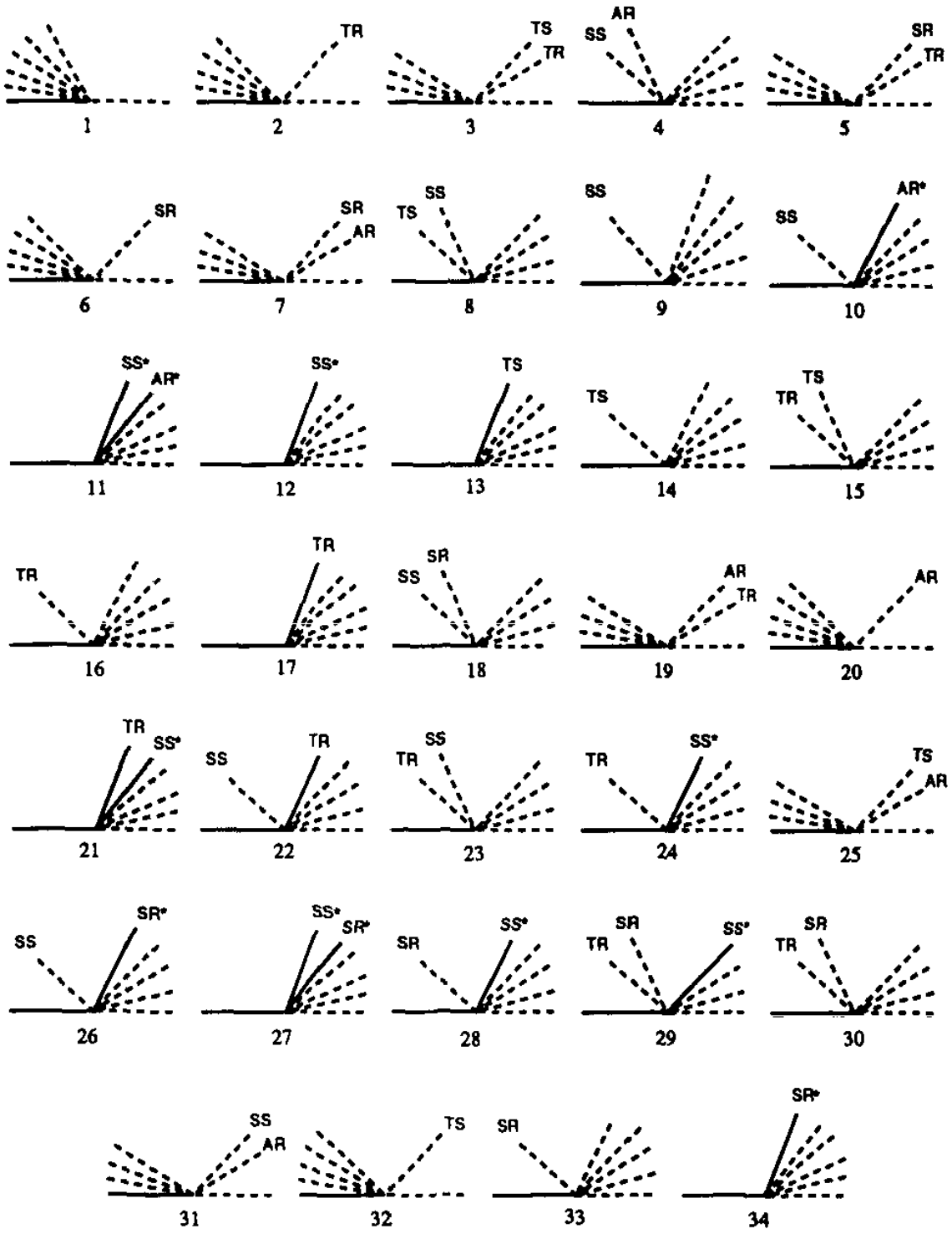

Figure 3.6: Unfolding diagrams of the $D_4 \ltimes T^2$ symmetric Hopf bifurcation for 34 qualitatively different normal form coefficient regions. These are only for $\mathrm{Re}\, a_4 > 0$, and more diagrams can be obtained for $\mathrm{Re}\, a_4 < 0$ simply by switching the AR and SS branches. *Reproduced with permission from Silber & Knobloch, 1991 [13].*

3.4.1 General methods

There are two forms of continuation methods we make use of:

1. Parameter continuation, and
2. Pseudoarclength continuation,

for finding continuous, one parameter families of solutions.

Parameter continuation

The simplest method of continuation is called *parameter continuation*. Parameter continuation involves changing the parameter β by an amount $\Delta\beta$, and using the known solution at β as the initial guess to a Newton iteration at the new parameter value $\beta + \Delta\beta$. Visually, this is in Figure 3.7, and algorithmically this is expressed as

1. Assign known solution of $g(U, \beta) = 0$ to $U_0 = U$.
2. Solve the linear system
$$\partial_U g(U_k, \beta + \Delta\beta)\Delta U = -g(U_k, \beta + \Delta\beta).$$
3. Update solution
$$U_{k+1} = U_k + \Delta U.$$
4. Increase k, repeat from 2 until some error tolerance reached.

The repetition of points 2-4 is just a simple Newton iteration.

The main drawback to parameter continuation is that it assumes U is a function of β, i.e., $U(\beta)$. This is not generally true, as U can have multiple solutions for a given parameter value. In the neighbourhood of a fold bifurcation, for example, u and β are related as in the right panel of Figure 3.7, which causes the algorithm to break in an unpredictable way. By unpredictable, we simply mean that a sequence $\{U_k\}$ will follow the global dynamics of the map given in point 3. The next algorithm fixes this situation.

Pseudoarclength continuation

Pseudoarclength continuation takes its initial guess to be tangential to the slope of g at the current solution. It then performs a Newton iteration in directions orthogonal to the direction of that initial guess. This change in initial guess can be worked into parameter continuation as well, so the big difference in pseudoarclength continuation is in the orthogonal update. This is what allows the method to get around the folds that parameter continuation has problems with, seen in Figure 3.8. It is natural to split the vectors tangent to g into their state components and their parameter component, i.e., $t = (t^{(U)T}, t^{(\beta)})^T$. The algorithm for pseudoarclength continuation is

1. Start with known solutions (U_0, β_0) and (U_1, β_1), with tangent vector t_0 between them, and a step size Δs.

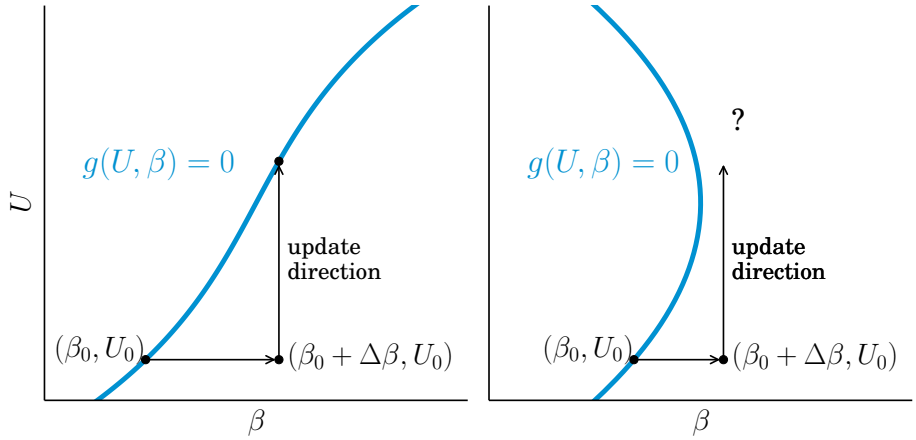

Figure 3.7: What is happening in parameter continuation. *Left*: The method can work when there is a solution to be found at the new parameter value $\beta+\Delta\beta$. *Right*: Near fold points of g, parameter continuation is doomed to fail because there is no solution to find.

2. Compute tangent vector t_1 from the equation

$$\begin{bmatrix} \partial_U g(U_1,\beta_1) & \partial_\beta g(U_1,\beta_1) \\ t_0^{(U)T} & t_0^{(\beta)} \end{bmatrix} \begin{bmatrix} t_1^{(U)} \\ t_1^{(\beta)} \end{bmatrix} = \begin{bmatrix} 0 \\ 1 \end{bmatrix}.$$

3. Form predictor as

$$\hat{U} = U_k + \frac{\Delta s}{\|t_0\|} t_0^{(U)}, \quad \hat{\beta} = \beta_k + \frac{\Delta s}{\|t_0\|} t_0^{(\beta)},$$

4. Assign $U_2 = \hat{U}, \beta_2 = \hat{\beta}$, i.e., $k = 2$
5. Solve the system

$$\begin{bmatrix} \partial_U g(U_k,\beta_k) & \partial_\beta g(U_k,\beta_k) \\ t_1^{(U)T} & t_1^{(\beta)} \end{bmatrix} \begin{bmatrix} \Delta U \\ \Delta\beta \end{bmatrix} = \begin{bmatrix} -g(U_k,\beta_k) \\ 0 \end{bmatrix}.$$

6. Update the solution

$$U_{k+1} = U_k + \Delta U, \quad \beta_{k+1} = \beta_k + \Delta\beta$$

7. Increase k, repeat from 5 until some error tolerance reached.

The repetition of points 5-7 is again just a Newton iteration, but with the initial set up, it now updates not only the state but the continuation parameter as well.

The particular method described in the algorithm is known as *Keller's method* [10]. There are a few variants of pseudoarclength continuation that will have very slightly different convergence properties, described in Govaerts [6], but this method was sufficient for any computations required in this thesis. Stressing again that this method is sufficient to allow for continuation around folds, we direct your attention to the right

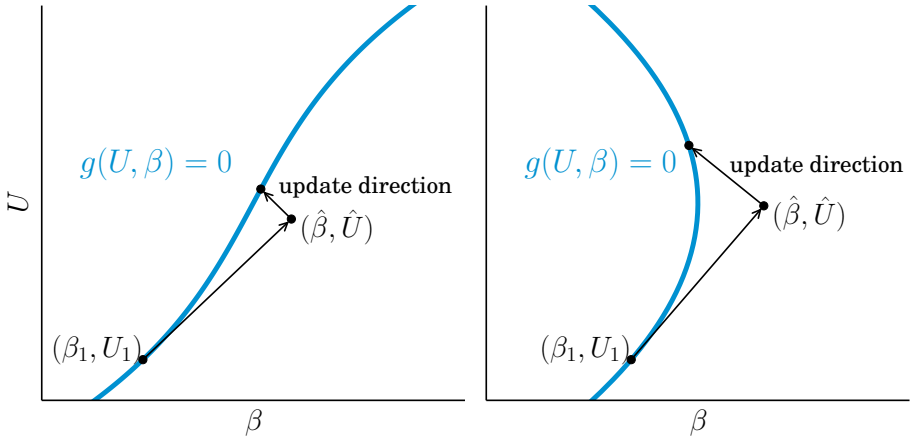

Figure 3.8: What is happening in pseudoarclength continuation. *Left*: For situations where parameter continuation will work, pseudoarclength works as well. The initial guess $(\hat{\beta},\hat{U})$ is typically closer to the actual solution which is beneficial for starting the Newton iteration both here and in parameter continuation. *Right*: When parameter continuation breaks down at a fold, pseudoarclength can succeed, provided the predicted step is not too large.

panel of Figure 3.8.

3.4.2 Applied to equilibria

For a finite dimensional dynamical system, the continuation of an equilibrium is as straightforward as it gets. It can be achieved simply by setting the general function g equal to the vector field of the system, f, the state $U = u$, and the continuation parameter $\beta = \alpha_1$, a single parameter out of the ODE's parameter set. That is, the elements needed for continuation are

$$\begin{aligned} g(U,\beta) &= f(u,\alpha), \\ \partial_U g(U,\beta) &= A(u,\alpha), \\ \partial_\beta g(U,\beta) &= \partial_{\alpha_1} f(u,\alpha). \end{aligned} \tag{3.4.2}$$

Various software packages are available to perform this computation for parameter dependent vector fields. For instance, Matcont [7] written in Matlab, or Auto-07p [2]. These packages however, are written with ODEs in mind, and work very well for systems with few degrees of freedom. When it comes to large discretized PDE problems, however, the algorithms used scale poorly in dimension, and thus can not be applied in a timely manner.

3.4.3 Applied to bifurcations of equilibria

For continuation of a bifurcation of an equilibrium, we think of the problem like this: Continuation is applied to the equilibrium such that the condition causing the bifurcation holds. As one parameter is needed for the continuation of the equilibrium, (at least) another degree of freedom must be considered so that the bifurcation condition can be met. For continuation of codimension n bifurcations, we effectively think of this as a $n+1$ dimensional continuation – 1 parameter for the equilibrium, and n parameters to ensure it satisfies the bifurcation conditions. In the context of the presented continuation algorithms, we can move n parameters into our state U so that β remains one dimensional. How to set up the nonsingular systems that will allow for the continuation of the codimension 1 fold bifurcation of equilibria is now presented.

Continuation of fold

At a non-degenerate fold bifurcation, also called a *quadratic turning point*, the Jacobian, A, at our equilibrium has a nullspace of dimension 1. We can thus define left and right nullvectors $p \neq 0$ and $q \neq 0$ according to

$$Aq = 0, \quad A^T p = 0.$$

A *minimally augmented system* can be defined for g,

$$g(u,\alpha) = \begin{bmatrix} f(u,\alpha) \\ h(u,\alpha) \end{bmatrix} = \begin{bmatrix} 0 \\ 0 \end{bmatrix}$$

where $h(u,\alpha) \in \mathbb{R}$ is part of the solution to

$$\begin{bmatrix} A & q \\ p^T & 0 \end{bmatrix} \begin{bmatrix} q \\ h \end{bmatrix} = \begin{bmatrix} 0 \\ 1 \end{bmatrix}.$$

What is more important to know about h, is that its derivatives with respect to an arbitrary state vector or parameter z are of the form

$$h_z = -p^T \left(\partial_z A\right) q.$$

It can then be shown that the matrix

$$\begin{bmatrix} A & \partial_{\alpha_1} f \\ -p^T \left(\partial_u A\right) q & -p^T \left(\partial_{\alpha_1} A\right) q \end{bmatrix}$$

is nonsingular, with proof of this given in Govaerts [6], Chapter 4.1.2.

Finally, we write the elements needed for continuation of a fold bifurcation by adding one parameter into the state $U = (u^T, \alpha_1)^T$ and having a free parameter for

the continuation $\beta = \alpha_2$,

$$\begin{aligned} g(U,\beta) &= \begin{bmatrix} f(u,\alpha) \\ h \end{bmatrix} \\ \partial_U g(U,\beta) &= \begin{bmatrix} A(u,\alpha) & \partial_{\alpha_1} f(u,\alpha) \\ -p^T\big(\partial_u A(u,\alpha)\big)q & -p^T\big(\partial_{\alpha_1} A(u,\alpha)\big)q \end{bmatrix} \\ \partial_\beta g(U,\beta) &= \begin{bmatrix} \partial_{\alpha_2} f(u,\alpha) \\ -p^T\big(\partial_{\alpha_2} A(u,\alpha)\big)q \end{bmatrix}. \end{aligned} \tag{3.4.3}$$

Further, the pseudoarclength algorithm can be tailored to this specific case, including scale parameters for the state and both parameters, θ_x, θ_{α_1} and θ_{α_2}, trying to stabilize the numerics further. However, this level of optimization/stability was not needed for computations done in this thesis.

3.4.4 Applied to periodic orbits

For continuation of a finite dimensional periodic solution, the temporal period of the solution must be considered in the state variables. Using the components that were defined in Section 3.1.3, we identify the state vector $U = (u^T, T)^T$, and a continuation parameter $\beta = \alpha_1$. The components for continuation are then written

$$\begin{aligned} g(U,\beta) &= \begin{bmatrix} u - \phi(u,T,\alpha) \\ P(u,T) \end{bmatrix} \\ \partial_U g(U,\beta) &= \begin{bmatrix} I - \partial_u \phi(u,T,\alpha) & -\partial_t \phi(u,T,\alpha) \\ \partial_u P & \partial_T P \end{bmatrix} \\ \partial_\beta g(U,\beta) &= \begin{bmatrix} -\partial_{\alpha_1} \phi(u,T,\alpha) \\ 0 \end{bmatrix}. \end{aligned} \tag{3.4.4}$$

Using these components to continue a periodic solution, however, can be tricky, and is a generally fragile process. As written, the equations suggest that $P(u,T)$ is independent of the parameters. This is not generally true, and continuation can possibly take us towards solutions that will never satisfy $P = 0$, causing a breakdown of the algorithm. This can be alleviated by monitoring the transversality of the orbit on $P = 0$, and reorthogonalizing P with the new periodic solutions as continuation steps are made.

Matcont and Auto-07p favour integral constraints over the time course of the period rather than this Poincaré plane. The reason being that it avoids the problem discussed in the above paragraph. This does however become computationally prohibitive when dealing with large systems, so we prefer the more easily implemented Poincaré plane while considering the noted potential problems.

3.4.5 Applied to continuous dispersion relations

Continuation methods are also useful for computing the continuous portion of dispersion relations, Λ^{CONT}. For PDEs, dispersion relations take the form of polynomials in both λ and k, so for a given k value, all possible solutions for λ can be computed in an algorithmic way. This is not the case when looking at the integral operators for the neural fields in general. Sometimes the dispersion relations have terms with rational exponents that can not be removed, and in even worse cases, the Fourier transform can not be evaluated symbolically at all. Even in these cases, however, it is still likely that the $k = 0$ state gives an easier system in λ. Keeping only the roots that satisfy the dispersion relation, we can perform parameter continuation in k to get different branches of the dispersion relation Λ^{CONT}.

There are a few things that must be noted when taking this approach. The first is that while we are looking for dispersion relationships that are continuous, they are not necessarily smooth. For instance, two separate branches of Λ^{CONT} can collide at a given value of $k = k_r$, called a resonant point. The direction of a branch at a resonant point changes discontinuously, i.e.,

$$\lim_{\epsilon\to 0}\big(\lambda_j(k_r+\epsilon)-\lambda_j(k_r)\big) \neq \lim_{\epsilon\to 0}\big(\lambda_j(k_r-\epsilon)-\lambda_j(k_r)\big).$$

This is seen most often occurring on the real axis, and more rarely away from it.

The second is that for equations with rational exponents or more general functional dependence, this only obtains the branches that are continuously connected to $k = 0$. That is to say, there may be branches that exist for $k \in (a, b)$ with $b > a > 0$ that this approach does not pick up.

3.4.6 Applied to bifurcations of SHE

For the bifurcations that are caused by elements of the continuous dispersion relations discussed in Section 3.2.3 we can formulate an appropriate continuation problem. The formulation for continuation of Turing or dynamic Turing bifurcation is the same, but as the case of the Turing bifurcation is just a simplified version, i.e., $\omega_c = 0$, we neglect that completely. The formulation consists of two pieces, the finding of a turning point of the dispersion, followed by continuation of such a turning point towards $\operatorname{Re}\lambda = 0$.

Turning point of dispersion relation

First, we want to find a turning point of a complex branch of the dispersion relation, recalled from earlier

$$F(\lambda, k, \alpha) = 0, \qquad \text{((3.2.4) revisited)}$$

and taken to be a scalar equation. Since F is a complex equation, to write it in real coordinates, we take $\lambda = \mu + i\omega$, substitute it into the dispersion relation, and split

that into the real and imaginary parts.

$$F^r(\mu, \omega, k, \alpha) = \mathrm{Re}\, F(\mu + i\omega, k, \alpha) = 0$$
$$F^i(\mu, \omega, k, \alpha) = \mathrm{Im}\, F(\mu + i\omega, k, \alpha) = 0$$

We are looking for the turning point in (μ, k) space, so that means that it must satisfy the equalities

$$\mu'(k) = 0 \to F^r_k F^i_\omega - F^i_k F^r_\omega \equiv J(\mu, \omega, k, \alpha) = 0.$$

Thus we consider the state to be $U = (\mu, \omega, k)^T$, and a continuation parameter $\beta = \alpha_1$.

The elements required for continuation of a turning point of the dispersion relation are

$$g(U, \beta) = \begin{bmatrix} F^r(\mu, \omega, k, \alpha) \\ F^i(\mu, \omega, k, \alpha) \\ J(\mu, \omega, k, \alpha) \end{bmatrix} = 0$$
$$\partial_U g(U, \beta) = \begin{bmatrix} \partial_\mu F^r & \partial_\omega F^r & \partial_k F^r \\ \partial_\mu F^i & \partial_\omega F^i_\omega & \partial_k F^i \\ \partial_\mu J & \partial_\omega J & \partial_k J \end{bmatrix} \tag{3.4.5}$$
$$\partial_\beta g(U, \beta) = \begin{bmatrix} \partial_{\alpha_1} F^r \\ \partial_{\alpha_1} F^i \\ \partial_{\alpha_1} J \end{bmatrix}.$$

We note that this notation is hiding the SHE values. In general the SHE must be continued simultaneously to this system of equations, because it is required to fully specify F.

Dynamic Turing bifurcation

We perform continuation of Eq. (3.4.5), until we reach a point with $\mu \approx 0$. At this point, we explicitly set $\mu = 0$, and switch our view of the state to $U = (\omega, k, \alpha_1)$, where the α_1 parameter has been added to make up for the lost degree of freedom in doing this. We take another parameter for continuation $\beta = \alpha_2$, and write

$$g(U, \beta) = \begin{bmatrix} F^r(0, \omega, k, \alpha) \\ F^i(0, \omega, k, \alpha) \\ J(0, \omega, k, \alpha) \end{bmatrix}$$
$$\partial_U g(U, \beta) = \begin{bmatrix} \partial_\omega F^r & \partial_k F^r & \partial_{\alpha_1} F^r \\ \partial_\omega F^i & \partial_k F^i & \partial_{\alpha_1} F^i \\ \partial_\omega J & \partial_k J & \partial_{\alpha_1} J \end{bmatrix} \tag{3.4.6}$$
$$\partial_\beta g(U, \beta) = \begin{bmatrix} \partial_{\alpha_2} F^r \\ \partial_{\alpha_2} F^i \\ \partial_{\alpha_2} J \end{bmatrix},$$

noting the different partial derivatives when compared to Eq. (3.4.5). From this expression, we can refine approximations to the dynamic Turing bifurcation, using just the g and $\partial_U g$ expressions, and then perform continuation in the α_2 parameter.

This approach will pick up dynamic Turing bifurcations, but we are most interested in studying when these are the principal instability of the system. That is, we must look at the rest of the dispersion relation, which must be computed using Section 3.4.5, for example.

3.5 Summary

Above, we presented general formulations for finite and infinite dimensional dynamical systems. We introduced the concept of bifurcations and center manifolds, and briefly discussed the influences of symmetry. We looked in more detail at the specific symmetry studied in this thesis – the square periodic tiling symmetry, $D_4 \ltimes T^2$. And finally the idea of continuation was presented, with its relevant domains of application detailed. Now we move on to using these ideas to study the dynamics of neural field models.

Bibliography

[1] Coombes, S. Waves, bumps, and patterns in neural field theories. *Biological Cybernetics 93*, 2 (2005), 91–108.

[2] Doedel, E. J., Champneys, A. R., Dercole, F., Fairgrieve, T. F., Kuznetsov, Y. A., Oldeman, B., Paffenroth, R., Sandstede, B., Wang, X., and Zhang, C. AUTO-07P: Continuation and bifurcation software for ordinary differential equations, 2008.

[3] Floquet, G. Sur les équations différentielles linéaires à coefficients périodiques. *Annales de l'École Normale Supérieure 12* (1883), 47–88.

[4] Golubitsky, M., and Stewart, I. Hopf Bifurcation in the presence of symmetry. *Archive for Rational Mechanics and Analysis 87*, 2 (1985), 107–165.

[5] Golubitsky, M., and Stewart, I. *The Symmetry Perspective*, 1 ed. Birkhäuser, Basel, 2002.

[6] Govaerts, W. J. F. *Numerical Methods for Bifurcations of Dynamical Equilibria*. Society for Industrial and Applied Mathematics, 2000.

[7] Govaerts, W. J. F., Kuznetsov, Y. A., De Witte, A. V., Dhooge, A., Meijer, H. G. E., and Mestrom, W. Matcont and CL Matcont: Continuation toolboxes in Matlab, 2011.

[8] Hopf, E. Abzweigung einer periodischen Losung von einer stationaren Losung eines Differentialsystems. *Ber. Verh. Saechs. Akad. Wiss. Leipzig, Math. Naturwiss. 94* (1942), 3–22.

[9] Howard, L. N., and Kopell, N. Translation, with editorial comments, of E. Hopf s Abzeigung einer periodischen Losung von einer stationaren Losungeines Differential systems. In *The Hopf Bifurcation and its Applications*, J. Marsden and M. McCracken, Eds. Springer-Verlag, New York, 1978, pp. 163–205.

[10] Keller, H. Numerical Solution of Bifurcation and Nonlinear Eigenvalue Problems. In *Applications of Bifurcation Theory*, P. Rabinowitz, Ed. Academic Press, New York, 1977, pp. 359–384.

[11] Kuznetsov, Y. A. *Elements of Applied Bifurcation Theory*, 2 ed. Applied Mathematical Sciences. Springer, 1998.

[12] Kuznetsov, Y. A. Numerical normalization techniques for all codim 2 bifurcations of equilibria in odes. *SIAM J Numer Anal 36*, 4 (1999), 1104–1124.

[13] Silber, M., and Knobloch, E. Hopf bifurcation on a square lattice. *Nonlinearity 4*, 4 (1991), 1063–1107.

[14] Wiggins, S. *Introduction to Applied Nonlinear Dynamical Systems and Chaos*, 2 ed. Texts in Applied Mathematics. Springer, 2003.

Chapter 4

Analysis of a scalar neural field

4.1 Preliminaries **60**
4.1.1 Integral transforms 60
4.1.2 Firing function 61
4.2 Spatially homogeneous dynamics **61**
4.2.1 Continuation 62
4.2.2 Linearization and dispersion relations 63
4.2.3 Homogeneous dynamics 64
4.3 $D_4 \ltimes T^2$ symmetric Hopf **64**
4.3.1 Finding dynamic Turing bifurcations 64
4.3.2 $D_4 \ltimes T^2$ Normal form 75
4.3.3 Locating degeneracies 75
4.4 Simulation **78**
Bibliography **80**

This chapter will bring the view of dynamical systems from Chapter 3 to the scalar neural field model described in Chapter 2. For this model,

$$u(\mathbf{x},t) = \eta * \big(K \otimes S \circ u(\mathbf{x},t) + p\big), \qquad \text{((2.3.1) revisited)}$$

it will progress through:

- Determining the equations that spatially homogeneous equilibria (SHE) will satisfy,
- Linearization about SHE,
- Finding dispersion relation about SHE,
- Analyzing the unfolding of the dynamic Turing bifurcation that arises, and

- Simulating solutions in the neighbourhood of the bifurcations.

It is mentioned again that the equation is taken on a two dimensional spatial domain $\Omega = \mathbb{R}^2$. The analysis is presented for homogeneous and isotropic problems, but we note that the normal form result will hold for problems with explicit $D_4 \ltimes T^2$ symmetry i.e., if the spatiotemporal connectivity satisfies this symmetry.

Novel results of this chapter are Section 4.3.1, the detection of the dynamic Turing bifurcation from a dispersion relation with irreducible rational exponents, Section 4.3.1 where symbolic expressions for computing the normal form coefficients of the $D_4 \ltimes T^2$ symmetric Hopf bifurcation are derived, and Section 4.4 where the bifurcating solutions are simulated in its neighbourhood.

4.1 Preliminaries

All of the analysis presented in this chapter can be done on the scalar field in its general form, without specifying a connectivity kernel, a synapse, or even a firing function. This is because the model has only spatial and temporal convolutions, which allows for simple representation in Fourier-Laplace space.

For visualizing the results presented here, specific kernels are chosen from those discussed in Section 2.2.2. These will be worked in among the analysis, with the relevant methods from Chapter 3 mentioned whenever they are used.

4.1.1 Integral transforms

First, we define the integral transforms which end up touching all facets of the coming sections, and even find use in the next chapter. These are:

1. The Laplace transform
$$\tilde{\eta}(\lambda) = \int_0^\infty \mathrm{d}s\, \eta(s) e^{-\lambda s}, \tag{4.1.1}$$
2. The Fourier-Laplace transform
$$\widehat{K}(k,\lambda) = \int_{\mathbb{R}^2} \mathrm{d}y_1 \mathrm{d}y_2 \int_0^\infty \mathrm{d}s\, K(\mathbf{y}, s) e^{-(i\mathbf{k}\cdot\mathbf{y} + \lambda s)}. \tag{4.1.2}$$

Fourier and Laplace transforming the scalar model, Eq. (2.3.1), we obtain

$$\widehat{u}(k,\lambda) = \tilde{\eta}(\lambda)\widehat{K}(k,\lambda)\big(\widehat{S \circ u}\big)(k,\lambda) + \widehat{p}(k,\lambda), \tag{4.1.3}$$

where the Fourier-Laplace transform of the composition is interpreted as

$$\big(\widehat{S \circ u}\big)(k,\lambda) = \int_{\mathbb{R}^2} \mathrm{d}y_1 \mathrm{d}y_2 \int_0^\infty \mathrm{d}s\, \big(S \circ u(\mathbf{y}, s)\big) e^{-(i\mathbf{k}\cdot\mathbf{y} + \lambda s)}.$$

Specific kernels

For the alpha function synapse

$$\eta(t) = \alpha^2 t e^{-\alpha t}, \qquad \text{((2.3.5) revisited)}$$

we have its Laplace transform

$$\tilde{\eta}(\lambda) = \frac{1}{(1+\lambda/\alpha)^2}. \tag{4.1.4}$$

For the double exponential connectivity, Eq. (2.3.8), combined with the constant, homogeneous, isotropic and space-dependent delay, Eq. (2.3.6), our specific spatiotemporal connectivity is

$$K(\mathbf{x},t) = \frac{1}{2\pi}\left(a_e e^{-\|\mathbf{x}\|} - a_i r^2 e^{-r\|\mathbf{x}\|}\right)\delta\left(t + \frac{\|\mathbf{k}\|}{c}\right), \tag{4.1.5}$$

and its Fourier-Laplace transform is.

$$\widehat{K}(k,\lambda) = \frac{1+\lambda/c}{\left((1+\lambda/c)^2 + k^2\right)^{3/2}} a_e - \frac{r+\lambda/c}{\left((r+\lambda/c)^2 + k^2\right)^{3/2}} r^2 a_i. \tag{4.1.6}$$

4.1.2 Firing function

With the firing function as the sigmoid

$$S(u) = \frac{S_{max}}{1 + e^{-C(u-\theta)}}, \qquad \text{((2.3.2) revisited)}$$

its derivatives satisfy

$$\begin{aligned} S'(u) &= CS(u)\left(1 - \frac{S(u)}{S_{max}}\right) \\ S''(u) &= \frac{C^2 S^2(u)}{S_{max}}\left(1 - \frac{S(u)}{S_{max}}\right)(1 - S(u)) \\ S'''(u) &= \frac{C^3 S^3(u)}{S_{max}^2}\left(1 - \frac{S(u)}{S_{max}}\right)\left(3S^2(u) - \big(3 + 2S_{max}\big)S(u) + S_{max}\right). \end{aligned} \tag{4.1.7}$$

4.2 Spatially homogeneous dynamics

Spatially homogeneous equilibria (SHE) of the neural field are very straightforward to determine. We denote the SHE as u_0, and also consider the extraneous input to

be constant in space and time $p(\mathbf{x}, t) = p_0$. Subbing these into the scalar model gives

$$\begin{aligned} u_0 &= \eta * \left(K \otimes S \circ u_0 + p_0\right) \\ &= \int_{-\infty}^{t} \mathrm{d}\tau\, \eta(t-\tau) \left(S(u_0) \int_{-\infty}^{\infty} \mathrm{d}t' \int_{\Omega} \mathrm{d}x_1' x_2'\, K\left(\mathbf{x}-\mathbf{x}', t-t'\right) \; + \; p_0 \right) \\ &= \tilde{\eta}(0) \left(S(u_0) \widehat{K}(0,0) + p_0 \right). \end{aligned} \tag{4.2.1}$$

This is just a single equation. For the sigmoidal form of Eq. (2.3.2), it is easy to see that u_0 can have either 1, 2, or 3 solutions for a given p_0 value, depending on the parameters in S, η, and K.

4.2.1 Continuation

Because it is just a single equation, the continuation of the SHE is almost trivial. Looking back to Section 3.4.2, we associate the state with $U = u_0$, and consider all of the parameters as the set β, so we have

$$\begin{aligned} g(u_0, \beta) &= u_0 - \tilde{\eta}(0) \left(S(u_0) \widehat{K}(0,0) + p_0 \right) \\ \partial_{u_0} g(u_0, \beta) &= 1 - \gamma_1 \tilde{\eta}(0) \widehat{K}(0,0) \end{aligned} \tag{4.2.2}$$

The derivative with respect to a specific parameter can also be easily expressed. We can consider the parameter set to be composed of four different types of parameters, $\beta = \{p_0, \beta^{syn}, \beta^{con}, \beta^{sig}\}$, the external forcing, the synaptic parameters, the connectivity parameters, and the sigmoidal parameters respectively. Identifying one of these as our continuation parameter gives different possibilities for the parameter derivative:

$$\begin{aligned} \partial_{p_0} g(u_0, \beta) &= -\tilde{\eta}(0), \\ \partial_{\beta^{syn}} g(u_0, \beta) &= -\left(S(u_0) \widehat{K}(0,0) + p_0 \right) \partial_{\beta^{syn}} \tilde{\eta}(0,0), \\ \partial_{\beta^{con}} g(u_0, \beta) &= -\tilde{\eta}(0) S(u_0) \partial_{\beta^{con}} \widehat{K}(0,0), \\ \partial_{\beta^{sig}} g(u_0, \beta) &= -\tilde{\eta}(0) \widehat{K}(0,0) \partial_{\beta^{sig}} S(u_0). \end{aligned} \tag{4.2.3}$$

For the specific functions chosen for each piece of the model, a particular equation we can look at for the SHE is

$$u_0 - (a_e - a_i) S(u_0) - p_0 = 0 \tag{4.2.4}$$

As it was mentioned that there is the possibility of 1, 2, or 3 SHE solutions for a given parameter set, this implies that a continuation of u_0 may result in fold bifurcations. A pseudoarclength continuation in the p_0 parameter shows this in Figure 4.1.

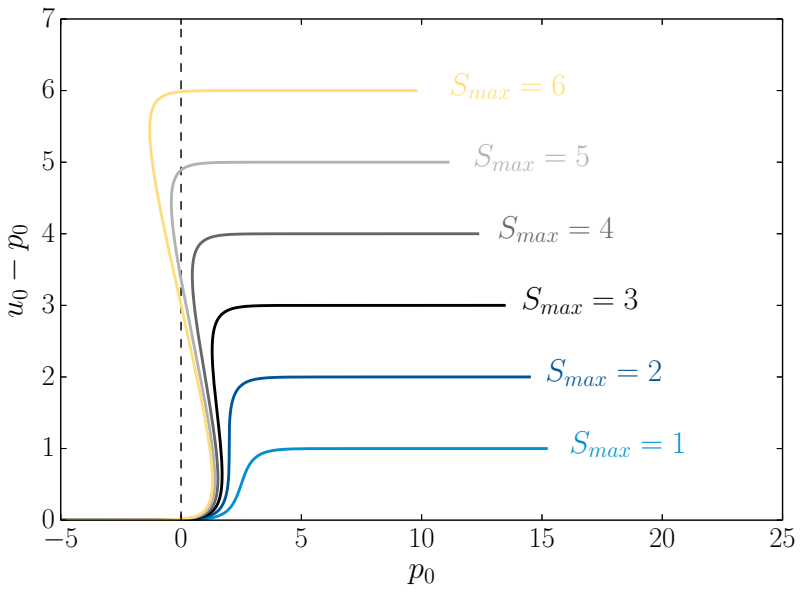

Figure 4.1: Continuation of SHE in the scalar model, Eq. (4.2.4), demonstrating the possibility of multiple solutions. Parameters are: $a_e = 41; a_i = 40; C = 2, \theta = 3$, and S_{max} set to different values for each curve. The transition from seeing no folds ($S_{max} = 2$) to two folds ($S_{max} = 3$) implies that we would see the codimension 2 *cusp* bifurcation in this region.

4.2.2 Linearization and dispersion relations

Now we linearize the scalar neural field equation about a general solution $u_0(\mathbf{x}, t)$ by subbing $u_0(\mathbf{x}, t) + \epsilon u_1(\mathbf{x}, t)$ into the model, and keeping terms proportional to ϵ. The result, after Taylor expanding the sigmoid as well, is

$$u_1(\mathbf{x}, t) = \eta * K \otimes \big(S' \circ u_0(\mathbf{x}, t)\big) u_1, \tag{4.2.5}$$

which simplifies when u_0 is a SHE

$$u_1(\mathbf{x}, t) = \gamma_1 \eta * K \otimes u_1, \quad \gamma_1 = S'(u_0).$$

A convenient notation to use for the upcoming nonlinear analysis is to rewrite the linear equation to be

$$\mathcal{L}(\gamma_1) u_1 \equiv (1 - \gamma_1 \eta * K \otimes)\, u_1 = 0 \tag{4.2.6}$$

With this linear equation, we take the ansatz

$$u_1(\mathbf{x}, t) = e^{i\mathbf{k}\cdot\mathbf{x} + \lambda t},$$

which gives the dispersion relation

$$1 - \gamma_1 \tilde{\eta}(\lambda) \widehat{K}(k, \lambda) = 0. \tag{4.2.7}$$

We mention again that for homogeneous and isotropic spatial connections, the dis-

persion relation only depends on the norm of $\mathbf{k}$.

A very useful feature of this dispersion relation, is that γ_1 can be varied independently of the SHE. That is, we can fix parameters in the synapses η and the spatiotemporal connectivity K, then look at the dispersion relation for varying γ_1. Once an *interesting* value of γ_1 is obtained, we can move back to the SHE equation and determine u_0, p_0, and the sigmoidal parameters such that the model is at the interesting state.

The specific dispersion relation we visualize is in fact given by

$$(1+\lambda/\alpha)^2 - \gamma_1 \left[\frac{1+\lambda/c}{\left((1+\lambda/c)^2+k^2\right)^{3/2}} a_e - \frac{r+\lambda/c}{\left((r+\lambda/c)^2+k^2\right)^{3/2}} r^2 a_i \right] = 0, \quad (4.2.8)$$

with continuation applied as discussed in Section 3.4.5. Various dispersion relations for different parameter sets are shown in Figures 4.2–4.7.

With continuous dispersion relations computed, we can now turn our attention to stability of the SHE with respect to spatially homogeneous modes as well as Fourier modes with wavenumber k.

4.2.3 Homogeneous dynamics

For stability with respect to spatially homogeneous modes, we simply take $k = 0$ in our dispersion relation

$$1 - \gamma_1 \tilde{\eta}(\lambda) \widehat{K}(0,\lambda) = 0. \quad (4.2.9)$$

For a discrete set of temporal eigenvalues satisfying this equation, we can define the stable, unstable, and center subspaces as was done for the finite dimensional dynamical system.

For our specific functions, the stability of the homogeneous dynamics is determined by

$$(1+\lambda/\alpha)^2 - \gamma_1 \left[\frac{1+\lambda/c}{|1+\lambda/c|^3} a_e - \frac{r+\lambda/c}{|r+\lambda/c|^3} r^2 a_i \right] = 0, \quad (4.2.10)$$

where we have left it in this form since $\lambda \in \mathbb{C}$. Finding solutions to this is simpler than the general k-dependent dispersion relation of Eq. (4.2.10).

4.3 $D_4 \ltimes T^2$ symmetric Hopf

4.3.1 Finding dynamic Turing bifurcations

Once we have the homogeneous mode eigenvalues, $\lambda_j(0)$, we can perform continuation in k to obtain the distinct branches $\lambda_j(k) \in \Lambda^{CONT}$. The process for doing this, described in Section 3.4.5, can result in the continuous dispersion relations as shown in Figures 4.2– 4.5.

The Turing and dynamic Turing bifurcations can now be detected by analysis of these dispersion relations. In fact, due to the form of the dispersion relation for this

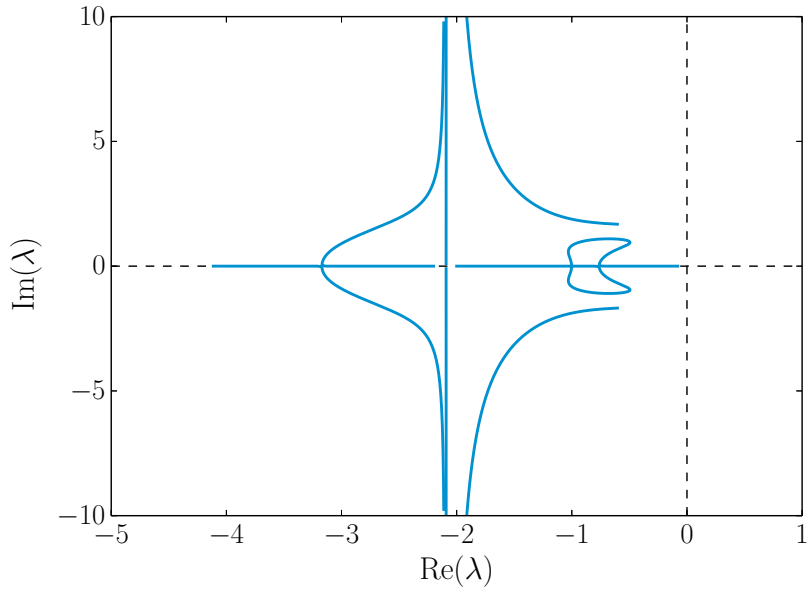

Figure 4.2: Continuous dispersion relation for parameters: $a_e = 41; a_i = 40; r = 1.1; c = 2; \alpha = 1; \gamma_1 = 0.6$.

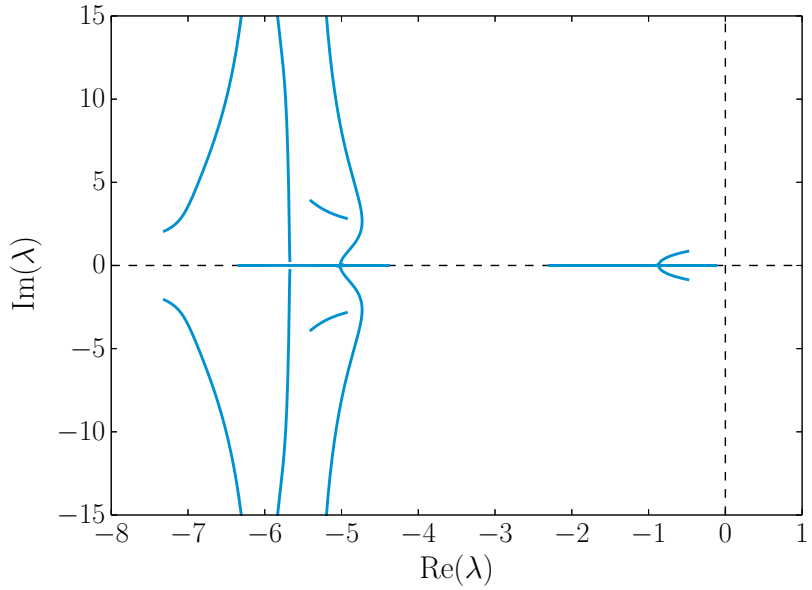

Figure 4.3: Continuous dispersion relation for parameters: $a_e = 39; a_i = 40; r = 0.9; c = 6; \alpha = 1; \gamma_1 = 0.4$.

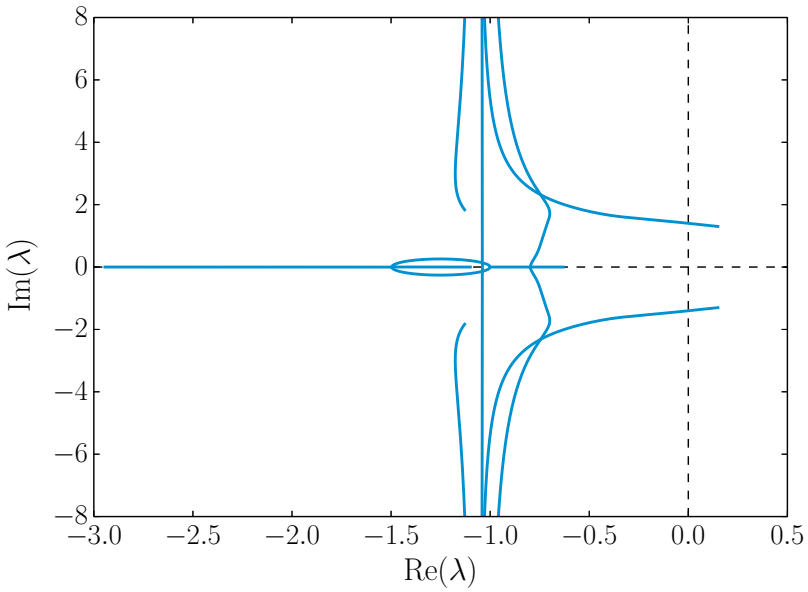

Figure 4.4: Continuous dispersion relation for parameters: $a_e = 30; a_i = 40; r = 1.1; c = 1; \alpha = 1; \gamma_1 = 0.6$. The unstable portion corresponds to modes with $k \in [0, 0.962)$. The instability of bulk oscillations is typical for parameter sets with small transmission speeds.

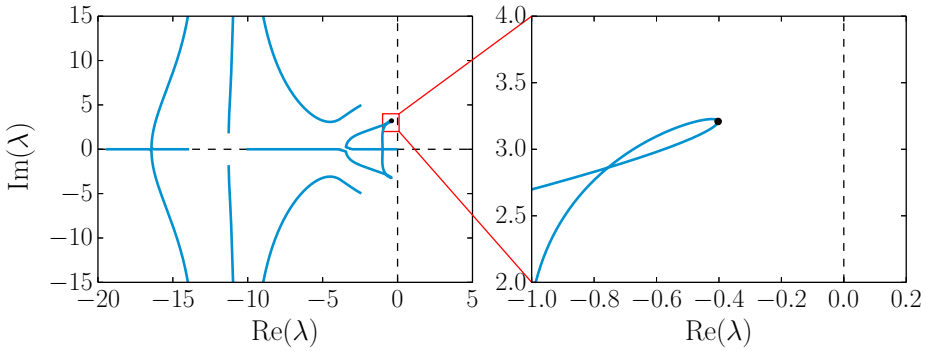

Figure 4.5: Continuous dispersion relation for parameters: $a_e = 121; a_i = 120; r = 1.4; c = 10; \alpha = 1; \gamma_1 = 0.5$. The right panel is a zoom of the left. The black dot represents a point in Λ^{CONT} that may produce a dynamic Turing bifurcation on increasing γ_1.

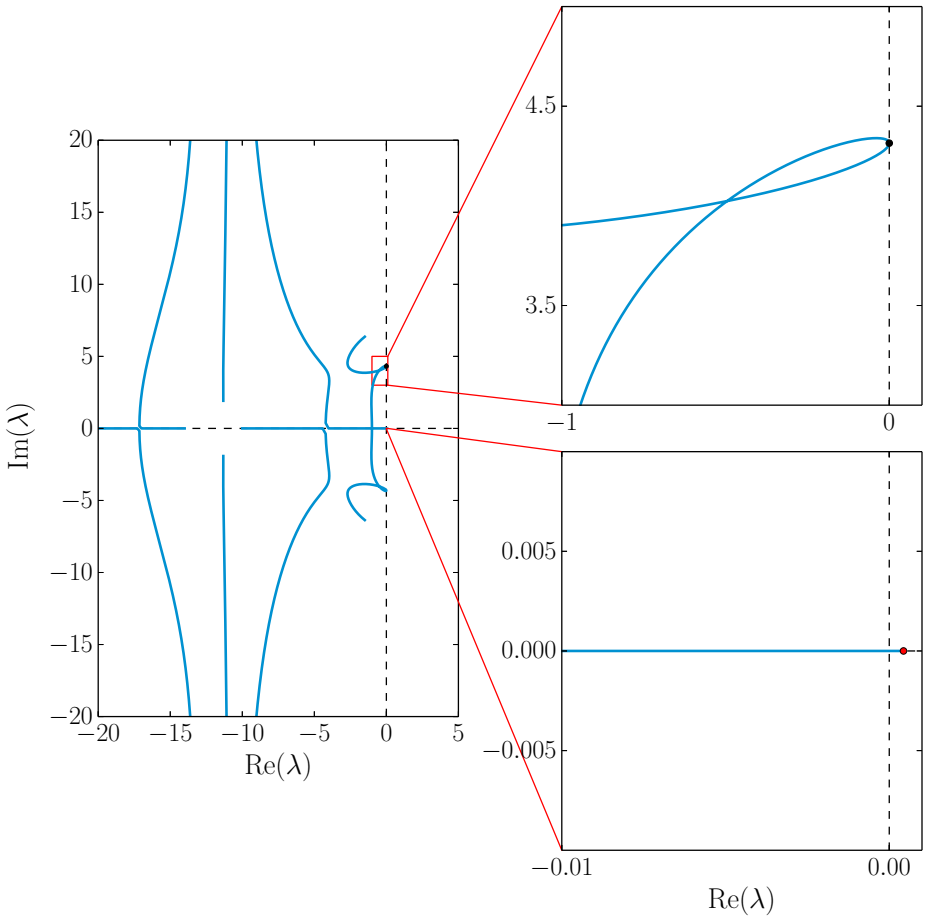

Figure 4.6: Continuous dispersion relation for parameters: $a_e = 121; a_i = 120; r = 1.4; c = 10; \alpha = 1; \gamma_1 = 1.003950769$. The right panels show zooms of the left. The black dot represents a point in Λ^{CONT} that would produce a dynamic Turing bifurcation if the rest of dispersion relation was stable. The red dot shows the maximum extent of an unstable branch.

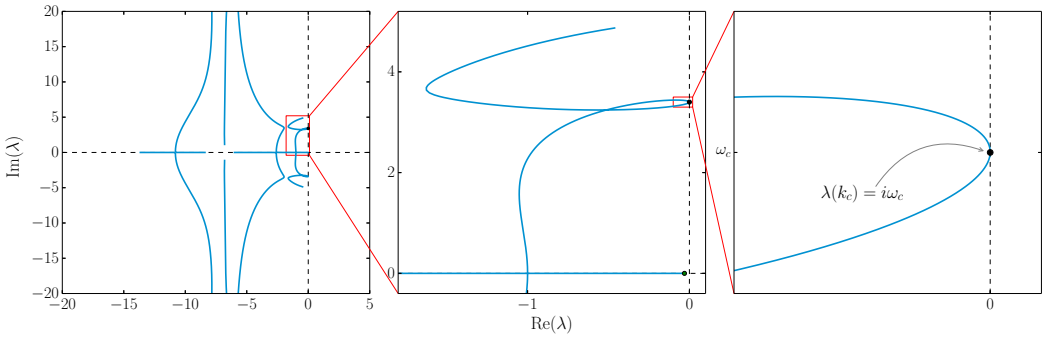

Figure 4.7: Continuous dispersion relation for parameters: $a_e = 121; a_i = 120; r = 1.4; c = 6; \alpha = 1; \gamma_1 = \gamma_c \approx 0.689077$. Progressive zoom from the left. The black dot represents a point in Λ^{CONT} that produces a dynamic Turing bifurcation. The green dot in the middle frame shows that decreasing the transmission speed c from Figure 4.6 has stabilized the real branch. The right-most level shows that this is indeed the dispersion behaviour depicted in the schematic view of Figure 3.2.

model, there is a simple way for detecting Turing bifurcations, which proceeds as follows.

1. Set $\lambda = 0$ in the dispersion relation

$$\frac{1}{\gamma_1} = \tilde{\eta}(0)\widehat{K}(k, 0) \tag{4.3.1}$$

2. If

$$\max_{k>0} \tilde{\eta}(0)\widehat{K}(k, 0) > 0,$$

Then a Turing bifurcation exists for

$$k_c^{Tu} = \arg\max_k \eta(0)\widehat{K}(k, 0), \tag{4.3.2}$$

with $\gamma_1 = \gamma_c^{Tu}$.

A variation of this method was initially applied to finding Turing bifurcations in one dimensional neural fields by Hutt et al. [3]. Its generalization to the two dimensional homogeneous isotropic case is trivial.

However, we are not interested in the formation of stationary patterns, so we do not get so lucky with such a simple algorithm. For instance, when we set $\lambda = i\omega_c$, $\omega_c > 0$, and split the dispersion relation into real and imaginary parts, we obtain the system of two equations

$$\begin{aligned} 1 - \gamma_c \operatorname{Re} \tilde{\eta}(i\omega_c)\widehat{K}(k_c^{dTu}, i\omega_c) = 0 \\ \gamma_c \operatorname{Im} \tilde{\eta}(i\omega_c)\widehat{K}(k_c^{dTu}, i\omega_c) = 0. \end{aligned} \tag{4.3.3}$$

For a one dimensional neural field, this can be applied successfully to find $\omega_c(k_c^{dTu})$ as in Venkov et al. [9] and Hutt et al. [3], because the resulting expressions are polynomial in ω and k. In two dimensional space, it is rare to see dispersion relations that are

polynomial, so applying this approach leaves us with complicated expressions such as

$$\begin{aligned}\frac{1-(\omega/\alpha)^2}{\gamma_1} &= \left[\left(\cos\left(\frac{3}{2}\theta_1\right)+\frac{\omega}{c}\sin\left(\frac{3}{2}\theta_1\right)\right)a_e R_1^{-3/2} - \right.\\ &\qquad \left.\left(r\cos\left(\frac{3}{2}\theta_r\right)+\frac{\omega}{c}\sin\left(\frac{3}{2}\theta_r\right)\right)a_i r^2 R_r^{-3/2}\right],\\ \frac{(2/\alpha)\omega}{\gamma_1} &= \left[\left(\frac{\omega}{c}\cos\left(\frac{3}{2}\theta_1\right)-\sin\left(\frac{3}{2}\theta_1\right)\right)a_e R_1^{-3/2} - \right.\\ &\qquad \left.\left(\frac{\omega}{c}\cos\left(\frac{3}{2}\theta_r\right)-r\sin\left(\frac{3}{2}\theta_r\right)\right)a_i r^2 R_r^{-3/2}\right],\end{aligned} \tag{4.3.4}$$

with (noting the subscripts)

$$\begin{aligned}R_z &= \sqrt{(z^2+k^2-\omega^2/c^2)^2+(2\omega/c)^2 z^2},\\ \theta_z &= \arctan\frac{2\omega z/c}{z^2+k^2-\omega^2/c^2}.\end{aligned}$$

This is the expression that results for our specific choice of synapse and connectivities, and even with attempted simplification through the application of trig identities, it remains difficult to work with. This is why the continuation approach of Section 3.4.6 was discussed.

With continuous dispersion curves computed as in Figure 4.5, we choose a turning point that looks like it has the potential to generate a dynamic Turing bifurcation as the primary instability. Such a point is displayed as the black dot in this figure. The turning point is continued by applying Eq. (3.4.5) in the parameter γ_1, until we get it to $\lambda = 0$ as in Figure 4.6.

However, the SHE is already unstable at this point, looking at the branch on the real axis with $\max \operatorname{Re}\lambda_j > 0$. So, we switch to a new parameter, the transmission speed c, and perform continuation using Eq. (3.4.6) until $\max \operatorname{Re}\lambda_j < 0$ for all of the branches except the one causing the dynamic Turing instability. The result is the parameter set given in Table 4.1, with continuous dispersion relation in Figure 4.7.

With a principal dynamic Turing bifurcation located, we now perform our restriction to square symmetric modes, and try to compute the normal form coefficients.

At the dynamic Turing bifurcation, the bifurcation parameter, the wave number and the angular frequency take critical values γ_c, k_c and ω_c, respectively. Correspondingly, the critical wavenumber and critical frequency also define a length scale and time scale at the bifurcation point $L_c = 2\pi/k_c$ and $T_c = 2\pi/\omega_c$, respectively. Again we stress that in general on $\mathbb{R}^2$ the dimension of the nullspace of $\mathcal{L}(\gamma_c)$ is infinite dimensional due to the degree of freedom in k.

On the domain $[0, L_c]^2 \times [0, T_c]$ with periodic boundary conditions, it is very natural

Parameter	Value
a_e	121
a_i	120
r	1.4
c	6.0
α	1.0
$\gamma_1 = \gamma_c$	0.689077
ω_c	3.400300
k_c	1.089196

Table 4.1: Parameters that will display a dynamic Turing bifurcation for the specific synapse and connectivity, Eqs. (2.3.5) and (4.1.5). Important to note that only the synapse and connectivity parameters need be defined and γ_1 can be taken as its own distinct parameter.

to define the eigenfunctions

$$\begin{aligned} \phi_1 &= e^{i(\omega_c t + k_c x_1)}, \\ \phi_2 &= e^{i(\omega_c t - k_c x_1)}, \\ \phi_3 &= e^{i(\omega_c t + k_c x_2)}, \\ \phi_4 &= e^{i(\omega_c t - k_c x_2)}, \end{aligned} \tag{4.3.5}$$

which can be taken as a basis for the nullspace of $\mathcal{L}(\gamma_c)$

$$\ker \mathcal{L}(\gamma_c) = \operatorname{span}\left\{\phi_1, \phi_2, \phi_3, \phi_4, \bar{\phi}_1, \bar{\phi}_2, \bar{\phi}_3, \bar{\phi}_4\right\},$$

with the bars denoting complex conjugation.

The linear analysis in Section 4.2.2 allows us to extract the bifurcation type by the computation of the eigenvalue spectrum of the corresponding linear operator. However, the linear analysis leads to degenerate solutions and does not allow us to determine the dynamic spatial patterns that emerge in the neighbourhood of the bifurcation. To extract criteria for the specific patterns, it is necessary to perform a weakly nonlinear analysis. To this end, one considers the linear eigenbasis of the nullspace of $\mathcal{L}(\gamma_c)$ and investigates the nonlinear interaction of the system projections on this basis.

Performing a center manifold reduction on this problem should be possible as well, such as through an extension of the rigorous results in Veltz & Faugeras [8] to two-dimensional space. However this is beyond the scope of this thesis as our end goal is simply to obtain behaviour of the square symmetric modes in the neighbourhood of the bifurcation. We do expect that a center manifold reduction will result in the same expressions as the weakly nonlinear analysis, as seen in Folias [1], where Hopf bifurcations of localized solutions were studied without transmission delays.

To perform weakly nonlinear analysis at a dynamic Turing bifurcation, it is neces-

sary to consider higher order perturbations from the equilibrium state u_0 beyond the linear limit. In particular, the subsequent analysis takes into account terms of cubic order of the transfer function S leading to a model of up to 3rd order perturbations

$$S(u) = S(u_0) + \gamma_1 (u - u_0) + \gamma_2 (u - u_0)^2 + \gamma_3 (u - u_0)^3 + \mathcal{O}\left((u - u_0)^4\right), \quad (4.3.6)$$

with $\gamma_n = \partial_u^n S(u_0)/n!$ evaluated at the homogeneous equilibrium u_0.

Multiple time scales

Just beyond a dynamic Turing bifurcation, dominant eigenmodes grow slowly in amplitude. This leads naturally to the idea of identifying different time scales in the system. The behaviour that occurs at all but the slowest of time scales can be discarded to obtain information about the envelopes, or amplitudes, of the slowest scale.

If we Taylor expand the dispersion curve, Eq. (4.2.7), about the temporal eigenvalue with maximum real part, we obtain $\mathrm{Re}(\lambda) \sim \gamma_1 - \gamma_c$ and $\mathrm{Im}(\lambda) \sim k - k_c \sim \sqrt{\gamma_1 - \gamma_c}$ near the dynamic Turing bifurcation. For $\gamma_1 \neq \gamma_c$, emergent patterns can thus be written as an infinite sum of unstable modes of the form

$$e^{\mu_0(\gamma_1-\gamma_c)t} e^{i\sqrt{\gamma_1-\gamma_c}\mathbf{k}_0\cdot\mathbf{x}} e^{i(\omega_c t + \mathbf{k}_c\cdot\mathbf{x})},$$

with μ_0 and $\mathbf{k}_0$ some unknown constants in the proportionalities. If we choose a scaling parameter $\epsilon \sim \sqrt{\gamma_1 - \gamma_c}$, then with ϵ small, we can identify the fast eigenmodes as $e^{i(\omega_c t + \mathbf{k}_c\cdot\mathbf{x})}$, and the slow modulations of the form $e^{\mu_0\epsilon^2 t} e^{i\epsilon\mathbf{k}_0\cdot\mathbf{x}}$.

We define scaled parameters, $\boldsymbol{\chi} = \epsilon\mathbf{x}$ and $\tau = \epsilon^2 t$ according to this reasoning, and also include an intermediate time scale $\theta = \epsilon t$ which assists in stepping through some integrals in the perturbative analysis as shown in Appendix A.1.1. Finally the analysis permits us to write solutions in the form $A(\boldsymbol{\chi}, \theta, \tau) e^{i(\omega_c t + \mathbf{k}_c\cdot\mathbf{x})}$, with A containing everything we do not know about the slower scales. With wave vectors $(\pm k_c, 0)^T$ and $(0, \pm k_c)^T$, these are linear combinations of the basis functions spanning $\ker \mathcal{L}(\gamma_c)$ given in Eq. (4.3.5). In addition, the individual amplitudes depend on a single scaled spatial coordinate only rather than both of them, i.e., $A_1 = A_1(\chi_1, \theta, \tau)$.

Now, we take a perturbation of the solution to the full model, Eq. (2.3.1), in the form

$$u(\mathbf{x}, t) - u_0 = \sum_{n=1}^{\infty} \epsilon^n u_n (\mathbf{x}, t, \boldsymbol{\chi}, \theta, \tau). \quad (4.3.7)$$

with unknown functions u_n. Inserting this ansatz into the model equation, we can pull out the equations for each order of ϵ

$$\begin{aligned}
&(1 - \gamma_c M_0) u_1 = g_1 = 0, \\
&(1 - \gamma_c M_0) u_2 = g_2 = \gamma_2 M_0 u_1^2 + \gamma_c M_1 u_1, \\
&(1 - \gamma_c M_0) u_3 = g_3 = M_0 \left(2\gamma_2 u_1 u_2 + \gamma_3 u_1^3 + \delta u_1\right) + M_1 \left(\gamma_c u_2 + \gamma_2 u_1^2\right) + \gamma_c M_2 u_1.
\end{aligned} \quad (4.3.8)$$

where $g_n(u_0, u_1, \ldots, u_{n-1})$ is a shorthand notation for the right hand sides, and

$\delta \equiv (\gamma_1 - \gamma_c)/\epsilon^2$, a scaled distance from the bifurcation. The M_i operators are defined as

$$\begin{aligned}
M_0 =& \eta * K \otimes, \\
M_1 =& -\eta * \left(x_1 K \otimes \frac{\partial}{\partial \chi_1} + x_2 K \otimes \frac{\partial}{\partial \chi_2} \right) - (t\eta * K + \eta * tK) \otimes \frac{\partial}{\partial \theta}, \\
M_2 =& \frac{1}{2}\eta * \left(x_1^2 K \otimes \frac{\partial^2}{\partial \chi_1^2} + x_2^2 K \otimes \frac{\partial^2}{\partial \chi_2^2} \right) + \eta * x_1 x_2 K \otimes \frac{\partial}{\partial \chi_1}\frac{\partial}{\partial \chi_2} \\
&+ t\eta * \left(x_1 K \otimes \frac{\partial}{\partial \chi_1} + x_2 K \otimes \frac{\partial}{\partial \chi_2} \right) \frac{\partial}{\partial \theta} \\
&+ \eta * t \left(x_1 K \otimes \frac{\partial}{\partial \chi_1} + x_2 K \otimes \frac{\partial}{\partial \chi_2} \right) \frac{\partial}{\partial \theta} \\
&+ \frac{1}{2}\left(t^2 \eta * K + 2t\eta * tK + \eta * t^2 K \right) \otimes \frac{\partial^2}{\partial \theta^2} \\
&+ (t\eta * K + \eta * tK) \otimes \frac{\partial}{\partial \tau},
\end{aligned} \tag{4.3.9}$$

with details of their computation given in Appendix A.1.1.

Noticing that the operator on the left hand side of (4.3.8) is identical to $\mathcal{L}(\gamma_c)$ in all orders, we see that our perturbative solutions originate from the kernel of $\mathcal{L}(\gamma_c)$. In its general form, we write

$$u_1(\mathbf{x}, t) = \sum_{i=1}^{4} \left(A_i \phi_i + \bar{A}_i \bar{\phi}_i \right) \tag{4.3.10}$$

so that now the unknowns in the problem are the amplitudes $A_1(\chi_1, \theta, \tau)$, $A_2(\chi_1, \theta, \tau)$, $A_3(\chi_2, \theta, \tau)$, and $A_4(\chi_2, \theta, \tau)$ which are functions of the scaled independent variables. By virtue of the structure of the perturbation solutions, the Fredholm alternative can be applied to find equations for these amplitudes.

Fredholm alternative

The form of the perturbation expansion is

$$\mathcal{L} u_n = g_n(u_1, u_2, \ldots, u_{n-1}),$$

such that the right hand side always contains known quantities. Thus to construct solutions that are a finite truncation of the system, we just need to know the inverse of $\mathcal{L}$. The Fredholm alternative may be generalized from matrices to include general linear operators [2]. Applying this generalization to $\mathcal{L}$ will put solvability conditions on the g_n, which will lead to conditions on the amplitudes.

Considering the basis on the square periodic domain that we have already written (4.3.10), we notice that this solution is also periodic in time. Thus, we are concerning ourselves with the domain $\Lambda = [0, 2\pi/k_c]^2 \times [0, 2\pi/\omega_c]$. To apply the Fredholm

alternative, we define the inner product to be

$$\langle u, v\rangle = \frac{k_c^2\omega_c}{8\pi^3}\int_\Lambda \mathrm{d}x_1\mathrm{d}x_2\mathrm{d}t\,\bar{u}(\mathbf{x},t)v(\mathbf{x},t). \tag{4.3.11}$$

This definition is chosen such that our basis for the nullspace (4.3.5) is orthonormal, $\langle\phi_i,\phi_j\rangle = \delta_{ij}$.

Under this inner product, the adjoint to $\mathcal{L}$ is given by $\mathcal{L}^* = 1-\gamma_c\eta(-t)*K(\mathbf{x},-t)\otimes$. Since the dispersion relation, Eq. (4.2.7), is invariant under time reversal $t\to -t$, $\mathcal{L}$ and $\mathcal{L}^*$ have the same nullspace.

The Fredholm alternative states that for all $\mathcal{L}u = g$ to have a solution for singular $\mathcal{L}$, it must hold that $\langle v, g\rangle = 0$ for all $v\in\ker\mathcal{L}$. In terms of our situation, this means that computing the inner products

$$\langle\phi_i, g_n\rangle = 0,\quad i = 1\ldots 4, n = 1,2,\ldots, \tag{4.3.12}$$

will put solvability conditions on the amplitudes A_i.

For the first nontrivial equation, and looking specifically at ϕ_1, we obtain

$$\begin{aligned}\langle\phi_1,g_2\rangle = 0 &= \gamma_2\langle\phi_1, M_0u_1^2\rangle + \gamma_c\langle\phi_1, M_1u_1\rangle\\ &= \gamma_2\tilde{\eta}\widehat{K}\langle\phi_1,u_1^2\rangle + \gamma_c\left(-\tilde{\eta}\frac{\partial}{\partial ik_1}\frac{\partial}{\partial\chi_1}\widehat{K} + \frac{\partial}{\partial i\omega}\frac{\partial}{\partial\theta}\tilde{\eta}\widehat{K}\right)\langle\phi_1,u_1\rangle\\ &= \left(-\tilde{\eta}\frac{\partial}{\partial ik_1}\frac{\partial}{\partial\chi_1}\widehat{K} + \frac{\partial}{\partial i\omega}\frac{\partial}{\partial\theta}\tilde{\eta}\widehat{K}\right)A_1\\ &= \left(\frac{\partial}{\partial\theta} - v_{g1}\frac{\partial}{\partial\chi_1}\right)A_1\end{aligned} \tag{4.3.13}$$

where $v_{g1} = \partial\omega/\partial k_1|_{\mathbf{k}=(k_c,0)^T}$ can be considered a group velocity, and the Laplace and Fourier-Laplace transforms are evaluated at the critical arguments. Going from the 1st to 2nd line in Eq. (4.3.13) is detailed in Appendix A.1.2. Going from the 2nd to 3rd line in (4.3.13) makes use of $\langle\phi_i,u_1^2\rangle = 0$, and $\langle\phi_i,u_1\rangle = A_i$. The final line of (4.3.13) has a solution that restricts how A_1 depends on its arguments. Performing similar calculation steps with the other basis functions leads to restrictions on all of the amplitudes

$$\begin{aligned}A_1(\chi_1,\theta,\tau) &= A_1(\chi_1+v_{g1}\theta,\tau)\equiv A_1(\xi_1,\tau)\\ A_2(\chi_1,\theta,\tau) &= A_2(\chi_1-v_{g1}\theta,\tau)\equiv A_2(\xi_2,\tau)\\ A_3(\chi_2,\theta,\tau) &= A_3(\chi_2+v_{g2}\theta,\tau)\equiv A_3(\xi_3,\tau)\\ A_4(\chi_2,\theta,\tau) &= A_4(\chi_2-v_{g2}\theta,\tau)\equiv A_4(\xi_4,\tau),\end{aligned}$$

where $v_{g2} = \partial\omega/\partial k_2|_{\mathbf{k}=(0,k_c)^T} = v_{g1}\equiv v_g$, and note the relative coordinates ξ_i introduced by our abuse of notation

$$\begin{aligned}\xi_1 &= \chi_1 + v_{g1}\theta,\\ \xi_2 &= \chi_1 - v_{g1}\theta,\\ \xi_3 &= \chi_2 + v_{g2}\theta,\\ \xi_4 &= \chi_2 - v_{g2}\theta.\end{aligned}$$

Calculating $\langle \phi_i, g_3 \rangle$ requires more steps. In particular, there is the inner product $\langle \phi_i, u_1^3 \rangle$ which requires the cube of the assumed solution (4.3.10), and then there are $\langle \phi_i, u_2 \rangle$ and $\langle \phi_i, u_1 u_2 \rangle$ which both require an expression for u_2 before they can be evaluated, see Appendix A.1.2 again for details. Eventually, we gain equations for all four amplitudes

$$\begin{aligned}\frac{\partial A_1}{\partial \tau} &= a_0 A_1 + A_1 \left[a_1 \langle |A_2|^2 \rangle_2 + a_2 \left(|A_1|^2 + \langle |A_2|^2 \rangle_2 \right) + a_3 \left(\langle |A_3|^2 \rangle_3 + \langle |A_4|^2 \rangle_4 \right) \right] + \\ &\quad + a_4 \langle \bar{A}_2 \rangle_2 \langle A_3 \rangle_3 \langle A_4 \rangle_4 + a_5 \frac{\partial^2 A_1}{\partial \xi_1^2},\end{aligned} \tag{4.3.14}$$

$$\begin{aligned}\frac{\partial A_2}{\partial \tau} &= a_0 A_2 + A_2 \left[a_1 \langle |A_1|^2 \rangle_1 + a_2 \left(\langle |A_1|^2 \rangle_1 + |A_2|^2 \right) + a_3 \left(\langle |A_3|^2 \rangle_3 + \langle |A_4|^2 \rangle_4 \right) \right] + \\ &\quad + a_4 \langle \bar{A}_1 \rangle_1 \langle A_3 \rangle_3 \langle A_4 \rangle_4 + a_5 \frac{\partial^2 A_2}{\partial \xi_2^2}\end{aligned} \tag{4.3.15}$$

$$\begin{aligned}\frac{\partial A_3}{\partial \tau} &= a_0 A_3 + A_3 \left[a_1 \langle |A_4|^2 \rangle_4 + a_2 \left(|A_3|^2 + \langle |A_4|^2 \rangle_4 \right) + a_3 \left(\langle |A_1|^2 \rangle_1 + \langle |A_2|^2 \rangle_2 \right) \right] + \\ &\quad + a_4 \langle \bar{A}_4 \rangle_4 \langle A_1 \rangle_1 \langle A_2 \rangle_2 + a_5 \frac{\partial^2 A_3}{\partial \xi_3^2}\end{aligned} \tag{4.3.16}$$

$$\begin{aligned}\frac{\partial A_4}{\partial \tau} &= a_0 A_4 + A_4 \left[a_1 \langle |A_3|^2 \rangle_3 + a_2 \left(\langle |A_3|^2 \rangle_3 + |A_4|^2 \right) + a_3 \left(\langle |A_1|^2 \rangle_1 + \langle |A_2|^2 \rangle_2 \right) \right] + \\ &\quad + a_4 \langle \bar{A}_3 \rangle_3 \langle A_1 \rangle_1 \langle A_2 \rangle_2 + a_5 \frac{\partial^2 A_4}{\partial \xi_4^2}\end{aligned} \tag{4.3.17}$$

where the angle brackets $\langle \cdot \rangle_i$ indicate an average. The subscript i of these brackets indicate which ξ_i has been averaged over. As an example, we can look at patterns periodic in ξ_i, with period P_i, with the average given by

$$\langle X \rangle_i = \frac{1}{P_i} \int_0^{P_i} X \mathrm{d}\xi_i. \tag{4.3.18}$$

The parameters a_i of Eqs. (4.3.14) to (4.3.17) are given by

$$\begin{aligned}a_0 &= -\delta D \\ a_1 &= -D \left[2\gamma_2^2 \left(2C_{200} + 2C_{020} - C_{220} \right) + 3\gamma_3 \right] \\ a_2 &= -D \left[2\gamma_2^2 \left(2C_{000} + C_{220} \right) + 3\gamma_3 \right] \\ a_3 &= -2D \left[2\gamma_2^2 \left(C_{211} + C_{011} + C_{000} \right) + 3\gamma_3 \right] \\ a_4 &= -2D \left[2\gamma_2^2 \left(2C_{011} + C_{200} \right) + 3\gamma_3 \right] \\ a_5 &= -\frac{\gamma_c^2}{2} D \left(\frac{\partial}{\partial i k_1} - v_g \frac{\partial}{\partial i \omega} \right)^2 \left(\tilde{\eta} \widehat{K} \right) \\ D &= \frac{1}{\gamma_c^2} \left(\frac{\partial (\tilde{\eta} \widehat{K})}{\partial i \omega} \right)^{-1},\end{aligned} \tag{4.3.19}$$

with the shorthand notation

$$C_{lmn} = \frac{\tilde{\eta}(il\omega_c)\widehat{K}((mk_c, nk_c)^T, il\omega_c)}{1 - \gamma_c\tilde{\eta}(il\omega_c)\widehat{K}((mk_c, nk_c)^T, il\omega_c)}. \tag{4.3.20}$$

4.3.2 $D_4 \ltimes T^2$ Normal form

For small ϵ, in a first approximation one may assume that the amplitudes A_i do not vary with ξ_i leading to

$$\begin{aligned}
\frac{\mathrm{d}A_1}{\mathrm{d}\tau} &= a_0A_1 + A_1\left[a_1|A_2|^2 + a_2\left(|A_1|^2 + |A_2|^2\right) + a_3\left(|A_3|^2 + |A_4|^2\right)\right] + a_4\bar{A}_2A_3A_4\\
\frac{\mathrm{d}A_2}{\mathrm{d}\tau} &= a_0A_2 + A_2\left[a_1|A_1|^2 + a_2\left(|A_1|^2 + |A_2|^2\right) + a_3\left(|A_3|^2 + |A_4|^2\right)\right] + a_4\bar{A}_1A_3A_4\\
\frac{\mathrm{d}A_3}{\mathrm{d}\tau} &= a_0A_3 + A_3\left[a_1|A_4|^2 + a_2\left(|A_3|^2 + |A_4|^2\right) + a_3\left(|A_1|^2 + |A_2|^2\right)\right] + a_4\bar{A}_4A_1A_2\\
\frac{\mathrm{d}A_4}{\mathrm{d}\tau} &= a_0A_4 + A_4\left[a_1|A_3|^2 + a_2\left(|A_3|^2 + |A_4|^2\right) + a_3\left(|A_1|^2 + |A_2|^2\right)\right] + a_4\bar{A}_3A_1A_2.
\end{aligned} \tag{(3.3.3) revisited}$$

This is the normal form for the Hopf bifurcation on a square lattice that is determined and analyzed in Silber & Knobloch [7], and discussed in Section 3.3.2.

4.3.3 Locating degeneracies

This section explains how to use the normal form of Eq. (3.3.3) to reveal spatiotemporal solutions of Eq. (2.3.1) assuming the specific temporal dynamics and spatial interaction, Eqs. (2.3.5) and (4.1.5).

Parameter search

Despite having a complicated normal form parameter space, $\mathbb{C}^4$, we can make use of Silber & Knobloch's analysis to determine the branches of the periodic solutions for a given set of model parameters. We find the system parameters c, α, a_e, a_i, r, and $\gamma_1 = \gamma_c$ such that a dynamic Turing bifurcation emerges, then apply Eqs. (4.3.19) and compare the parameters found to the conditions in Table 3.1 to see how the solutions branch.

To compute the normal form parameters, we only need to have set the specific functions and parameters for the temporal and spatial kernels, η and K, respectively. Once these are set, varying the steepness of the transfer function f changes only γ_2 and γ_3, and we can observe how the branching diagram changes.

As an example, we set the system parameters as those depicted with the spectrum in Table 4.1, with the maximum of the sigmoid $S_{max} = 1$. We note that the maximum slope of the transfer function is $\gamma = C/4$. Thus, for a small steepness $C < 4\gamma_c$, we

C interval	Region number	Distinguishing characteristic
$(4\gamma_c, C_1)$	21(-)	TR and AR both supercritical and stable
(C_1, C_2)	24(-)	TR subcritical, AR supercritical and stable
(C_2, C_3)	23(-)	TR and AR both subcritical
(C_3, C_4)	25(-)	Only TS and SS supercritical
(C_4, C_5)	20(-)	Only SS supercritical
(C_5, ∞)	1(-)	All modes subcritical

Table 4.2: The regions of normal form parameter space traversed as steepness is increased. The visualization of this is in Figure 4.8.

Transition	Degeneracy condition	Solution
$21 \to 24$	$\mathrm{Re}\,(a_2) = 0$	$C_1 \approx 3.209199$
$24 \to 23$	$\mathrm{Re}\,(a_1 + 2a_2 - (f + \lvert a_4\rvert)/2) = 0$	$C_2 \approx 3.522248$
$23 \to 25$	$\mathrm{Re}\,(a_1 + 2a_2) = 0$	$C_3 \approx 3.525135$
$25 \to 20$	$\mathrm{Re}\,(a_1 + 4a_2 - f) = 0$	$C_4 \approx 4.214041$
$20 \to 1$	$\mathrm{Re}\,(a_1 + 2a_2 - (f - \lvert a_4\rvert)/2) = 0$	$C_5 \approx 16.069927$

Table 4.3: The transitions between branching diagrams, their associated degeneracy conditions, and the C values that satisfy this for the parameters in Table 4.1. Note that f used here is a combination of parameters defined in [7] for convenience $f = a_1 + 2a_2 - 2a_3$.

find that there will be no dynamic Turing bifurcation. For $C = 4\gamma_c$, there exists a single dynamic Turing bifurcation but it is degenerate in the sense that the spectrum never destabilizes, but just touches the complex axis. For $C > 4\gamma_c$, our analysis can be applied, and the behaviour as C is increased further is summarized in Table 4.2, and visualized in Figure 4.8.

Note that this analysis approach does not reveal what happens for explicit equalities $C = C_i$. This is because these represent degenerate cases in the normal form, and to understand what is happening we need to take into account nonlinear terms of larger than cubic orders. As there are a large number of ways in which these degeneracies arise, we refrain from analyzing all possibilities. Rather we investigate how to determine when a specific degeneracy emerges while varying C.

To compute the values of C_i of the degenerate cases, the problem can be formulated in terms of a Newton iteration to solve the nearby degeneracy condition. For instance, for C_1 we observe that $C \approx 4\gamma_c + 0.5$ is close to the degeneracy condition between regions 21 and 24. The equation for this degeneracy is simply given by

$$\mathrm{Re}\,(a_2) = 0,$$

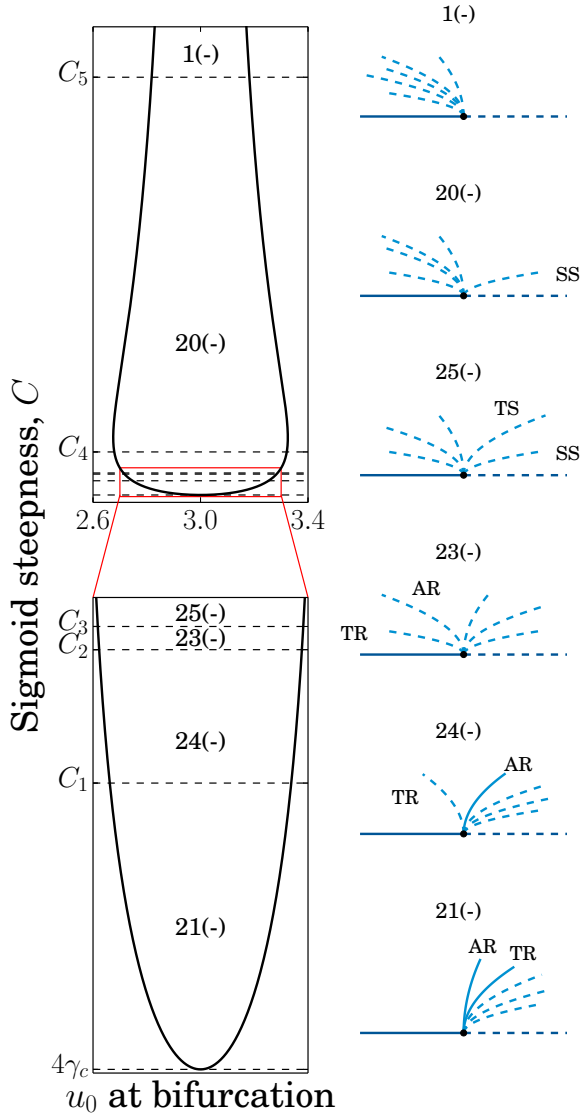

Figure 4.8: The behaviour of the dynamic Turing bifurcations for increasing steepness $C > 4\gamma_c$ for parameters taken from Table 4.1. *Left*: Relation between steepness parameter C and values of u_0 at the dynamic Turing bifurcations, the lower being a more detailed view of a region in the upper. *Right*: Branching diagram at the lower bifurcation point, noting that the branching diagram for the upper point is simply the mirror image. Definition and values of C_i are given in Table 4.2 and Table 4.3, respectively.

as determined in [7]. Taking the equation to be just a function of C, we can apply Newton's method to obtain the value of C_1 that satisfies this to arbitrary precision, limited only by the precision of the previously calculated γ_c, k_c, and ω_c. Increasing the parameter C, one crosses different degeneracy conditions. These conditions, along with the corresponding values of C_i where they are satisfied, are given in Table 4.3.

4.4 Simulation

To compare the analytical results to numerical solutions of Eq. (2.3.1), we have employed a recently developed numerical integration scheme[1] [5, 4]. The numerical scheme assumes a discretization in space and time, and considers a fixed finite transmission speed. To integrate over time, a forward Euler scheme is applied. The computation of the spatial integral in Eq. (2.3.1) is done as a combination of a spatial convolution and a temporal integration, where the former is implemented by a Fast Fourier transform and the latter utilizes a rectangular integration rule.

By virtue of the spatial discretization, it is mandatory to choose the spatial extension of the integration domain $|\Omega| = L^2$ with side length L and the number of discretization intervals N in such a way to ensure the convergence of the numerical solution to the analytical results. The major criteria for the parameters are:

- *Discretization of wave vectors*: the wave vector $\mathbf{k} = (k_x, k_y)^T$ is discrete due to periodic boundary condition, i.e. $k_i = n_i \Delta k$, $n_i \in \mathbb{Z}$ for $i = x, y$ and $\Delta k = 2\pi/L$. For a finite number N $n_i = -N/2, \ldots, N/2$. Hence the maximum resolution for wave vectors is given by $\Delta k = 2\pi/N\Delta x$ where $\Delta x = L/N$, and $k = \|\mathbf{k}\|$ is a multiple of Δk. This insight is important when scanning the parameter space for values of k which destabilize the stationary state. In addition, Δk has to be chosen in such a way that it allows to sample the Fourier transforms with a sufficiently high resolution, e.g. resolving the locations of local extrema of the transforms.
- *Discretization of space*: the analytical study assumes periodically repeating solutions on an infinite spatial domain implying that there are no boundary effects affecting the Fourier transform of the spatial connectivity kernel while, on the other side, taking into account periodic boundary conditions. To ensure the validity of these assumptions, we have guaranteed by a large enough L and N that the analytical and spatial norms of the connection kernels are identical up to a relative error < 0.01.
- *Numerical integration time*: The larger N, the better the numerical approximation of the analytical dynamics. However, the number of delayed rings to be integrated in the delay integral increases with the spatial discretization N. To see this, we note that there is a maximum transmission delay $\tau_m = \frac{L}{2c}$ due to the finiteness of location space. Since the numerical integration makes it necessary to discretize the delay integral into time steps $\Delta t = \tau_m/T_m$, the numerical

[1] NeuralFieldSimulator: https://gforge.inria.fr/projects/nfsimulator/

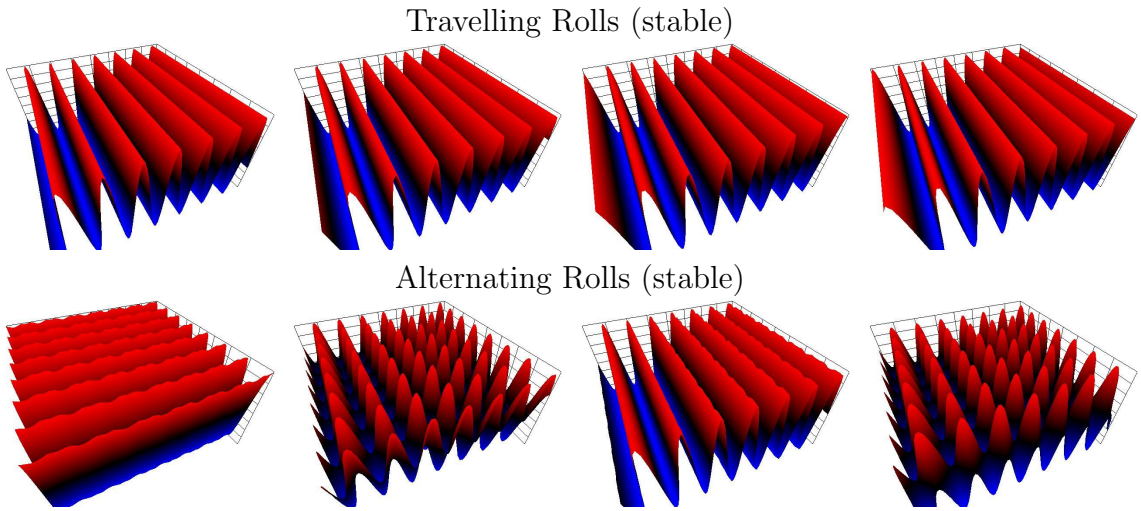

Figure 4.9: Snapshots of stable TR and AR from NeuralFieldSimulator [6]: direct numerical simulation of the integral model Eq. (2.3.1) just beyond the discussed bifurcation point. Steepness parameter set to $C = 2.856$, which corresponds to region 21(-) in Figure 4.8. Time in the frames is increasing by one-eighth of the critical period $T_c \approx 1.84783$. Simulation domain size is $L = 7L_c \approx 40.3805$, discretized into $N = 512$ points in each dimension.

integration performs a sum over rings of number

$$T_m = \frac{\Delta x}{2c\Delta t} N, \tag{4.4.1}$$

i.e. the number of terms to sum up in the integral is proportional to the number of discretization intervals N.

The relation (4.4.1) leads to a trade-off between the integration time and the integration precision.

With the above considered, we are able to simulate the predicted stable modes of region 21(−) (TR and AR) from Fig. 4.8. For our parameter set, we find that a simulation domain of length $L = 7l_c$, with a discretization of $N = 512$ points in each spatial dimension is enough for the norm of the discretized kernel connectivity to match the norm of the analytical connectivity within a tolerance of 0.01.

Simulating a desired mode requires us to use initial conditions (initial history, technically) that are within the basin of attraction for that mode. We know no details of the geometry of these basins, and simulating from random initial conditions is not likely to produce one of the principal modes. However, starting the simulation from conditions that are the correct shape (but wrong amplitude) of the desired mode should allow it to evolve towards the mode. This is what was done to generate the fields in Figure 4.9, which are taken after the transient variation in amplitude has decayed.

When we do start with random perturbations in the initial conditions, the simulation becomes more unpredictable. For example, if we set initial conditions that

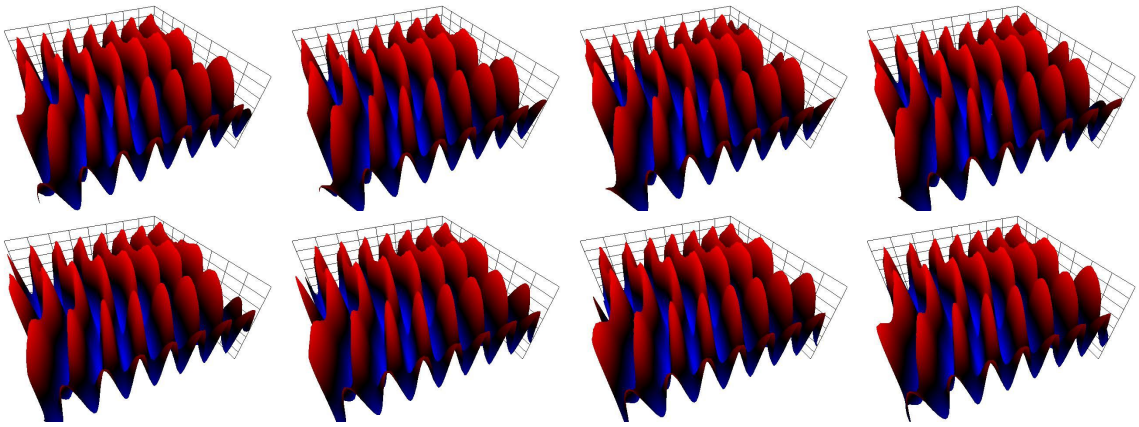

Figure 4.10: When noisy initial conditions are used in simulation, i.e., the initial field is not periodic on $(0, L_c)^2$, simulations progress in an unpredictable manner. However, it is usually possible to visually pick out regions that resemble the elementary modes from the $D_4 \ltimes T^2$ symmetric restriction, e.g., TR with different directions, local AR, etc. Left to right, top to bottom, the time of the frames is again progressing by one-eighth of the critical period.

are in the shape of a standing square wave, and add to this Gaussian white noise across the domain, then after some time, the numerical solution may or may not have regions that resemble the elementary modes discussed in our analysis. This comes about because our analysis was performed for a *single unit cell* near the bifurcation point, i.e., length $L = L_c$, but our numerics are restricted to being on a domain at least seven times this size. Stability that we speak of thus refers to stability with respect to perturbations with the periodicity of the unit cell. After a long simulation time, this example of randomized initial conditions is shown in Figure 4.10. For our parameters, the simulation is eventually dominated by TR-like behaviour, which is good because our analysis showed these to be stable, but there are deviations from the elementary TR solution in the waves' profile.

Bibliography

[1] Folias, S. E. Nonlinear Analysis of Breathing Pulses in a Synaptically Coupled Neural Network. *SIAM Journal on Applied Dynamical Systems 10*, 2 (2011), 744–787.

[2] Helmberg, G. *Introduction to spectral theory in hilbert space.* North Holland Publishing Company, Amsterdam, 1969.

[3] Hutt, A., Bestehorn, M., and Wennekers, T. Pattern formation in intracortical neuronal fields. *Network Computation in Neural Systems 14*, 2 (2003), 351–68.

[4] Hutt, A., and Rougier, N. Activity spread and breathers induced by finite transmission speeds in two-dimensional neural fields. *Physical Review E 82*, 5 (2010), 055701.

[5] Hutt, A., and Rougier, N. Numerical simulation scheme of one- and two-dimensional neural fields involving space-dependent delays. In *Neural Field Theory*, S. Coombes, P. beim Graben, R. Potthast, and J. J. Wright, Eds. Springer, 2014, pp. 175–183.

[6] Nichols, E. J., and Hutt, A. Neural field simulator: fast computation and 3D-visualization. *BMC Neuroscience 14(1)* (2013).

[7] Silber, M., and Knobloch, E. Hopf bifurcation on a square lattice. *Nonlinearity 4*, 4 (1991), 1063–1107.

[8] Veltz, R., and Faugeras, O. A center manifold result for delayed neural fields equations. *SIAM Journal on Mathematical Analysis 45*, 3 (2013), 1527–1562.

[9] Venkov, N., Coombes, S., and Matthews, P. Dynamic instabilities in scalar neural field equations with space-dependent delays. *Physica D 232*, 1 (2007), 1–15.

Chapter 5

Analysis of Liley's model

5.1 Preliminaries 84
5.1.1 Linearization and dispersion 86
5.1.2 $D_4 \ltimes T^2$ symmetric Hopf 87
5.1.3 Simulation 90
5.1.4 Periodic orbit computations 93
5.1.5 Initialization of $D_4 \ltimes T^2$ modes 94
5.2 Parameter set I 95
5.2.1 Origin 95
5.2.2 Building on previous work 98
5.3 Parameter set II 105
5.3.1 Origin 105
5.3.2 Building on previous work 105
Bibliography 110

This chapter will bring the view of dynamical systems from Chapter 3 to Liley's neural field model which was described in Chapter 2. For this model, we must recall both the integral form,

$$
\begin{aligned}
h_k(\mathbf{x},t) &= \eta_k * \left(h_k^r + \sum_j \frac{h_{jk}^{eq} - h_k(\mathbf{x},t)}{\left|h_{jk}^{eq} - h_k^r\right|} I_{jk}(\mathbf{x},t) \right), \\
I_{jk}(\mathbf{x},t) &= \eta_{jk} * \left(K_{jk} \otimes S_j \circ h_j(\mathbf{x},t) + p_{jk} \right),
\end{aligned}
\qquad \text{((2.4.1) revisited)}
$$

which is used for the weakly nonlinear analysis, and the specific PDE form

$$\begin{aligned}
\tau_k \frac{\partial}{\partial t} h_k(\mathbf{x},t) &= h_k^r - h_k(\mathbf{x},t) + \sum_j \frac{h_{jk}^{eq} - h_k(\mathbf{x},t)}{\left|h_{jk}^{eq} - h_k^r\right|} I_{jk}(\mathbf{x},t) \\
\left(\frac{\partial}{\partial t} + \gamma_{jk}\right)^2 I_{jk}(\mathbf{x},t) &= \exp(1)\Gamma_{jk}\gamma_{jk}\left[N_{jk}^{\beta} S_j \circ h_j(\mathbf{x},t) + \phi_{jk}(\mathbf{x},t) + p_{jk}\right] \\
\left[\left(\frac{\partial}{\partial t} + v\Lambda\right)^2 - \frac{3}{2}v^2\nabla^2\right]\phi_{ek}(\mathbf{x},t) &= N_{ek}^{\alpha} v^2 \Lambda^2 S_e \circ h_e(\mathbf{x},t) \\
\phi_{ik}(\mathbf{x},t) &= 0,
\end{aligned}$$

((2.4.6) revisited)

which is used for numerical simulation.

This chapter focuses on applying the weakly nonlinear analysis of the $D_4 \ltimes T^2$ symmetric Hopf bifurcation to a system of integral equations, followed by the development of simulation code for the PDE variant Liley's model. We then apply the developed ideas and methods to two specific parameter sets chosen from literature to evaluate them and gain some further insight.

5.1 Preliminaries

The first thing we will do is write the different forms of Liley's model as vector systems, expanding the dense index notation. First is the general form with the integral convolutions. This does not require any manipulations, we simply write the 6 components of the model out in vector form

$$\begin{bmatrix} h_e \\ h_i \\ I_{ee} \\ I_{ie} \\ I_{ei} \\ I_{ii} \end{bmatrix} = \begin{bmatrix} \eta_e * \left(h_e^r + \frac{h_{ee}^{eq} - h_e(\mathbf{x},t)}{\left|h_{ee}^{eq} - h_e^r\right|} I_{ee}(\mathbf{x},t) + \frac{h_{ie}^{eq} - h_e(\mathbf{x},t)}{\left|h_{ie}^{eq} - h_e^r\right|} I_{ie}(\mathbf{x},t)\right) \\ \eta_i * \left(h_i^r + \frac{h_{ei}^{eq} - h_i(\mathbf{x},t)}{\left|h_{ei}^{eq} - h_i^r\right|} I_{ei}(\mathbf{x},t) + \frac{h_{ii}^{eq} - h_i(\mathbf{x},t)}{\left|h_{ii}^{eq} - h_i^r\right|} I_{ii}(\mathbf{x},t)\right) \\ \eta_{ee} * \left(K_{ee} \otimes S_e \circ h_e(\mathbf{x},t) + p_{ee}\right) \\ \eta_{ie} * \left(K_{ie} \otimes S_i \circ h_i(\mathbf{x},t) + p_{ie}\right) \\ \eta_{ei} * \left(K_{ei} \otimes S_e \circ h_e(\mathbf{x},t) + p_{ei}\right) \\ \eta_{ii} * \left(K_{ii} \otimes S_i \circ h_i(\mathbf{x},t) + p_{ii}\right) \end{bmatrix}. \tag{5.1.1}$$

We will consistently use small letters to denote vectors of this general integral system, i.e., $u(\mathbf{x},t) = (h_e, h_i, I_{ee}, I_{ie}, I_{ei}, I_{ii})^T(\mathbf{x},t)$ for this chapter.

For a vector system from the specific PDE formulation, we introduce additional variables to split the postsynaptic potentials and long range connections from their second order form in a common way. For postsynaptic potentials, we introduce the

J_{jk} fields,

$$\begin{aligned}\frac{\partial}{\partial t}I_{jk} &= J_{jk} - \gamma_{jk}I_{jk} \\ \frac{\partial}{\partial t}J_{jk} &= \exp(1)\Gamma_{jk}\gamma_{jk}\left\{N_{jk}^{\beta}S_j\left[h_j\right] + \phi_{jk} + p_{jk}\right\} - \gamma_{jk}J_{jk}\end{aligned} \tag{5.1.2}$$

and for the long-range connections, the ψ_{ek} fields,

$$\begin{aligned}\frac{\partial}{\partial t}\phi_{ek} &= \psi_{ek} - v\Lambda\phi_{ek} \\ \frac{\partial}{\partial t}\psi_{ek} &= v^2\Lambda^2 N_{ek}^{\alpha}S_e\left[h_e\right] + \frac{3}{2}v^2\nabla^2\phi_{ek} - v\Lambda\psi_{ek}.\end{aligned} \tag{5.1.3}$$

This allows the PDE system for Liley's model to be written as

$$\frac{\partial}{\partial t}\begin{bmatrix} h_e(\mathbf{x},t) \\ h_i(\mathbf{x},t) \\ I_{ee}(\mathbf{x},t) \\ J_{ee}(\mathbf{x},t) \\ I_{ie}(\mathbf{x},t) \\ J_{ie}(\mathbf{x},t) \\ I_{ei}(\mathbf{x},t) \\ J_{ei}(\mathbf{x},t) \\ I_{ii}(\mathbf{x},t) \\ J_{ii}(\mathbf{x},t) \\ \phi_{ee}(\mathbf{x},t) \\ \psi_{ee}(\mathbf{x},t) \\ \phi_{ei}(\mathbf{x},t) \\ \psi_{ei}(\mathbf{x},t) \end{bmatrix} = \begin{bmatrix} \frac{1}{\tau_e}\left(h_e^r - h_e(\mathbf{x},t) + \frac{h_{ee}^{eq}-h_e(\mathbf{x},t)}{\left|h_{ee}^{eq}-h_e^r\right|}I_{ee}(\mathbf{x},t) + \frac{h_{ie}^{eq}-h_e(\mathbf{x},t)}{\left|h_{ie}^{eq}-h_e^r\right|}I_{ie}(\mathbf{x},t)\right) \\ \frac{1}{\tau_i}\left(h_i^r - h_i(\mathbf{x},t) + \frac{h_{ei}^{eq}-h_e(\mathbf{x},t)}{\left|h_{ei}^{eq}-h_i^r\right|}I_{ei}(\mathbf{x},t) + \frac{h_{ii}^{eq}-h_i(\mathbf{x},t)}{\left|h_{ii}^{eq}-h_i^r\right|}I_{ii}(\mathbf{x},t)\right) \\ J_{ee}(\mathbf{x},t) - \gamma_{ee}I_{ee}(\mathbf{x},t) \\ \exp(1)\Gamma_{ee}\gamma_{ee}\left(N_{ee}^{\beta}S_e\left[h_e(\mathbf{x},t)\right] + \phi_{ee}(\mathbf{x},t) + p_{ee}\right) - \gamma_{ee}J_{ee}(\mathbf{x},t) \\ J_{ie}(\mathbf{x},t) - \gamma_{ie}I_{ie}(\mathbf{x},t) \\ \exp(1)\Gamma_{ie}\gamma_{ie}\left(N_{ie}^{\beta}S_i\left[h_i(\mathbf{x},t)\right] + \phi_{ie}(\mathbf{x},t) + p_{ie}\right) - \gamma_{ie}J_{ie}(\mathbf{x},t) \\ J_{ei}(\mathbf{x},t) - \gamma_{ei}I_{ei}(\mathbf{x},t) \\ \exp(1)\Gamma_{ei}\gamma_{ei}\left(N_{ei}^{\beta}S_e\left[h_e(\mathbf{x},t)\right] + \phi_{ei}(\mathbf{x},t) + p_{ei}\right) - \gamma_{ei}J_{ei}(\mathbf{x},t) \\ J_{ii}(\mathbf{x},t) - \gamma_{ii}I_{ii}(\mathbf{x},t) \\ \exp(1)\Gamma_{ii}\gamma_{ii}\left(N_{ii}^{\beta}S_i\left[h_i(\mathbf{x},t)\right] + \phi_{ii}(\mathbf{x},t) + p_{ii}\right) - \gamma_{ii}J_{ii}(\mathbf{x},t) \\ \psi_{ee}(\mathbf{x},t) - v\Lambda\phi_{ee}(\mathbf{x},t) \\ v^2\Lambda^2 N_{ee}^{\alpha}S_e\left[h_e(\mathbf{x},t)\right] + \frac{3}{2}v^2\nabla^2\phi_{ee}(\mathbf{x},t) - v\Lambda\psi_{ee}(\mathbf{x},t) \\ \psi_{ei}(\mathbf{x},t) - v\Lambda\phi_{ei}(\mathbf{x},t) \\ v^2\Lambda^2 N_{ei}^{\alpha}S_e\left[h_e(\mathbf{x},t)\right] + \frac{3}{2}v^2\nabla^2\phi_{ei}(\mathbf{x},t) - v\Lambda\psi_{ei}(\mathbf{x},t) \end{bmatrix} \tag{5.1.4}$$

which fits the first order (in time) general form for an infinite dimensional dynamical system. We will consistently denote the vectors for this system as upper case letters, i.e., $U(\mathbf{x},t) = (h_e, h_i, I_{ee}, J_{ee}, I_{ie}, J_{ie}, I_{ei}, J_{ei}, I_{ii}, J_{ii}, \phi_{ee}, \psi_{ee}, \phi_{ei}, \psi_{ei})^T(\mathbf{x},t)$.

It is because of the large expression for the PDE system that the weakly nonlinear analysis is done on the simpler 6 component integral system of Eq. (5.1.1). In addition to this, there is an added bonus: such analysis can be used with general connectivities.

5.1.1 Linearization and dispersion

Assuming we have some solution u^0 to Liley's model, we can write the linearization of the integral form as

$$\mathcal{L}u^1(\mathbf{x},t) = \begin{bmatrix} \mathcal{L}_{11} & 0 & \mathcal{L}_{13} & \mathcal{L}_{14} & 0 & 0 \\ 0 & \mathcal{L}_{22} & 0 & 0 & \mathcal{L}_{25} & \mathcal{L}_{26} \\ \mathcal{L}_{31} & 0 & 1 & 0 & 0 & 0 \\ 0 & \mathcal{L}_{42} & 0 & 1 & 0 & 0 \\ \mathcal{L}_{51} & 0 & 0 & 0 & 1 & 0 \\ 0 & \mathcal{L}_{62} & 0 & 0 & 0 & 1 \end{bmatrix} u^1(\mathbf{x},t) = 0 \tag{5.1.5}$$

with the components

$$\begin{aligned}
\mathcal{L}_{11} &= 1 + \frac{1}{|h_{ee}^{eq} - h_e^r|}\eta_e * \left(I_{ee}^0(\mathbf{x},t)\,\cdot\right) + \frac{1}{|h_{ie}^{eq} - h_e^r|}\eta_e * \left(I_{ie}^0(\mathbf{x},t)\,\cdot\right) \\
\mathcal{L}_{13} &= \frac{1}{|h_{ee}^{eq} - h_e^r|}\eta_e * \left(h_e^0(\mathbf{x},t)\,\cdot\right) \\
\mathcal{L}_{14} &= \frac{1}{|h_{ie}^{eq} - h_e^r|}\eta_e * \left(h_e^0(\mathbf{x},t)\,\cdot\right) \\
\mathcal{L}_{22} &= 1 + \frac{1}{|h_{ei}^{eq} - h_i^r|}\eta_i * \left(I_{ei}^0(\mathbf{x},t)\,\cdot\right) + \frac{1}{|h_{ii}^{eq} - h_i^r|}\eta_i * \left(I_{ii}^0(\mathbf{x},t)\,\cdot\right) \\
\mathcal{L}_{25} &= \frac{1}{|h_{ei}^{eq} - h_i^r|}\eta_i * \left(h_i^0(\mathbf{x},t)\,\cdot\right) \\
\mathcal{L}_{26} &= \frac{1}{|h_{ii}^{eq} - h_i^r|}\eta_i * \left(h_i^0(\mathbf{x},t)\,\cdot\right) \\
\mathcal{L}_{31} &= -\eta_{ee} * \left(K_{ee} \otimes S_e'[h_e^0(\mathbf{x},t)]\,\cdot\right) \\
\mathcal{L}_{42} &= -\eta_{ie} * \left(K_{ie} \otimes S_i'[h_i^0(\mathbf{x},t)]\,\cdot\right) \\
\mathcal{L}_{51} &= -\eta_{ei} * \left(K_{ei} \otimes S_e'[h_e^0(\mathbf{x},t)]\,\cdot\right) \\
\mathcal{L}_{62} &= -\eta_{ii} * \left(K_{ii} \otimes S_i'[h_i^0(\mathbf{x},t)]\,\cdot\right).
\end{aligned} \tag{5.1.6}$$

For SHE, this simplifies in a similar way to the scalar equation: All of the zeroth order terms can be taken out of the integral operators, so the operators will act only on the higher order solutions to which this is applied. Now we look at perturbations of the form $u^1 = qe^{i\mathbf{k}\cdot\mathbf{x}}e^{\lambda t}$. This allows us to write the linear system in Fourier-Laplace space

$$L(\mathbf{k},\lambda)q = \begin{bmatrix} 1 + \left(\frac{I_{ee}^0}{|h_{ee}^{eq} - h_e^r|} + \frac{I^0{}_{ie}}{|h_{ie}^{eq} - h_e^r|}\right)\tilde{\eta}_e & 0 & \frac{h_e^0}{|h_{ee}^{eq} - h_e^r|}\tilde{\eta}_e & \frac{h_e^0}{|h_{ie}^{eq} - h_e^r|}\tilde{\eta}_e & 0 & 0 \\ 0 & 1 + \left(\frac{I_{ei}^0}{|h_{ei}^{eq} - h_i^r|} + \frac{I_{ii}^0}{|h_{ii}^{eq} - h_i^r|}\right)\tilde{\eta}_i & 0 & 0 & \frac{h_i^0}{|h_{ei}^{eq} - h_i^r|}\tilde{\eta}_i & \frac{h_i^0}{|h_{ii}^{eq} - h_i^r|}\tilde{\eta}_i \\ -\gamma_e^1\tilde{\eta}_e\widehat{K}_{ee} & 0 & 1 & 0 & 0 & 0 \\ 0 & -\gamma_i^1\tilde{\eta}_i\widehat{K}_{ie} & 0 & 0 & 1 & 0 \\ -\gamma_e^1\tilde{\eta}_e\widehat{K}_{ei} & 0 & 0 & 1 & 0 & 0 \\ 0 & -\gamma_i^1\tilde{\eta}_i\widehat{K}_{ii} & 0 & 0 & 0 & 1 \end{bmatrix} q = 0, \tag{5.1.7}$$

where the arguments in $\tilde{\eta}(\lambda)$ and $\widehat{K}(\mathbf{k},\lambda)$ are always the same, and we have introduced the short notation

$$\gamma_e^1 = S_e'(h_e^0), \quad \gamma_i^1 = S_i'(h_i^0) \tag{5.1.8}$$

The dispersion relation will then satisfy $\det L(\mathbf{k},\lambda) = 0$.

5.1.2 $D_4 \ltimes T^2$ symmetric Hopf

The normal form coefficients for Liley's model can also be computed using a multi-scale analysis as was done for the scalar field. For this, however, we do not consider the long spatial scale in order to simplify the calculations, and can obtain the normal form of Eq. (3.3.3) directly. The weakly nonlinear analysis now proceeds with the integral equation system Eq. (5.1.1).

The modes causing a $D_4 \ltimes T^2$ Hopf bifurcation for a system of equations can be written as

$$\varphi_1 = q\phi_1, \quad \varphi_2 = q\phi_2, \quad \varphi_3 = q\phi_3, \quad \varphi_4 = q\phi_4, \tag{5.1.9}$$

where ϕ_j represent the $D_4 \ltimes T^2$ scalar wave modes given in Eq. (3.3.2), and q represents the normalized right nullvector of the Fourier-Laplace transformed linear system at criticality

$$L\left(\mathbf{k}_c, i\omega_c\right) q = 0, \quad \bar{q}^T q = 1, \tag{5.1.10}$$

The first order solution is then written as

$$\begin{aligned} u^1(\mathbf{x},t) &= \sum_{j=1}^{4} \left(A_j\varphi_j + \bar{A}_j\bar{\varphi}_j\right) \\ &= q\sum_{j=1}^{4} A_j\phi_j + \bar{q}\sum_{j=1}^{4} \bar{A}_j\bar{\phi}_j. \end{aligned} \tag{5.1.11}$$

For this, we consider the amplitudes to be only functions of the long time scale $\tau = \epsilon^2 t$, excluding the long spatial scale $\boldsymbol{\chi}$ and the intermediate time scale θ. Determining the higher order perturbations will result in the sequence of equations

$$\begin{aligned} \mathcal{L}u^1(\mathbf{x},t) &= g^1(u^0) = 0 \\ \mathcal{L}u^2(\mathbf{x},t) &= g^2(u^0,u^1) \\ \mathcal{L}u^3(\mathbf{x},t) &= g^3(u^0,u^1,u^2), \end{aligned} \tag{5.1.12}$$

with each order requiring the solution to a 6 component linear system. Fortunately, all of the hard work in separating the scales of the integral terms was performed in the scalar model, and Liley's model can be expressed in terms of those results. The

second order equation will have

$$g^2 = \begin{bmatrix} -\eta_e * \left(\frac{h_e^1 I_{ee}^1}{|h_{ee}^{eq} - h_e^r|} + \frac{h_e^1 I_{ie}^1}{|h_{ie}^{eq} - h_e^r|} \right) \\ -\eta_i * \left(\frac{h_i^1 I_{ei}^1}{|h_{ei}^{eq} - h_i^r|} + \frac{h_i^1 I_{ii}^1}{|h_{ii}^{eq} - h_i^r|} \right) \\ \gamma_e^2 M_{ee}^0 (h_e^1)^2 + \gamma_e^1 M_{ee}^1 h_e^1 \\ \gamma_i^2 M_{ie}^0 (h_i^1)^2 + \gamma_i^1 M_{ie}^1 h_i^1 \\ \gamma_e^2 M_{ei}^0 (h_e^1)^2 + \gamma_e^1 M_{ei}^1 h_e^1 \\ \gamma_i^2 M_{ii}^0 (h_i^1)^2 + \gamma_i^1 M_{ii}^1 h_i^1 \end{bmatrix}, \tag{5.1.13}$$

where we have introduced the notation $\gamma_j^2 = S_k''(h_k^0)/2$, and the M_{jk}^n operators are simply the M_n operators from the scalar analysis (Eq. (4.3.9)) with indices added for the generating and receiving populations, i.e.,

$$\begin{aligned} M_{jk}^0 &= \eta_{jk} * K_{jk} \otimes, \\ M_{jk}^1 &= 0, \\ M_{jk}^2 &= (t\eta_{jk} * K_{jk} + \eta_{jk} * tK_{jk}) \otimes \frac{\partial}{\partial \tau}, \end{aligned} \tag{5.1.14}$$

noting the drastic simplification that comes with ignoring the long space and intermediate time scales at this stage. The M_{jk}^2 operator shows up in the next order equation.

The right hand side for the third order equation is

$$g^3 = \begin{bmatrix} -\eta_e * \left[\left(\frac{I_{ee}^2}{|h_{ee}^{eq} - h_e^r|} + \frac{I_{ie}^2}{|h_{ie}^{eq} - h_e^r|} \right) h_e^1 + \left(\frac{I_{ee}^1}{|h_{ee}^{eq} - h_e^r|} + \frac{I_{ie}^1}{|h_{ie}^{eq} - h_e^r|} \right) h_e^2 \right] \\ -\eta_i * \left[\left(\frac{I_{ei}^2}{|h_{ei}^{eq} - h_i^r|} + \frac{I_{ii}^2}{|h_{ii}^{eq} - h_i^r|} \right) h_i^1 + \left(\frac{I_{ei}^1}{|h_{ei}^{eq} - h_i^r|} + \frac{I_{ii}^1}{|h_{ii}^{eq} - h_i^r|} \right) h_i^2 \right] \\ M_{ee}^0 \left(2\gamma_e^2 h_e^1 h_e^2 + \gamma_e^3 (h_e^1)^3\right) + \gamma_e^1 M_{ee}^2 h_e^1 \\ M_{ie}^0 \left(2\gamma_i^2 h_i^1 h_i^2 + \gamma_i^3 (h_i^1)^3\right) + \gamma_i^1 M_{ie}^2 h_i^1 \\ M_{ei}^0 \left(2\gamma_e^2 h_e^1 h_e^2 + \gamma_e^3 (h_e^1)^3\right) + \gamma_e^1 M_{ei}^2 h_e^1 \\ M_{ii}^0 \left(2\gamma_i^2 h_i^1 h_i^2 + \gamma_i^3 (h_i^1)^3\right) + \gamma_i^1 M_{ii}^2 h_i^1 \end{bmatrix}, \tag{5.1.15}$$

with $\gamma_j^3 = S'''(h_j^0)/6$. To help parse the meaning, it is useful to keep in mind that superscripts on variables are denoting a perturbation order, and that powers have been written with explicit brackets consistently.

Also to note with Liley's model, we have not included a parameter that involves distance from the bifurcation (i.e., δ in the scalar analysis), and this is because we are interested in computing the normal form coefficients $a_{1,2,3,4}$ that determine the criticality and stability of the branching solutions. This can be thought of as looking at the parameter independent normal form. Criticality and stability can be obtained by analysis at the bifurcation point, similar to setting $\delta = 0$ in the scalar model. An unfolding parameter β can then be added in afterwards with the assumption $\beta \propto p - p^c$, where p is an arbitrary parameter in Liley's model, and p^c its value at criticality.

Since $u^1 \in \ker \mathcal{L}$, the Fredholm Alternative must be satisfied for each order as

well. To apply the Fredholm alternative, we must define an inner product

$$\langle u, v\rangle = \frac{k_c^2\omega_c}{8\pi^3}\sum_j \int_\Lambda \mathrm{d}x_1\mathrm{d}x_2\mathrm{d}t\, \bar{u}_j(\mathbf{x},t)v_j(\mathbf{x},t) = \frac{k_c^2\omega_c}{8\pi^3}\int_\Lambda \mathrm{d}x_1\mathrm{d}x_2\mathrm{d}t\, \bar{u}^T(\mathbf{x},t)v(\mathbf{x},t), \tag{5.1.16}$$

with $\Lambda = [0, 2\pi/k_c]^2 \times [0, 2\pi/\omega_c]$ as in the scalar case. From Eq. (5.1.16), we can determine the adjoint operator $\mathcal{L}^*$. The adjoint turns out to be simply the transpose of the original operator with connectivity kernels evaluated at negative time

$$\mathcal{L}^* = \begin{bmatrix} \mathcal{L}^*_{11} & 0 & \mathcal{L}^*_{13} & \mathcal{L}^*_{14} & 0 & 0 \\ 0 & \mathcal{L}^*_{22} & 0 & 0 & \mathcal{L}^*_{25} & \mathcal{L}^*_{26} \\ \mathcal{L}^*_{31} & 0 & 1 & 0 & 0 & 0 \\ 0 & \mathcal{L}^*_{42} & 0 & 1 & 0 & 0 \\ \mathcal{L}^*_{51} & 0 & 0 & 0 & 1 & 0 \\ 0 & \mathcal{L}^*_{62} & 0 & 0 & 0 & 1 \end{bmatrix}^T \tag{5.1.17}$$

with the components

$$\begin{aligned}
\mathcal{L}^*_{11} &= 1 + \left(\frac{I^0_{ee}}{|h^{eq}_{ee} - h^r_e|} + \frac{I^0_{ie}}{|h^{eq}_{ie} - h^r_e|}\right)\eta_e(-t)* \\
\mathcal{L}^*_{13} &= \frac{h^0_e}{|h^{eq}_{ee} - h^r_e|}\eta_e(-t)* \\
\mathcal{L}^*_{14} &= \frac{h^0_e}{|h^{eq}_{ie} - h^r_e|}\eta_e(-t)* \\
\mathcal{L}^*_{22} &= 1 + \left(\frac{I^0_{ei}}{|h^{eq}_{ei} - h^r_i|} + \frac{I^0_{ii}}{|h^{eq}_{ii} - h^r_i|}\right)\eta_i(-t)* \\
\mathcal{L}^*_{25} &= \frac{h^0_i}{|h^{eq}_{ei} - h^r_i|}\eta_i(-t)* \\
\mathcal{L}^*_{26} &= \frac{h^0_i}{|h^{eq}_{ii} - h^r_i|}\eta_i(-t)* \\
\mathcal{L}^*_{31} &= -\gamma^1_e\eta_{ee}(-t) * K_{ee}(\mathbf{x}, -t)\otimes \\
\mathcal{L}^*_{42} &= -\gamma^1_i\eta_{ie}(-t) * K_{ie}(\mathbf{x}, -t)\otimes \\
\mathcal{L}^*_{51} &= -\gamma^1_e\eta_{ei}(-t) * K_{ei}(\mathbf{x}, -t)\otimes \\
\mathcal{L}^*_{62} &= -\gamma^1_i\eta_{ii}(-t) * K_{ii}(\mathbf{x}, -t)\otimes
\end{aligned} \tag{5.1.18}$$

This has the useful property that in Fourier-Laplace space, it is simply the conjugate transpose of the matrix L defined in Eq. (5.1.7). We define p as the nullvector of the Fourier-Laplace transform of this adjoint operator, which can thus be written as

$$\bar{L}^T(\mathbf{k}_c, i\omega_c)p = 0. \tag{5.1.19}$$

The Fredholm Alternative then manifests itself as requiring

$$\langle p\phi_j, g^n \rangle = 0 \tag{5.1.20}$$

for each of the nullspace elements ($j = 1 \ldots 4$), for each order of equation ($n = 1, 2, \ldots$).

As mentioned before, this is exactly the same procedure as was performed for the scalar model, now complicated by dealing with 6 simultaneous equations rather than 1. This can only be carried out numerically, so specific application of this method is deferred to Appendix B.1 with results simply stated in Sections 5.2, 5.3.

5.1.3 Simulation

An important tool for the analysis of complicated models is the ability to perform direct numerical simulation of the model equations. In fact, a large portion of time was spent in this thesis developing simulation tools using state-of-the-art algorithms for the PDE version of Liley's model. This section will describe the basic algorithms used in creating a scalable simulation code for numerical simulation of Eq. (2.4.6). Details of how the code is structured to incorporate everything discussed here is left to Appendix B.3.

Spatial discretization

Approximating the spatial derivatives by finite difference (FD) approximations will allow the continuous system to be discretized into an arbitrarily large finite dimensional system. We take a regular square grid with equally spaced nodes

$$\mathbf{x}_{j,k} = \begin{bmatrix} jh \\ kh \end{bmatrix},$$

with h the grid spacing. Taking centered differences in both spatial dimensions allows the Laplacian to be approximated as the truncation of

$$\nabla^2\phi(\mathbf{x}_{j,k}, t) = \frac{\phi(\mathbf{x}_{j-1,k},t)+\phi(\mathbf{x}_{j+1,k},t)+\phi(\mathbf{x}_{j,k-1},t)+\phi(\mathbf{x}_{j,k+1},t)-4\phi(\mathbf{x}_{j,k},t)}{h^2} + \mathcal{O}(h^2). \tag{5.1.21}$$

On a square grid with periodic boundary conditions in either direction, we order the nodes as

$$X = (\mathbf{x}_{0,0}, \ldots, \mathbf{x}_{0,N-1}, \mathbf{x}_{1,2}, \ldots, \mathbf{x}_{1,N-1}, \ldots)^T \tag{5.1.22}$$

The resulting node connectivity matrix will then appear as the light colouring in Figure 5.1.

Considering all 14 of the dynamical quantities at each node, we choose a grid-based ordering scheme, which allows us to hold our view of the large-scale coupling, but we can also consider the smaller scale coupling determined by the actual model Eq. (5.1.4). This gives us an overall view of the coupling in the discretized system, the

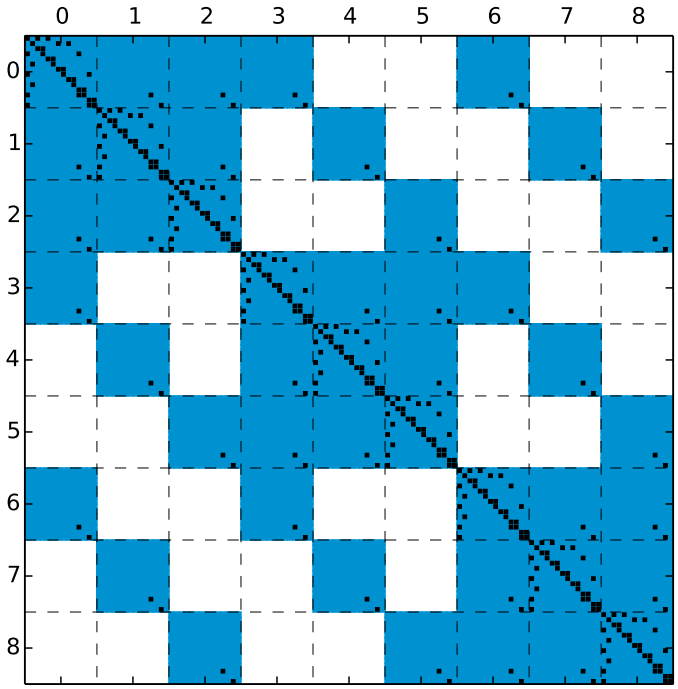

Figure 5.1: Coupling for Liley's model on a 3x3 grid with periodic BC. Grid-based ordering of the 14 components in Liley's PDE (dark) overlaid on the grid coupling (light). The result is a very sparse structure of the Jacobian.

black squares in Figure 5.1, which will reflect the structure of the Jacobian. Though visualized for only a 3x3 grid, the sparsity of this system is apparent, and is exploited for parallel computation for larger grids.

Distribution through parallel domain decomposition

As we take more and more grid points, computation on the discretized system will take longer and longer. Splitting up the domain into various pieces that can be worked on separately by different processors will become advantageous. The catch is that since our grid points do have a local coupling to their neighbours, it is required that points on the boundaries of processor subdomains be communicated to the relevant neighbouring processors that use them in computing the vector field or Jacobian. These coordinates whose actual values are on another processor are called *ghost nodes*, and this situation is visualized as the coloured squares in the discrete grid of Figure 5.2. The red dots represent the grid points local to a specific processor, with the other colours the relevant ghost points.

Implementing this discretization and distribution is straightforward in an MPI code, however, we have made use of a particular C library where this is standard procedure. That library is the Portable Extensible Toolkit for Scientific Computation (PETSc) [2], which is intended to provide useful tools for the numerical solution of PDEs using a distributed computing environment. More specifics of the structure of

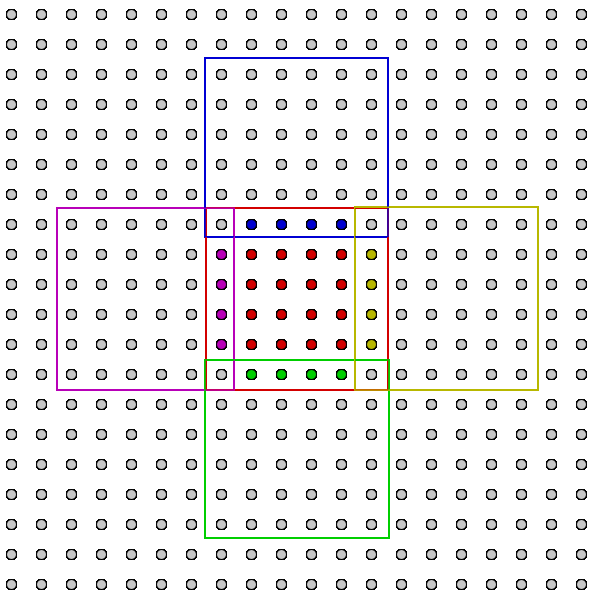

Figure 5.2: A regularly spaced grid on a square domain, split into multiple processors. The red dots represent grid points local to a particular processor. In order for this processor to compute a Laplacian according to Eq. (5.1.21), they must contain *ghost nodes* that are communicated from the local points on neighbouring processors.

the PDE code can be found in Appendix B.3.

Treatment as a finite dimensional system

With the continuous domain discretized into a square periodic grid, the PDE system is effectively a high dimensional dynamical system

$$\partial_t U^D = F^D(U^d, A), \quad F^D : \mathbb{R}^{14N^2} \times \mathbb{R}^{32} \to \mathbb{R}^{14N^2} \tag{5.1.23}$$

for $U^D(t) \in \mathbb{R}^{14N^2}$ the set of all dynamical quantities, and $A \in \mathbb{R}^{32}$ the set of all parameters.

The treatment as a finite dimensional dynamical system may commence as in Section 3.1, but some algorithmic concerns must be taken into account due to the potentially large system size. The main problem that arises is the storage of, and solution to, systems involving the Jacobian. The specific algorithms we use for computations involving the Jacobian are listed in Table 5.1.

All of the algorithms mentioned in the table are provided either by PETSc, or its sister library, the Scalable Library for Eigenvalue Problem Computations (SLEPc) [8]. We provide our own schematic of the relative hierarchy of classes in these libraries in Appendix B.2. The PETSc/SLEPc combination cover all aspects of computation we wish to perform, but we now make a special note on computations regarding periodic orbits.

Problem	Algorithm
Solving a linear system	GMRES [10], preconditioned with incomplete LU factorization of order k (ILU(k)) [9]
Computing eigenvalues	Krylov-Schur iteration [12] • Largest real part by shift • Largest magnitude by straight application • Target eigenvalues by shift-invert methods
Solving nonlinear system	Newton iteration with linesearch [5]; Linear systems solved as above

Table 5.1: Useful algorithms for performing certain computations on large, sparse systems. All of these algorithms are available in the PETSc/SLEPc distributed software libraries.

5.1.4 Periodic orbit computations

To refresh, the linear system to be solved in computing a periodic orbit was written in Section 3.4.4:

$$\begin{aligned} g(U,\beta) &= \begin{bmatrix} U^d - \phi^d(U^d,T,\alpha) \\ P(U^d,T) \end{bmatrix}, \\ \partial_U g(U,\beta) &= \begin{bmatrix} I - \partial_{U^d}\phi^d(U^d,T,\alpha) & -\partial_t\phi^d(U^d,T,\alpha) \\ \partial_{U^d}P & \partial_T P \end{bmatrix}, \end{aligned} \qquad \text{((3.4.4) revisited)}$$

with notation updated to our discretized viewpoint. The problem with this lies in the $\partial_{U^d}\phi$ term. As this can be thought of as "the derivative of the flow at time T, with respect to initial condition u," it becomes apparent that this can be a dense matrix, i.e., small localized perturbations in the initial conditions can possibly influence the entire system over the course of the period. Changing a single component in the initial condition can affect all components by time T. Even with the sparse coupling of our system in Figure 5.1, this is the case.

For a large grid, split onto multiple processors, dealing with dense matrices is not feasible. The solution to this problem comes from looking at the first variational equation

$$\dot{v} = \partial_u f\big|_{u(t)} v. \tag{5.1.24}$$

Keeping in mind that the $\partial_U g$ matrix in Eq. (3.4.4) is multiplied by the vector $[\Delta u, \Delta T]^T$, we can find that the product $\partial_u\phi(u,T,\alpha)\Delta u$ can be approximated by

$$v(T) \text{ such that } v(0) = \Delta u. \tag{5.1.25}$$

Since we already use iterative (matrix-free) algorithms within PETSc/SLEPc, these can simply be turned to this new view where we do not form the matrix explicitly, but rather just have the effect of the matrix multiplication. This approach to periodic orbit computation (and its extension to continuation) was pioneered by Sanchez et al. [11] for use with Navier-Stokes flows.

5.1.5 Initialization of $D_4 \ltimes T^2$ modes

One practical consideration for the simulation of the $D_4 \ltimes T^2$ symmetric waveforms in the multicomponent systems is generating initial conditions to be used that can be compared with the analysis presented above. In general, the numerical computation of the the basis for the nullspace (i.e., the bifurcating eigenmodes) will be different from the basis given in Eq. (3.3.2). The eigenmodes in the basis will be some unknown linear combination of the eigenmodes in Eq. (3.3.2). This section resolves that issue by taking the dispersion relation viewpoint, and determining initial conditions for each of the five $D_4 \ltimes T^2$ symmetric wave modes from there.

Considering the PDE system Eq. (5.1.4), with a complex nullvector Q at the bifurcation point, i.e.,

$$\left(i\omega_c I - \widehat{\partial_U F}(\mathbf{k}_c)\right) Q = 0, \tag{5.1.26}$$

we can use Eq. (5.1.9) and the amplitude relations of Table 3.1 to obtain real-valued expressions for each of the 5 branching modes. These are $U(\mathbf{x},t) - U_0 \propto$

$$\begin{cases} \text{TR}: & \mathrm{Re}(Q)\cos(\omega_c t + k_c x_1) - \mathrm{Im}(Q)\sin(\omega_c t + k_c x_1), \\ \text{SR}: & 2\big[\mathrm{Re}(Q)\cos(\omega_c t) + \mathrm{Im}(Q)\sin(\omega_c t)\big]\cos(k_c x_1), \\ \text{TS}: & \mathrm{Re}(Q)\big(\cos(\omega_c t + k_c x_1) + \cos(\omega_c t + k_c x_2)\big) - \\ & \qquad \mathrm{Im}(Q)\big(\sin(\omega_c t + k_c x_1) + \cos(\omega_c t + k_c x_2)\big), \\ \text{SS}: & 2\Big[\mathrm{Re}(Q)\big(\cos k_c x_1 + \cos k_c x_2\big)\cos\omega_c t - \\ & \qquad \mathrm{Im}(Q)\big(\cos k_c x_1 + \cos k_c x_2\big)\sin\omega_c t\Big] \\ \text{AR}: & \Big[\mathrm{Re}(Q)\big(\cos\omega_c t - \sin\omega_c t\big), + \mathrm{Im}(Q)\big(\cos\omega_c t + \sin\omega_c t\big)\Big] \times \\ & \qquad \big(\cos k_c x_1 + \sin k_c x_1 + \cos k_c x_2 + \sin k_c x_2\big). \end{cases} \tag{5.1.27}$$

These are written with their time dependence because these expressions can be used either when Q is obtained from the PDE system, or even if Q is taken from the integral version of the model, i.e., we use q from Eq. (5.1.9). For initialization of a PDE simulation, it is sufficient to take $t = 0$, however for the (delayed) integral version of the model, an initial history needs to be supplied, and the time dependence of these solutions becomes useful.

The above neglects the actual amplitudes of the solutions, which is reasonable because the numerical normal form analysis does not reveal a precise value for the

unfolding parameter. Without a value for the unfolding parameter, the scaling factors that would make Eq. (5.1.27) equalities are unable to be obtained. These are thus mostly useful in generating the correct *form* of the bifurcating wavemodes, with Q containing information about the relative amplitudes and phases of the various components in the system.

What can be done, in principle, is finding one of the periodic solutions near the bifurcation, and using the scaling factor to give an approximation to a_0 using the relevant entry of Table 3.1. With an approximation to a_0, the amplitudes of all of the other periodic solutions can be approximated, so that even with unstable branches we may be able to obtain reasonably close estimates for the periodic solutions, which can then be refined to the actual solutions.

Now that we have covered how all of the methods generalize to Liley's model, both with continuous and discretized space, we move on to the analysis of parameter sets.

5.2 Parameter set I

5.2.1 Origin

The first parameter set we are going to apply our ideas to are taken from Bojak & Liley [4] where they are used to investigate the generation of oscillations with a 40Hz component. This parameter set was taken from the set of 73,454 physiologically admissible parameter sets that were determined by Bojak & Liley [3], and is displayed in Table 5.2.

In [4], Bojak & Liley perform some SHE and spatially homogeneous periodic orbit continuations in two different parameters: the inhibitory postsynaptic potential amplitudes (simultaneously) $\Gamma_{ie,ii} \to r_1\Gamma_{ie,ii}$, and the local inhibitory-inhibitory connectivity $N_{ii}^{\beta} \to r_2 N_{ii}^{\beta}$. Their results are reproduced in Figure 5.3. And we make note of the idea of a spatially homogeneous periodic orbit, or SHPO.

From there they move on to show how nonzero wave modes will undergo Hopf bifurcation before spatially homogeneous modes (i.e., dynamic Turing bifurcation), as shown in Figure 5.4. They do not perform any analysis of this bifurcation, but instead perform some numerical simulations of Eq. (5.1.4) just beyond the bifurcation point to show the emergence of gamma-band (∼40Hz) *hot spots* in a sharp transition just beyond the bifurcation point. The hot spots occur spontaneously from random initial conditions, with different hot spots shown to exhibit phase correlations among each other.

While the critical frequency at bifurcation suggests periodic solutions with alpha frequency (∼13 Hz), the branching solutions seem to be subcritical and the increase through bifurcation produces a discontinuous jump to large amplitude oscillations with a 40 Hz frequency. This is shown by computing power spectra of the numerical simulations before and after the bifurcation as in Figure 5.5.

Parameter	Value	Units	Parameter	Value	Units
h_e^r	-72.293	mV	N_{ee}^{α}	3228.0	–
h_i^r	-67.261	mV	N_{ei}^{α}	2956.9	–
τ_e	32.209	ms	N_{ee}^{β}	4202.4	–
τ_i	92.260	ms	N_{ei}^{β}	3602.9	–
h_{ee}^{eq}	7.2583	mV	N_{ie}^{β}	443.71	–
h_{ei}^{eq}	9.8357	mV	N_{ii}^{β}	386.43	–
h_{ie}^{eq}	-80.697	mV	v	116.12	$\mathrm{cm\,s^{-1}}$
h_{ii}^{eq}	-76.674	mV	$1/\Lambda$	1.6423	cm
Γ_{ee}	0.29835	mV	$S_e^{\max}$	66.433	$\mathrm{s^{-1}}$
Γ_{ei}	1.1465	mV	$S_i^{\max}$	393.29	$\mathrm{s^{-1}}$
Γ_{ie}	1.2615	mV	μ_e	-44.522	mV
Γ_{ii}	0.20143	mV	μ_i	-43.086	mV
γ_{ee}	122.68	$\mathrm{s^{-1}}$	σ_e	4.7068	mV
γ_{ei}	982.51	$\mathrm{s^{-1}}$	σ_i	2.9644	mV
γ_{ie}	293.10	$\mathrm{s^{-1}}$	p_{ee}	2250.6	$\mathrm{s^{-1}}$
γ_{ii}	111.40	$\mathrm{s^{-1}}$	p_{ei}	4363.4	$\mathrm{s^{-1}}$

Table 5.2: Parameter set PS1 for Liley's model. This parameter set was taken originally from Bojak & Liley [4] where oscillations with a 40Hz component were studied. This is also the principle parameter set used in our verification and testing of the PDE simulation code MFM [7].

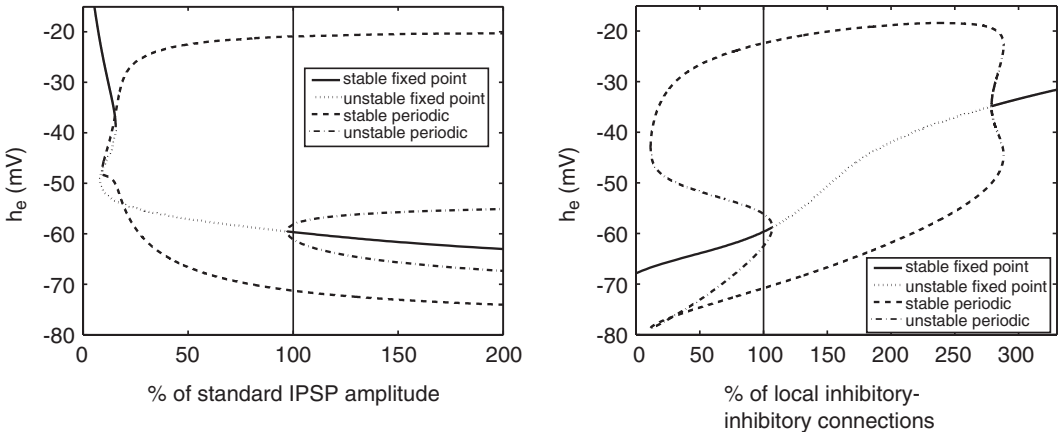

Figure 5.3: Single parameter continuations of SHE and spatially homogeneous periodic orbits. *Left*: Continuation in inhibitory postsynaptic potential amplitudes, $\Gamma_{ie,ii} \to r_1\Gamma_{ie,ii}$, with r_1 in percent. *Right*: Similarly for local inhibitory-inhibitory connectivity $N_{ii}^{\beta} \to r_2 N_{ii}^{\beta}$. *Reproduced with permission from [4].*

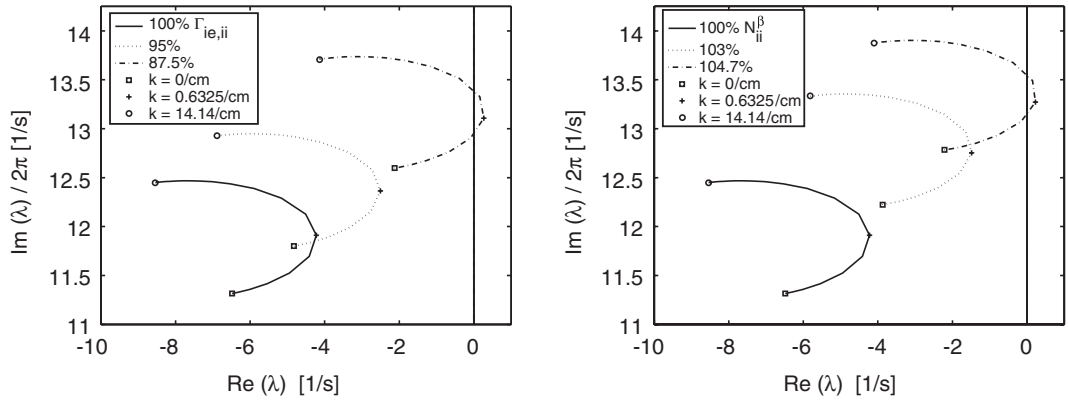

Figure 5.4: Least damped branch of dispersion relations about SHE for various parameter values leading up to dynamic Turing bifurcations. *Left*: Continuation in inhibitory postsynaptic potential amplitudes, $\Gamma_{ie,ii} \to r_1\Gamma_{ie,ii}$, with r_1 in percent. *Right*: Similarly for local inhibitory-inhibitory connectivity $N_{ii}^{\beta} \to r_2 N_{ii}^{\beta}$. *Reproduced with permission from [4].*

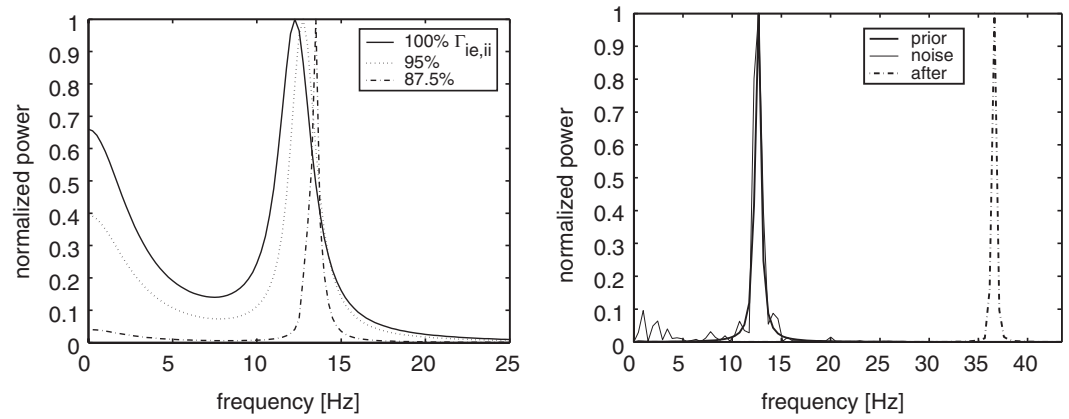

Figure 5.5: Temporal power spectra, normalized to peak power. *Left*: Predictions from linear theory as r_1 is varied through the principal bifurcation. *Right*: Temporal power spectra observed from simulation before and after instability, very different from the prediction of linear theory. *Reproduced with permission from [4].*

5.2.2 Building on previous work

Now comes the time to build on the analysis performed in [4]. First we verify that our numerics are indeed consistent with those that were used in the paper. We check three things:

1. Our implementation of the spatially homogeneous dynamics in Auto-07p is consistent, by comparing continuation of equilibria and periodic solutions in r_2 as in the right panel of Figure 5.3.
2. Our PETSc code for the discretized PDE system is consistent, by
   (a) comparing its spatially homogeneous behaviour to the right panel of Figure 5.3,
   (b) confirming that we see a dynamic Turing bifurcation for $r_2 \lesssim 1.047$, and
   (c) confirming that our temporal power spectrum of simulation behaves as in the right panel of Figure 5.5.
3. Our Maple implementation for dispersion relation calculations is consistent, by comparing our least damped mode to the right panel in Figure 5.4.

All three turn out to give the expected results, which we elaborate on in the next subsections and Section B.4.

Results from discretized PDE viewpoint

Our PETSc simulation code is capable of performing parameter continuation of SHE and SHPO. Thus, it can reproduce the equilibrium curve and the top of the SHPO curve in the right panel of Figure 5.3. Numerically computing the eigenvalues during the continuation of the SHE reveals a dynamic Turing bifurcation occurring for some $r_2 \in [1.044, 1.045]$. The eigenvector found to cause this bifurcation has a structure as displayed in Figure 5.6. It is important to recall that for the square periodic domain, we expect to see the bifurcating modes appear in quadruplets. To observe this numerically, with the Krylov-Schur iterative algorithm, the tolerance must be set finer than usual defaults. This is reflected in the relevant runfile for the thesis' code repository.

Perturbing by the real part of the eigenvector in Figure 5.6, we find that the perturbations do in fact grow. After some time the formation of gamma frequency oscillations and *hot spots* do emerge as described in [4]. After a short amount of time, we observe the hotspot form and produce propagating waves radially outward. After a longer amount of time, the hotspots become spiral waves, and eventually the whole domain becomes engulfed in spiral-like waves. Temporal snapshots of these cases are shown in Figure 5.7, with attention drawn to the black boxes.

Next, we compute the frequency power spectrum of this simulation in one second intervals around three of the temporal evolution events previously described. For the simulation, we generate a time series by averaging the values from a small region (the black squares in Figure 5.7). The simulation is run over 4 seconds, and sampled at 1000 Hz. For the power spectra, we compute the discrete Fourier transform (DFT) of

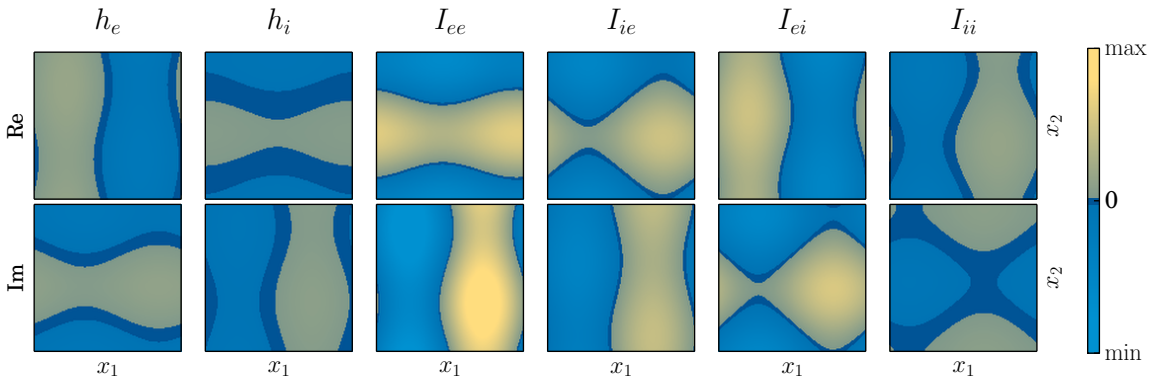

Figure 5.6: Spatial structure of one of the modes causing the left dynamic Turing bifurcation for PS1. The top row is the real part, and bottom imaginary, for six components of the eigenvector computed just beyond the dynamic Turing bifurcation with $r_2 = 1.045$. Computed numerically with Krylov-Schur iteration, the algorithm does not produce the exact modes used in analysis, rather an undetermined linear combination. The algorithm does return 3 additional complex conjugate pairs of vectors, with eigenvalues that match to 7 digits. These eigenvalues are

$$\lambda \approx 4.934091 \times 10^{-5} \pm (8.34590298 \times 10^{-2})i \quad [1/\text{ms}].$$

the discrete time series in the intervals i) $[0, 1]$, ii) $[1.75, 2.75]$, iii) $[2.75, 3.75]$ (seconds) with the resulting power spectrum displayed in Figure 5.8.

Finally, we look at the upper branch of the SHPO. Even though we have precise information about the period of oscillation along the branch, seen in Figure 5.9, we compute a power spectrum in the same way as was done in the general simulation. The time series and spectrum are shown in Figure 5.10. Comparing this to the separate spectra of the simulation, we see slight difference in the first region when the hot spots are forming, and no significant difference as the simulation progresses.

Perturbation by (one of) the principal bifurcating modes has the capacity to produce the large amplitude gamma hot spots that were observed from random initial conditions in Bojak & Liley [4]. From this we can conclude that the square symmetric bifurcating modes of the principal bifurcation should all be subcritical. To check this, we perform the normal form computation based on bifurcation from the dispersion relation.

Results from dispersion relation viewpoint

We apply our continuation of continuous dispersion relations (described in Section 3.4.5) to determine the value of the principal dynamic Turing bifurcation to be $r_2 \approx 1.04453$. This was performed in a Maple code, which can be used to refine this value to arbitrary precision. The least damped branch of the continuous dispersion relation is depicted in Figure 5.11, consistent with Figure 5.4.

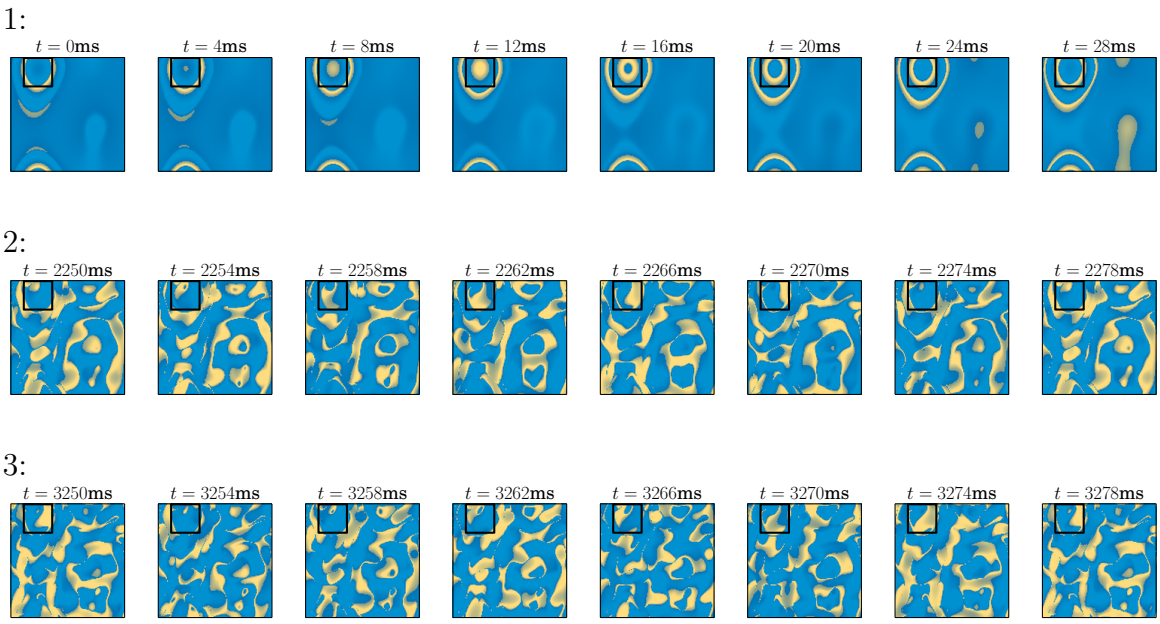

Figure 5.7: Perturbing with the unstable eigenmode from Figure 5.6, the time evolution of the solution (h_e pictured) goes through stages. *1*: After some time of slowly increasing amplitude, localized hotspots of large amplitude emerge in the upper left corner. Time t is measured relative to this first frame. *2*: The radially propagating waves give way to spiral waves. *3*: The waves throughout the domain break up even more, giving even finer spatial structure.

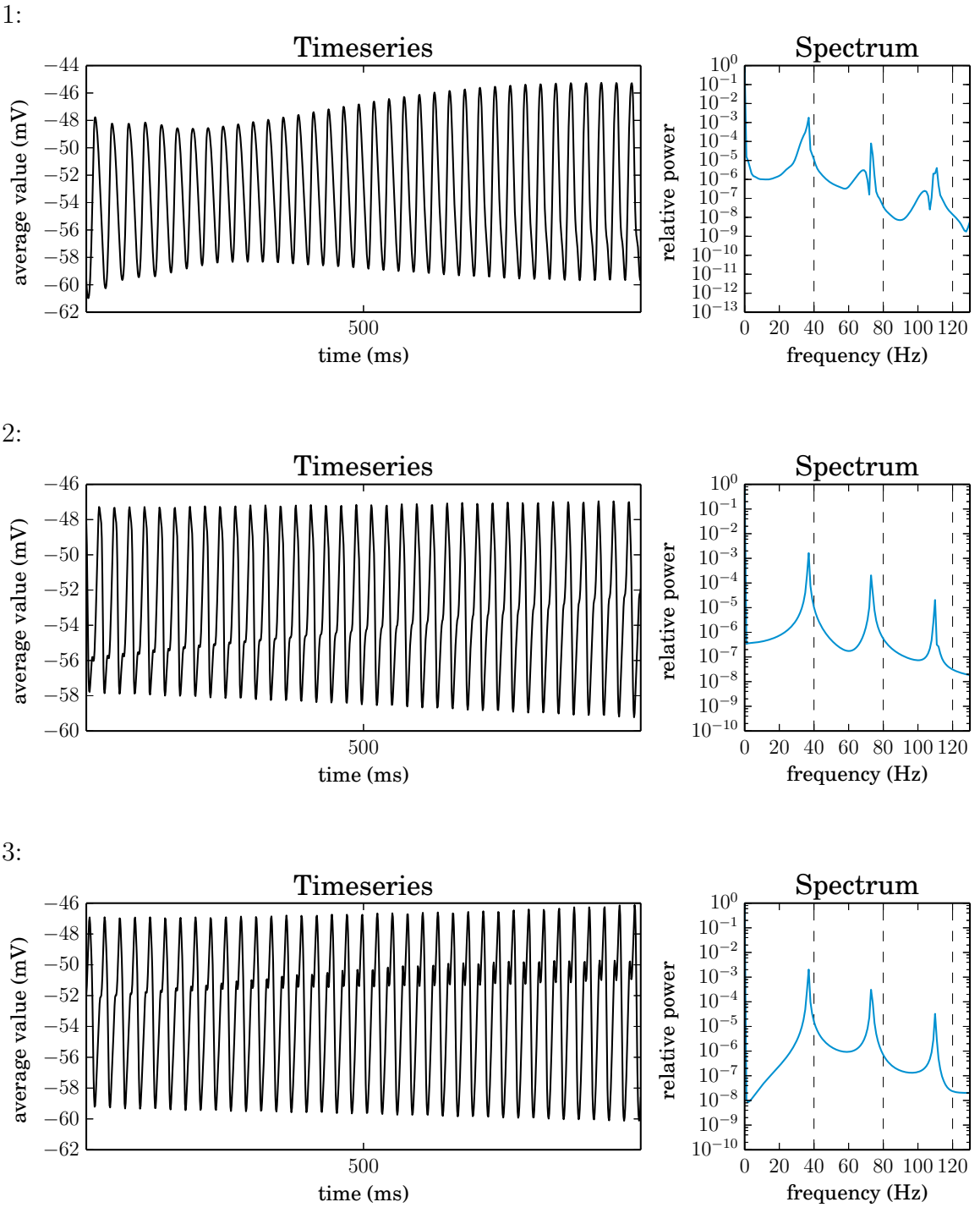

Figure 5.8: Power spectra for 3 time intervals related to the snapshots shown in Figure 5.7. The time series are generated by averaging over the black box regions in Figure 5.7, at 1 ms intervals. The power spectra are obtained by DFT of the discrete time series, as described in the text.

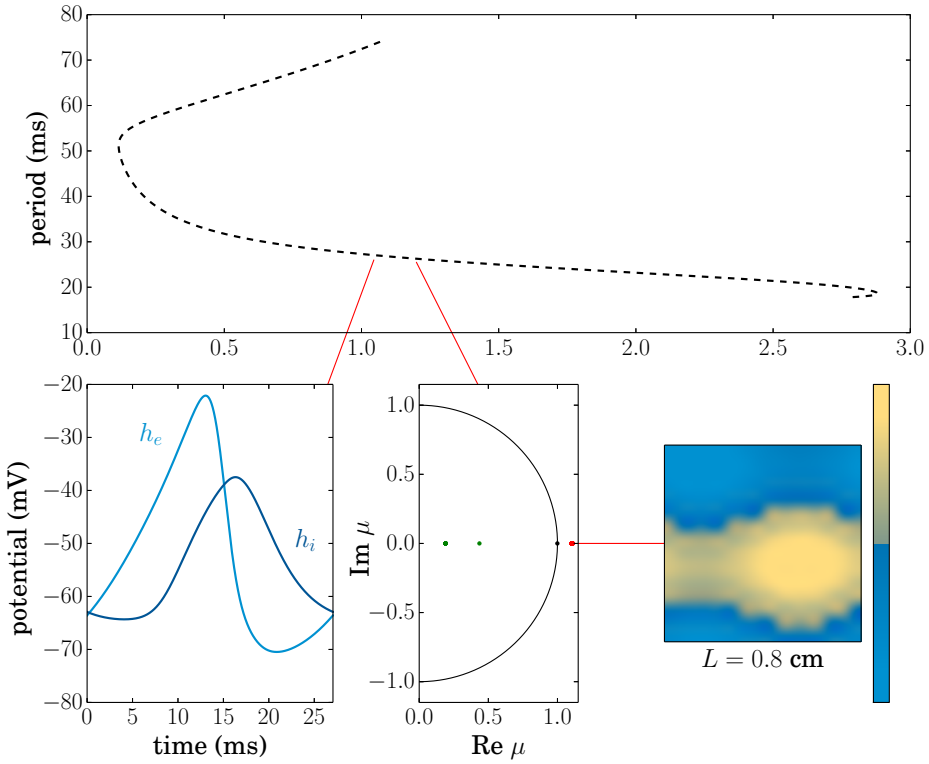

Figure 5.9: Period of oscillation along the SHPO pictured in the right panel of Figure 5.3. The top frame is the period along the entire SHPO branch. Bottom left is the soma membrane dynamics for the period at $r_2 = 1.045$. Bottom center is the largest magnitude Floquet multipliers at $r_2 = 1.2$. Bottom right is spatial structure of an unstable perturbation. The three bottom frames are qualitatively representative of the central portion of the period curve.

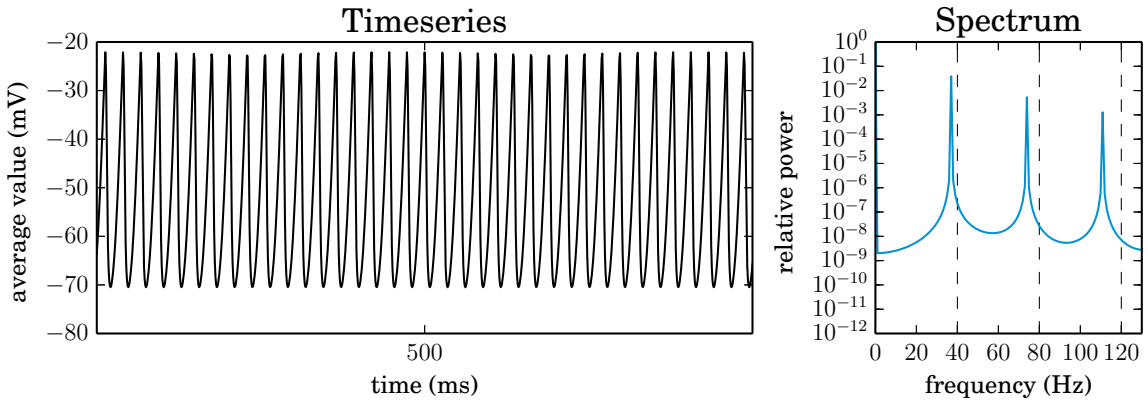

Figure 5.10: Power spectrum for spatially homogeneous periodic solution at $r_2 = 1.045$. The time series was generated by sampling the solution at 1 ms intervals (1000 Hz) for 1 s. The power spectrum is obtained by DFT of the discrete time series, as described in the text.

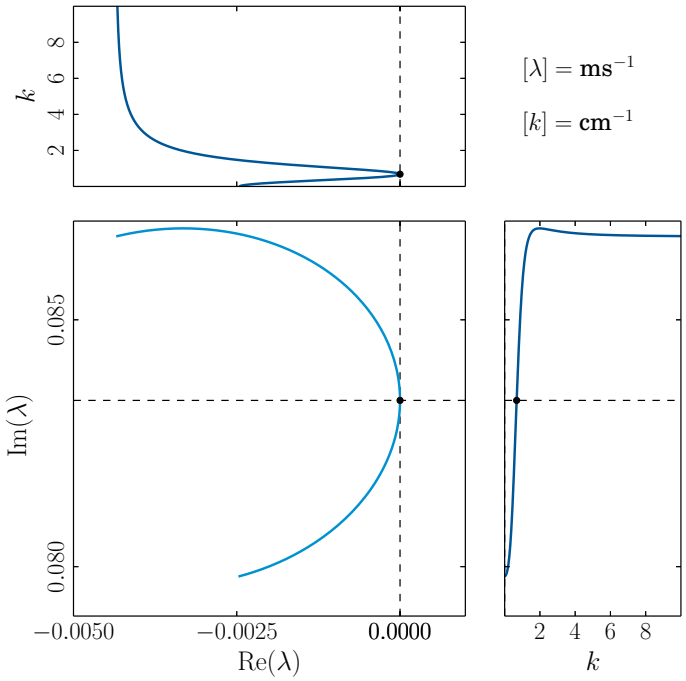

Figure 5.11: Least stable branch of the dispersion relation for SHE of PS1 at $r_2 = 1.04453$. The lower left frame is the branch in the complex plane. The top gives the k dependence of Re λ, and the right gives the k dependence of Im λ.

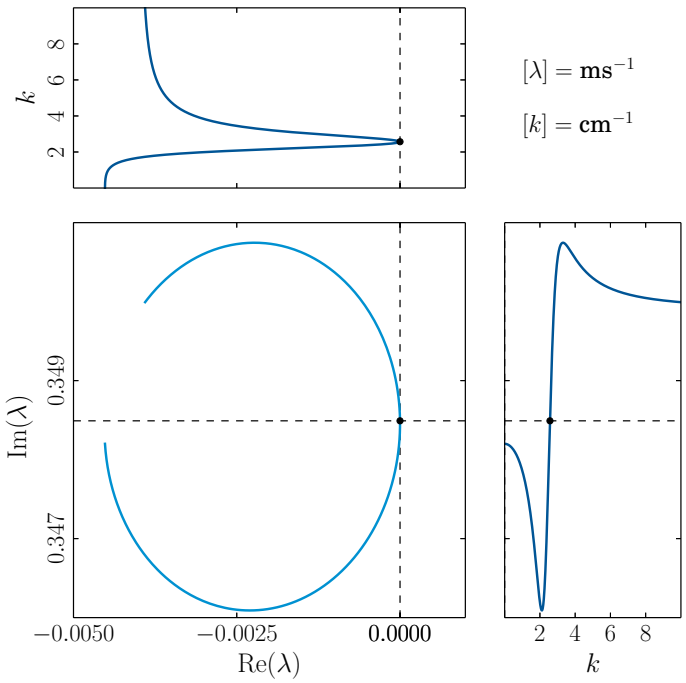

Figure 5.12: Least stable branch of the dispersion relation for SHE of PS1 at $r_2 = 2.84769$.

Parameter	Left Value	Right Value
r_2	1.04453	2.84769
Criticals		
k_c	0.679987 cm^{-1}	2.56537 cm^{-1}
ω_c	0.0833676 ms^{-1}	0.348455 ms^{-1}
Coefficients		
a_1	$(0.34181 - 1.55754i) \times 10^{-3}$	$(-3.20099 + 2.93132i) \times 10^{-5}$
a_2	$(1.11877 - 2.76280i) \times 10^{-3}$	$(-3.20992 + 2.99307i) \times 10^{-5}$
a_3	$(1.55738 - 4.40715i) \times 10^{-3}$	$(-6.46250 + 5.92864i) \times 10^{-5}$
a_4	$(0.82736 - 3.27429i) \times 10^{-3}$	$(-6.55619 + 5.89367i) \times 10^{-5}$
Region:	1	21(-)

Table 5.3: Characterization of the dynamic Turing bifurcations with $D_4 \ltimes T^2$ symmetry. The normal form coefficients result in branching diagram 1 at the left point, and branching diagram 21(-) at the right point.

From the determination of the precise location of the principal bifurcation point, the normal form coefficients, and thus the branching diagrams, can be computed using the method described in Section 5.1.2, and detailed in Appendix B.1. This is done for both ends, with results summarized in Table 5.3.

Putting together the information from both the PDE code and the normal form analysis allows us to obtain a more complete picture of r_2 dependent dynamics for parameter set PS1. This picture is presented in Figure 5.13, where the branching from the principal bifurcations is added in a qualitative rather than quantitative manner.

The unstable subcritical nature of the branches at the left bifurcation point have made our attempts at picking up all of the space dependent periodic solutions fail. We had originally assumed that the right bifurcation point would have the same unstable subcritical branching structure, as we could not yet (historically) compute the normal form coefficients for these bifurcations. With that in mind, we moved to a new parameter set, which contains a supercritical Hopf bifurcation in its homogeneous dynamics. Assuming that a nearby $D_4 \ltimes T^2$ Hopf bifurcation would have similar behaviour, we moved to parameter set PS2, looking first at the problem numerically.

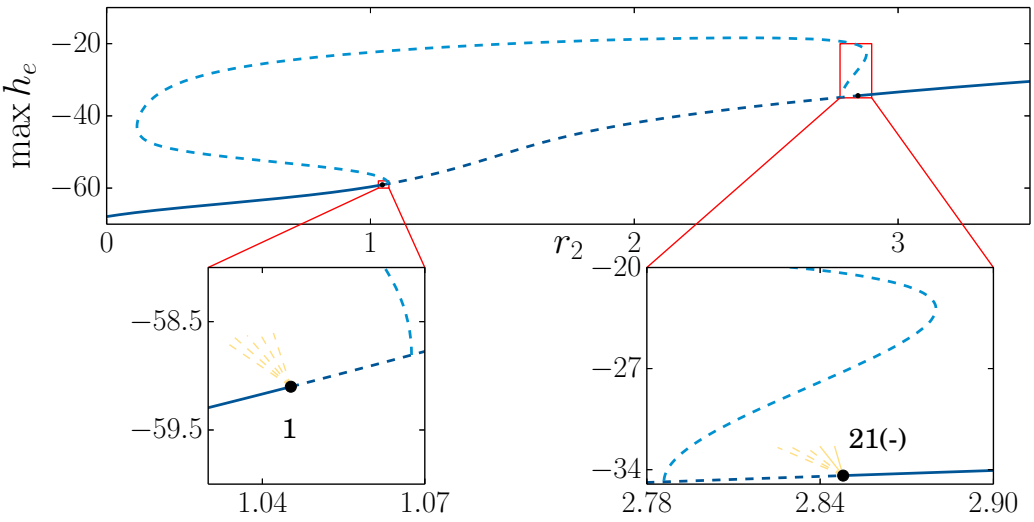

Figure 5.13: SHE and homogeneous PO in the r_1 continuation of the parameter set PS1. The left zoom shows that the principle dynamic Turing bifurcation produces only subcritical $D_4 \ltimes T2$ symmetric wave modes similar to the nearby subcritical homogeneous Hopf. The right zoom shows all $D_4 \ltimes T^2$ modes branching supercriticaly, in contrast to the nearby homogeneous Homogeneous. *Note that the branching diagrams from the principal bifurcations are qualitative and do not reflect the actual amplitudes of $D_4 \ltimes T^2$ wave modes.*

5.3 Parameter set II

5.3.1 Origin

This parameter set (PS2) was part of the set of the 73,454 parameter sets discussed in [3]. While aside from satisfying the physiological constraints that the original paper required, we are unaware of any further analysis performed on this particular set. In general, recall that the database of 73,454 physiological parameter sets was analyzed by Frascoli et al. [6] in an attempt to determine statistics of the nonlinear behaviours. For this thesis, this particular parameter set was chosen because the homogeneous dynamics exhibit a supercritical Hopf bifurcation. In contrast to the previous parameter set, we thought it may be easier to show branching solutions that are supercritical and potentially stable.

The numerical results in this section were originally reported (in part) in van Veen & Green [13], and the parameters are given in Table 5.4.

5.3.2 Building on previous work

As already mentioned, the only previous work done on this particular parameter set was in determining its relevance to physiology and as a piece of a larger statistical analysis. This leaves us quite open ended in how we will proceed. The first thing we

Parameter	Value	Units	Parameter	Value	Units
h_e^r	-71.3473	mV	N_{ee}^{α}	4129.3102	–
h_i^r	-78.2128	mV	N_{ei}^{α}	1884.2588	–
τ_e	112.891	ms	N_{ee}^{β}	4204.8457	–
τ_i	116.4642	ms	N_{ei}^{β}	2867.3399	–
h_{ee}^{eq}	6.0551	mV	N_{ie}^{β}	987.9069	–
h_{ei}^{eq}	-16.8395	mV	N_{ii}^{β}	210.0476	–
h_{ie}^{eq}	-88.0656	mV	v	251.4	$\mathrm{cm\,s^{-1}}$
h_{ii}^{eq}	-88.6666	mV	$1/\Lambda$	3.6643	cm
Γ_{ee}	0.3917	mV	$S_e^{\max}$	69.4	$\mathrm{s^{-1}}$
Γ_{ei}	1.4019	mV	$S_i^{\max}$	320.9	$\mathrm{s^{-1}}$
Γ_{ie}	1.4707	mV	μ_e	-40.9723	mV
Γ_{ii}	1.4264	mV	μ_i	-42.5412	mV
γ_{ee}	551.6	$\mathrm{s^{-1}}$	σ_e	4.2276	mV
γ_{ei}	912.9	$\mathrm{s^{-1}}$	σ_i	2.1897	mV
γ_{ie}	258.5	$\mathrm{s^{-1}}$	p_{ee}	1–10	$\mathrm{s^{-1}}$
γ_{ii}	96.7	$\mathrm{s^{-1}}$	p_{ei}	4.3634	$\mathrm{s^{-1}}$

Table 5.4: Parameter set PS2 for Liley's model. This parameter set was taken originally from a set of 73,454 physiologically admissible parameter sets that were determined by Bojak & Liley [3].

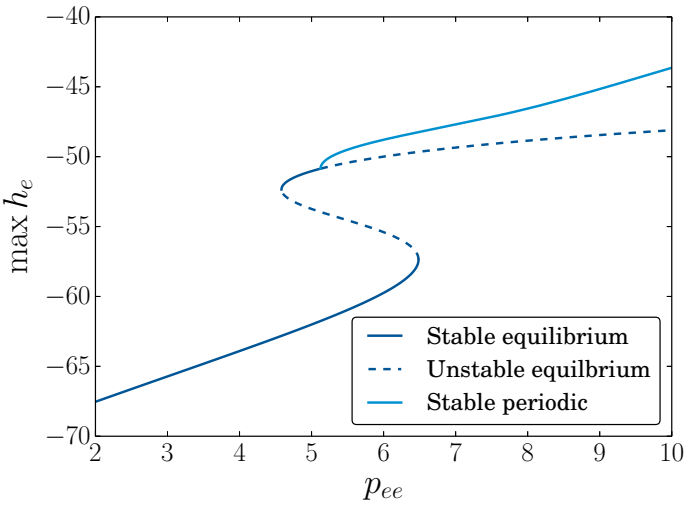

Figure 5.14: The spatially homogeneous dynamics of PS2, continuation in the external excitatory input to excitatory synapses parameter, p_{ee}. Increasing p_{ee}, this parameter set undergoes a pair of fold bifurcations *before* a supercritical Hopf bifurcation to alpha frequency oscillations.

do is a continuation of SHE in the parameter p_{ee}, to give an idea of the state space in response to external excitatory forcing. This continuation is displayed in Figure 5.14.

Normal form analysis

Turning our view to the spatial dependence and dispersion relation, we show that the dynamic Turing bifurcation occurs before the homogeneous Hopf bifurcation, characterized by the entries in Table 5.5, with dispersion relation shown in Figure 5.15. The normal form coefficients determine that we have branching diagram 21(-), the same as the right point in PS1. This branching diagram has all modes bifurcating supercritically, with alternating and travelling rolls being stable.

With this in mind, we turn to simulation, trying to find the stable branches that emerge here. We are not able to successfully pick up either the travelling rolls or the alternating rolls to the right of the bifurcation point. Spatially inhomogeneous perturbations about the SHE at $p_{ee} = 4.95$ (for example) move very quickly away from the upper SHE, and move towards the lower (stable) SHE depicted in Figure 5.14. The homogeneous dynamics seem to overpower the spatially inhomogeneous dynamics at this parameter value.

However, perhaps if we fix the boundaries of our square domain to the SHE values of the upper branch, we can at least compute and observe the standing solutions. This is exactly the approach we took in van Veen & Green [13], and it allows us to compute a supercritical branch of standing square waves.

Parameter	Value
p_{ee}^c	4.94304
Criticals	
k_c	0.363867
ω_c	0.0633570
Coefficients	
a_1	$-(3.65403 + 1.92732i) \times 10^{-4}$
a_2	$-(1.62484 + 0.93401i) \times 10^{-3}$
a_3	$-(2.00397 + 1.20946i) \times 10^{-3}$
a_4	$-(7.71473 + 4.34533i) \times 10^{-4}$
Region:	21(-)

Table 5.5: Characterization of the dynamic Turing bifurcation restricted to $D_4 \ltimes T^2$ symmetry for PS2. The result is region 21(-) from Figure 3.6 where all five periodic modes bifurcate supercritically, with travelling and alternating rolls being stable.

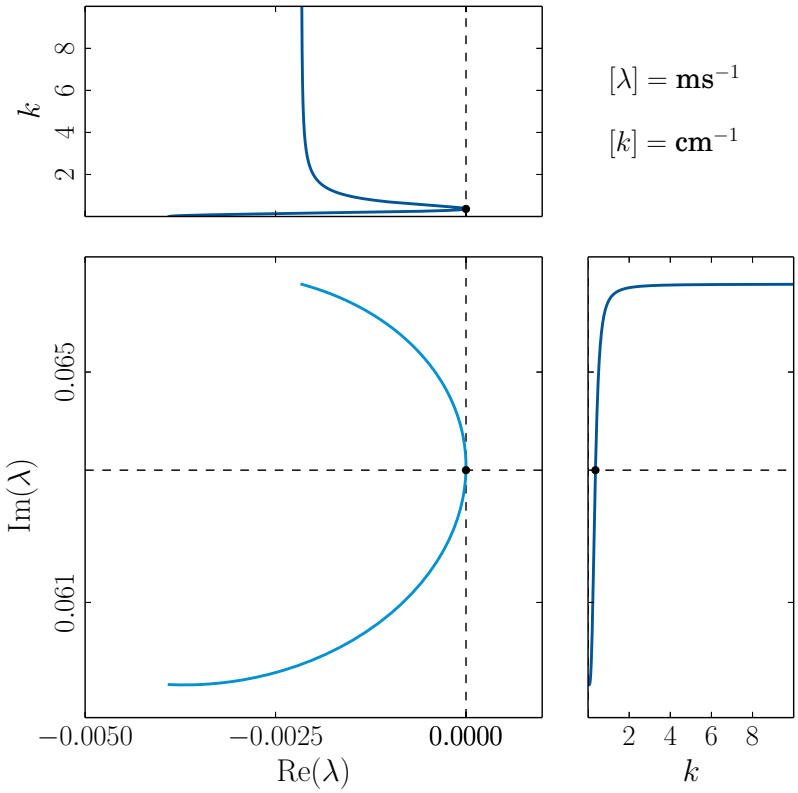

Figure 5.15: Continuous dispersion relation for SHE of PS2 at the dynamic Turing bifurcation with $p_{ee} = 4.94304$.

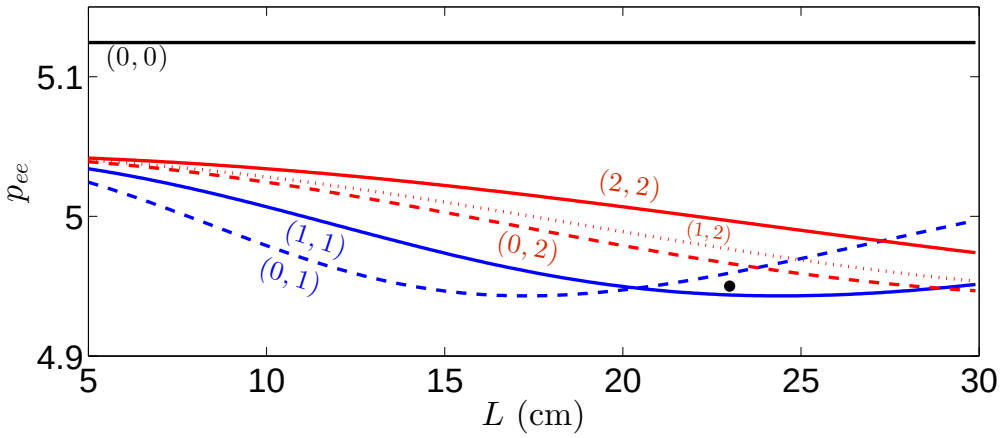

Figure 5.16: PS2 Neutral stability curves for varying length of square domain L. The smallest wave vector that satisfies both periodic and fixed boundary conditions is the $(1, 1)$ mode, so we choose L to be a size such that this mode will become unstable first. The black dot represents a domain size and p_{ee} value where only the $(1, 1)$ mode should be unstable.

Standing square computation

Since we are unable to produce good enough guesses to find the periodic solutions on the square periodic domain, we move now to fixed boundary conditions. For a given p_{ee} value in the neighbourhood of the dynamic Turing bifurcation, we fix the field to the SHE values of the upper branch. This approach has been used by Ashwin et al. [1], and here it ensures that the system can not move towards the lower stable SHE branch as we destabilize.

To determine an appropriate system size for this solution, we introduce yet another way of looking at the system: neutral stability curves. Neutral stability curves are obtained by computing families of solutions to

$$\det\left(i\omega I - \widehat{\partial_U F}((2\pi n/L, 2\pi m/L)^T)\right) = 0. \tag{5.3.1}$$

They represent the neutrally stable eigenvalues for waves with (n, m) wave numbers. They can be computed by solving Eq. (5.3.1) for particular p_{ee}, L, and (n, m), and then extended using continuation methods. Neutral stability curves are shown in Figure 5.16.

If we take $L = 23$ cm, then we do not see the principal bifurcation at $p_{ee} \approx 4.94304$, because the discretization of the dispersion relation does not allow $k_c \approx 0.363867$. Instead, the first bifurcation we see corresponds to the $(1, 1)$ wave mode on this domain. This can be visualized by considering a vertical line in Figure 5.16 with $L = 23$ cm. We have chosen this length because the $(1, 1)$ wave mode satisfies the periodic boundary conditions as well.

The Standing square modes are computed using the algorithm mentioned in Section 5.1.4, and then continued in the p_{ee} parameter. The resulting branch is displayed

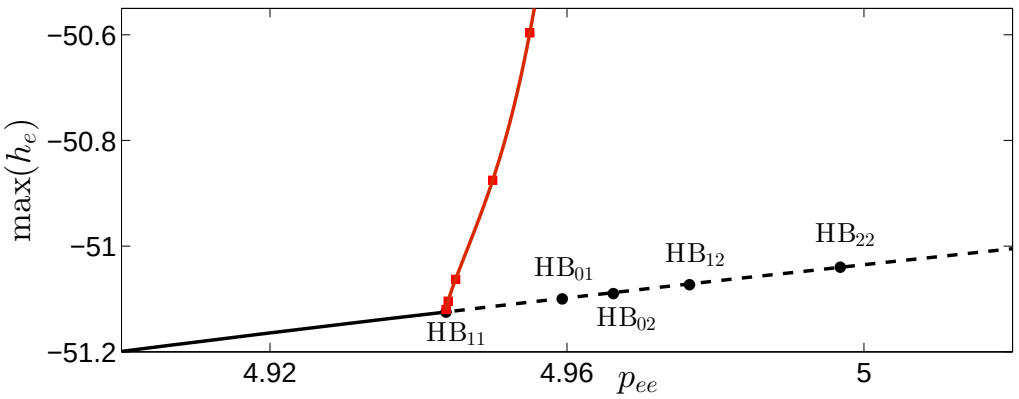

Figure 5.17: Detailed zoom of bifurcation diagram for PS2 with $L = 23$ cm. We compute a branch of standing square solutions emanating from the first bifurcation point. The red squares show show our computed SS solutions, with the red line an interpolant. The secondary bifurcations are noted by black circles, corresponding to the neutral stability curves in Figure 5.16.

in Figure 5.17, with snapshots of a particular solution at $p_{ee} = 4.95$ displayed in Figure 5.18. The branch is seen to bifurcate supercritically, the same as the SHPO branch, and all of the predicted $D_4 \ltimes T^2$ symmetric wave modes of the dynamic Turing bifurcation.

Bibliography

[1] Ashwin, P., Böhmer, K., and Mei, Z. A numerical Liapunov-Schmidt method with applications to Hopf bifurcation on a square. *Mathematics of Computation 64*, 210 (1995), 649–670.

[2] Balay, S., Brown, J., Buschelman, K., Eijkhout, V., Gropp, W. D., Kaushik, D., Knepley, M. G., Curfman, L. M., Smith, B. F., and Zhang, H. PETSc Users Manual. Tech. rep., Argonne National Laboratory, 2012.

[3] Bojak, I., and Liley, D. Modeling the effects of anesthesia on the electroencephalogram. *Physical Review E 71*, 4 (2005), 1–22.

[4] Bojak, I., and Liley, D. Self-organized 40Hz synchronization in a physiological theory of EEG. *Neurocomputing 70* (2007), 2085–2090.

[5] Dennis, J. E., and Schnabel, R. B. *Numerical Methods for Unconstrained Optimization and Nonlinear Equations*. Classics in Applied Mathematics. Prentice-Hall, Englewood Cliffs, NJ, 1983.

[6] Frascoli, F., van Veen, L., Bojak, I., and Liley, D. T. Metabifurcation analysis of a mean field model of the cortex. *Physica D 240*, 11 (2011), 949–962.

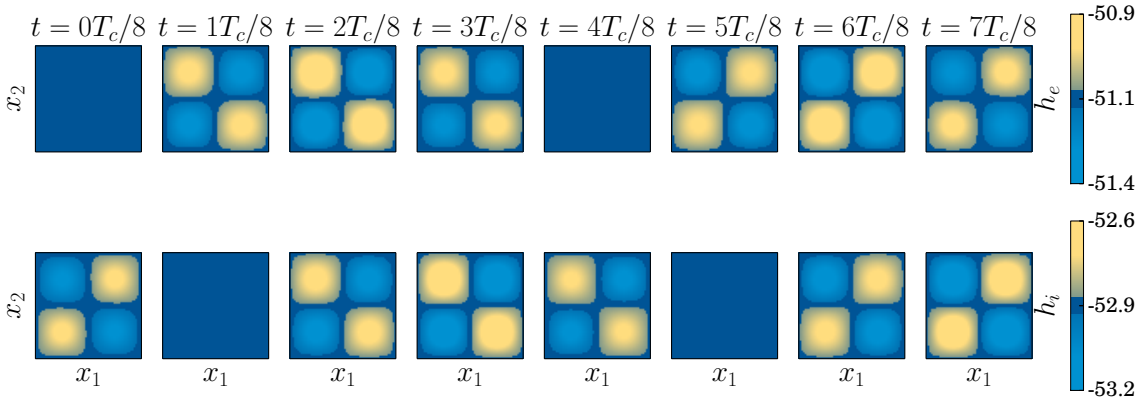

Figure 5.18: Time dependent snapshots of the supercritical SS solution for PS2 with $p_{ee} = 4.95$. Shown are the excitatory and inhibitory soma membrane potentials. In its usual fashion, the inhibitory population is lagging behind the excitatory, this time with a period of about 1/8 the critical period.

[7] Green, K. R., and van Veen, L. Open-source tools for dynamical analysis of Liley's mean-field cortex model. *Journal of Computational Science 5*, 3 (2014), 507–516.

[8] Hernandez, V., Roman, J. E., and Vidal, V. SLEPc: A scalable and flexible toolkit for the solution of eigenvalue problems. *ACM Transactions on Mathematical Software 31*, 3 (2005), 351–362.

[9] Saad, Y. *Iterative Methods for Sparse Linear Systems*, 2 ed. Society for Industrial and Applied Mathematics, Philadelphia, PA, 2003.

[10] Saad, Y., and Schultz, M. H. GMRES: A Generalized Minimal Residual Algorithm for Solving Nonsymmetric Linear Systems. *SIAM Journal on Scientific and Statistical Computing 7*, 3 (1986), 856–869.

[11] Sanchez, J., Net, M., Garcia-Archilla, B., and Simo, C. Newton-Krylov continuation of periodic orbits for Navier-Stokes flows. *Journal of Computational Physics 201*, 1 (2004), 13–33.

[12] Stewart, G. W. Addendum to "A Krylov–Schur Algorithm for Large Eigenproblems", 2002.

[13] van Veen, L., and Green, K. R. Periodic solutions to a mean-field model for electrocortical activity. *The European Physical Journal Special Topics 223*, 13 (2014), 2979–2988.

Chapter 6

Conclusions

6.1 Summary **113**
6.2 Discussion of results **114**
6.2.1 Comparisons and extensions 114
6.3 Conclusions **117**
6.4 Further work **118**
Bibliography **120**

6.1 Summary

The purpose of this thesis was to try to gain some insight into spatiotemporal solutions of neural field models in two dimensional space. While the initial hopes and dreams of the author were grand – to characterize transitions from spatially homogeneous equilibria to wave solutions and eventually to chaotic solutions – the end result became scaled back as we realized that the primary transitions were not understood so well.

This thesis enforced a specific symmetry, $D_4 \ltimes T^2$, on the bifurcating solutions, and developed methods for mapping various neural field models undergoing this bifurcation to a previously studied normal form. The restriction to this particular symmetry was justified on the basis that it still permits the T^2 (translational) symmetric components of the Euclidean symmetry $E(2)$ in two dimensional space, allowing for travelling wave solutions. An additional feature, not discussed in detail in the text, is that any solutions obtained in the $D_4 \ltimes T^2$ space can be transformed by the remaining $E(2)$ generator (i.e., $O(2)$ rotations) and obtain new solutions along a group orbit.

In the case of a general scalar neural field model that incorporates spatiotemporal axonal delays, symbolic expressions for the normal form coefficients were derived. This is a novel result for delayed neural fields in two dimensional space. While similar work has been done for the dynamic Turing bifurcation in one dimension (with $O(2)$

symmetry [10]), and also for Turing bifurcations in two dimensions (with the $D_n \ltimes T^2$ symmetries [2]), analysis of the two dimensional dynamic Turing bifurcation has not been performed on neural fields with delays before this thesis. With our symbolic expressions for normal form coefficients, a specific instance of the general model was then employed to test the results of this analysis, using preexisting simulation software.

For the case of a coupled system of neural field models, which also introduces dynamics for soma membrane potentials, the method used for the scalar equation is extended, but can only be carried out numerically. We know of no published work closer to this than that which was presented, in this thesis, on the scalar model.

Simulation software for a specific multi-population model (Liley's model) was written to be of general use in its simulation, and was turned towards the neighbourhood of the $D_4 \ltimes T^2$ symmetric Hopf bifurcation. Standing square waves were numerically computed and continued away from the bifurcation, in the supercritical direction as predicted by the normal form analysis. The behaviour of the numerical algorithms during the SS branch computation brings up some questions regarding Liley's model.

6.2 Discussion of results

To further zoom in on where this research falls, we provide a deeper comparison of the models and results in this thesis to those in the literature, and discuss how our approach expands on our understanding of, or extends to, other models.

The form of the integral operator that is used in the models of this thesis

$$\eta * K \otimes S\circ$$

generalizes the description of a large number of previously studied neural field models, allowing them to be written in a single convenient notation. While we can not take credit for this simple notation, what we can do is claim that our approach and results can be easily used in homogeneous and isotropic neural field models that were not studied in this thesis.

6.2.1 Comparisons and extensions

Spike frequency adaptation

The models studied in this thesis are missing a piece that is very much present in real biological neurons: metabolism. Through an abundance of metabolic processes, neurons are unable to continuously fire at a high rate, which is referred to as spike frequency adaptation (SFA). While missing in our analysis, a simple extension that can model this effect can be introduced. We can consider a neural field with a local negative feedback component, v

$$\begin{aligned} u &= \eta * (K \otimes S \circ u - av)\,, \\ v &= \eta_{SF} * K_{SF} \otimes S_{SF} \circ u, \end{aligned} \tag{6.2.1}$$

with a a coupling coefficient, and η_{SF}, K_{SF}, and S_{SF} having (potentially) different forms from their synaptic counterparts.

Note that this extension is known to produce Hopf bifurcations as the principal instability more readily than the scalar neural field in this thesis. This such modification was studied in one dimensional space with space dependent delays by Venkov et al. [10] which, recall, applies the method that we have extended to two dimensional space. The analysis in [10] generalized in a very straightforward manner to SFA, and we expect the same for our $D_4 \ltimes T^2$ normal form results.

SFA has also been studied in two dimensional neural field models without delays. Examples of this include the study of spiral waves by Laing [6], and square symmetric waveforms in the more recent book chapter by Ermentrout et al. [4]. While the analysis in [4] is for square symmetric waves, we note that a specific form for the synapse was used in their analysis (similar to the single exponential synapse of Eq. (2.3.3)), there are no symbolic expressions for the normal form coefficients, and again we note that the model does not incorporate spatiotemporal delays. Our analysis generalizes this to some extent by allowing for an arbitrary synapse and including spatiotemporal delay.

To fully generalize the results by Ermentrout et al. [4], we would have to extend to incorporate the SFA as in Eq. (6.2.1). This seems to be as straightforward in two dimensional space as in the one dimension. We did not perform this, however, because our interests were more directed at multiple populations.

A specific type of SFA, called *synaptic depression* has recently been added to Liley's model by Bojak et al. [1]. It adds a slowly varying temporal component to the the PSP peak amplitudes Γ_{jk}. Note that this has been included in this subsection even though SFA deals with *frequency* modulation. The reason for this is because in Liley's model the PSP peak amplitudes always appear in product with the maximum firing rates S_k^{max} (i.e., minimum frequency), so regardless of which one is actually changing, they can be handled in an equivalent way. The model in [1] can be written as

$$\begin{aligned} h_k(\mathbf{x},t) &= \eta_k * \left(h_k^r + \sum_j \frac{h_{jk}^{eq} - h_k(\mathbf{x},t)}{\left| h_{jk}^{eq} - h_k^r \right|} I_{jk}(\mathbf{x},t) \right), \\ I_{jk}(\mathbf{x},t) &= \eta_{jk} * \left(K_{jk} \otimes \left(C_j(\mathbf{x},t) S_j \circ h_j(\mathbf{x},t) \right) + p_{jk} \right), \\ C_j(\mathbf{x},t) &= \eta_j^{SFA} * K_j^{SFA} \otimes S_j \circ h_j(\mathbf{x},t), \end{aligned} \tag{6.2.2}$$

noting that [1] treats the newly introduced variables C_j as having purely local influence, similar to the inhibitory population in the PDE version of Liley's model. The results of Bojak et al. were based on numerical simulation on a square periodic domain, looking at space dependent *burst suppression*. The methods of this thesis are thus particularly suited to comparison with the results of the modified model. As [1] is a very recent article, this has not been performed yet.

Multiple populations

We have already considered the extension to multiple populations in a specific sense within this thesis. Extending the analysis from the scalar field to Liley's model involved both the introduction of a second population and additional dynamics for the soma membrane potentials.

The approach to extending the scalar model to Liley's model is quite general, however in this thesis it was presented more from the viewpoint of practicality. That is, we wanted to study the primary instabilities in Liley's model, so the notation of our numerical approach (the short form of Eq. (B.6) for example) was developed with the sole purpose of being practical with the analysis of Liley's model.

Multi-population neural field models have existed all the way back to Wilson & Cowan in the 1970s [11, 12], whose model (generalized to space in Ermentrout & Cowan [3]) can be expressed as:

$$\begin{aligned} u_e &= \eta_e * S_e \circ (K_{ee} \otimes u_e + K_{ie} \otimes u_i)\,, \\ u_i &= \eta_i * S_i \circ (K_{ei} \otimes u_e + K_{ii} \otimes u_i)\,, \end{aligned} \tag{6.2.3}$$

with single exponential synapses and no spatiotemporal delay. One particular thing to note about Eq. (6.2.3) is the order of the $\circ$ and $\otimes$ operators. This is the reverse of the order for models studied in this thesis, but it is easily explained. The difference can be traced to how the population averages are interpreted. With the viewpoint of "sum connections, and then convert to average firing rate," then the $\eta * S \circ K \otimes$ order will come up. With the viewpoint of "convert to average firing rate, and then sum connections," then the $\eta * K \otimes S \circ$ ordering will be present. Neither of these seem to be the definitive model, and it seems that qualitative behaviour of both variants have a similar repertoire. In fact, as the nonlinear analysis presented in this thesis relies on what are essentially Taylor expansions, the analysis could be easily converted to this other view and the qualitative behaviours of both types could be compared. In the interest of time, this was not conducted.

One particularly relevant paper (introduced to us only after we had performed all of our computations) is that of Tass [9]. Tass performs an analysis of Eq. (6.2.3) with single exponential time scales and no spatiotemporal delays. As the synapse is specified, he is able to determine a symbolic expression for the frequency at bifurcation. He goes through the procedure of computing *order parameter equations* for various cases, one of which corresponding to square symmetric modes. The resulting equations (which includes symbolic expressions for all coefficients) seem to be equivalent to the $D_4 \ltimes T^2$ normal form of Silber & Knobloch, up to some scaling.

Our normal form analysis extends Tass' work in the following three ways: i) It incorporates the (biologically relevant) axonal delays into the models, ii) It generalizes the synapses such that more biologically realistic models can be used (i.e., nonzero rise time), and iii) It adds a model for soma membrane dynamics to the mix, still allowing for the square modes to be analyzed (although, numerically).

Perhaps the most relevant comparison between Tass' work and this thesis can be stated as follows: Tass determines that the only modes that are possibly stable in the

square symmetric reduction of the neural field in his work are the TR and AR states. Even though we are unable to make such a strong statement (our symbolic expressions for the normal form coefficients are quite difficult to work with analytically) we have only observed stability for the TR and AR states. The three other modes that are guaranteed to branch by the Equivariant Hopf Theorem appear to always be stable in both our scalar field with delay and Liley's model. It may be possible to show this result from our symbolic normal form coefficients, however we were unable to achieve this.

6.3 Conclusions

Scalar field

For scalar neural fields with transmission delay undergoing a pair of dynamic Turing bifurcations, the emergence of this pair can be visualized through the sigmoid steepness parameter. For low enough steepness, there will be no such bifurcation, but increasing through a critical value will create a pair of (reflected) Hopf bifurcations originating in some region of the normal form coefficient space. In our investigations, this has always been regions 21/21(-), but may be different for different model specifics. These regions have all solutions bifurcating supercritically, with travelling rolls and standing squares (or alternating rolls) being stable. It is likely that the branches of periodic solutions connect the Hopf bifurcations in this regime.

Increasing sigmoid steepness eventually moves the $D_4 \ltimes T^2$ normal form coefficients towards regions 1/1(-). These regions have all 5 guaranteed solutions bifurcating subcritically and being unstable. The path taken in approaching this region is dependent largely on the underlying model, i.e., the specifics of the spatiotemporal connectivity and the synapse, so we may not comment on which regions will be traversed.

As the steepness approaches infinity (a Heaviside firing function) the normal form coefficients also approach infinity in magnitude in region 1, meaning that the bifurcating wave modes will be subcritical and their amplitudes will go to zero. With a Heaviside firing rate, the condition for a Hopf bifurcation can not possibly be met, which can be thought of as consistent with a zero amplitude branching structure.

Liley's model

From the analysis performed, we can only conclude that the temporal dynamics of the spatially homogeneous modes tell us a lot about the temporal power spectrum in the regions of instability. This is demonstrated by comparing the frequencies of general simulation to the frequency of the spatially homogeneous oscillations as in Figures 5.8 and 5.10. This is likely due to the relatively weak spatial coupling that is present in this particular model.

For Liley's model, considering the spatial dependence in the analysis has been most successful from the point of view of determining the precise location and branching of the principal bifurcation. This provides a means for predicting when small perturba-

tions will grow to large amplitude waves in the neighbourhood of the bifurcation, i.e., we now have predictive power over this phenomena. A key result however, displayed in Figure 5.13, shows us that the $D_4 \ltimes T^2$ symmetric Hopf modes do not always branch in the same way (criticality and stability) as the nearby, and related, spatially homogeneous oscillations.

We suspect that advancing the numerics now to pick up *known* branching solutions and continue them will shed light on further bifurcations leading to the more complicated dynamical regimes like the hot spots.

General

The above were concerned strictly with the results as they pertain to the models, without any mention of reality. To be explicit, this thesis contained no attempt to directly match experimental data. However, we can relate the results in a qualitative sense to experimental observations. Muller et al. observe propagating activity waves by voltage sensitive dye (VSD) imaging the cortex of awake monkey [8]. The observations provide the first concrete evidence of propagating activity in the cortex of an awake, conscious being. The travelling wave mode that is observed resembles that of a travelling roll, as with cortex waves in past work on anaesthetized subjects (Muller & Destexhe [7]).

The results of Muller et al. are consistent with our calculations showing that the TR modes appear to be one of the two square symmetric modes that can be stable. We suspect that in the absence of the square periodic symmetry, the AR state may always be unstable as well, leaving us with stable TR solutions for some parameter values. This is not to say that the TR solutions will be the only possible solutions, rather that from the analysis of this thesis, and the recent experimental results, they should be the primary target for expanding on our results.

6.4 Further work

The previous sections alluded to further work that could be conducted to gain a better understanding of how the results of this thesis exist among existing results. This section now presents the directions that will advance results.

Tiling symmetries

Since dynamic Turing bifurcation plays an important role in neural systems with long range excitatory connections and time delays, it should be of principal importance to understand its behaviour in a more varied sense. Restrictions to the other two dimensional tiling symmetries will add to the picture presented here. The *stability* of the square symmetric modes in this thesis refers only to stability in the square periodic lattice. It will be very beneficial to compare results among the tiling symmetries, to see if there is a particular mode that consistently dominates the others. My prediction:

Travelling rolls are king.

Numerical methods

With the now known branching behaviour, numerics can be tuned around attempting to pick up small amplitude branching solutions and performing continuation to larger amplitude solutions. This process is sure to reveal what methods should be used for the general simulation of the scalar delayed field and Liley's model.

Continuation of the branch of standing square solutions using [5] posed a very difficult problem numerically. Using the ideas presented in Section 5.1.4, we found that the nonlinear residuals were not decreasing quadratically as we would expect for Newton's method. In fact, we required the use of a line search method to adjust the length of our Newton updates, and even with this our approach would not converge beyond a lower limit.

This presents a mystery to us, and we think the solution likely lies in one of the possibilities:

- The convergence of the periodic orbit refinement is limited by the spatial discretization error, or
- The numerics for discretizing and time stepping the model are inadequate.

The first point can be addressed simply by adjusting the spatial discretization and comparing convergence results between them. The second point would require a little more work, perhaps writing a pseudospectral code to apply in the neighbourhood of the bifurcations of interest.

Symmetry breaking

Restriction to the tiling symmetries with length and time scales of the principle bifurcation is just the first step. The nature of the dynamic Turing bifurcation, however, is that there can be many (up to infinite) bifurcations with different scales in a small region. An important question then becomes: How do these bifurcations at different scales interact among each other? Especially, since we have enforced a particular symmetry on the principal bifurcation.

Radial and rotating waves

Simulation of Liley's model, as demonstrated in Figure 5.7, shows the formation of localized sources of activity which, due to the periodic boundary conditions, end up interacting with themselves and creating spiral waves. With periodic boundaries removed, it is plausible that the localized sources would be radially symmetric, and their destabilization into spiral waves could be studied from this angle. While there is currently work on spiral waves in neural fields, the extension to multiple populations (and Liley's model) with spatiotemporal delay would be very interesting to see.

Inhomogeneity, Anisotropy

Of course, the cortex is not homogeneous, nor is it isotropic. That does not mean, however, that the results of this thesis are useless. Rather, they can form the beginnings of more realistic analysis. We now know how to characterize the generation of square symmetric wave modes. How does their character change when K is *slightly* anisotropic? *Slightly* inhomogeneous? What happens when the axonal delays have small inhomogeneities or anisotropies? We should try to figure these out!

Bibliography

[1] Bojak, I., Stoyanov, Z. V., and Liley, D. T. J. Emergence of spatially heterogeneous burst suppression in a neural field model of electrocortical activity. *Frontiers in Systems Neuroscience 9* (2015), 1–20.

[2] Bressloff, P. C., Cowan, J. D., Golubitsky, M., Thomas, P. J., and Wiener, M. C. Geometric visual hallucinations, Euclidean symmetry and the functional architecture of striate cortex. *Philosophical transactions of the Royal Society of London B 356*, 1407 (2001), 299–330.

[3] Ermentrout, G. B., and Cowan, J. D. A mathematical theory of visual hallucination patterns. *Biological Cybernetics 34* (1979), 137–150.

[4] Ermentrout, G. B., Folias, S. E., and Kilpatrick, Z. P. Spatiotemporal pattern formation in neural fields with linear adaptation. In *Neural Fields*, S. Coombes, P. biem Graben, R. Potthast, and J. J. Wright, Eds. Springer, 2014, ch. 4.

[5] Green, K. R., and van Veen, L. Open-source tools for dynamical analysis of Liley's mean-field cortex model. *Journal of Computational Science 5*, 3 (2014), 507–516.

[6] Laing, C. R. Spiral Waves in Nonlocal Equations. *SIAM Journal on Applied Dynamical Systems 4*, 3 (2005), 588–606.

[7] Muller, L., and Destexhe, A. Propagating waves in thalamus, cortex and the thalamocortical system: Experiments and models. *Journal of physiology, Paris 106* (2012), 222–238.

[8] Muller, L. E., Reynaud, A., Chavane, F., and Destexhe, A. Propagating waves structure spatiotemporal activity in visual cortex of the awake monkey. *BMC Neuroscience 14*, Suppl 1 (2013), O8.

[9] Tass, P. Oscillatory Cortical Activity during Visual Hallucinations. *Journal of Biological Physics 23*, 1 (1997), 21–66.

[10] Venkov, N., Coombes, S., and Matthews, P. Dynamic instabilities in scalar neural field equations with space-dependent delays. *Physica D 232*, 1 (2007), 1–15.

[11] Wilson, H. R., and Cowan, J. D. Excitatory and Inhibitory Interactions in Localized Populations of Model Neurons. *Biophysical Journal 12*, 1 (1972), 1–24.

[12] Wilson, H. R., and Cowan, J. D. A mathematical theory of the functional dynamics of cortical and thalamic nervous tissue. *Kybernetik 13*, 2 (1973), 55–80.

Appendix A

Resources for scalar equation

A.1 Calculations 123
A.1.1 Details of separation of scales calculation 123
A.1.2 Details of Fredholm alternative inner products 127
A.2 Initialization files for nfSimulator 129

A.1 Calculations

A.1.1 Details of separation of scales calculation

For the separation of scales calculation, we use the integral notation of the model as seen in Eq. (2.3.1) with the operator notation expanded. We first write the model making explicit the dependence of u on the scaled independent variables $\boldsymbol{\chi} = \epsilon\mathbf{x}$, $\theta = \epsilon t$, and $\tau = \epsilon^2 t$ leading to

$$u(\mathbf{x}, t, \epsilon\mathbf{x}, \epsilon t, \epsilon^2 t) = \int_{-\infty}^{t} \mathrm{d}s\ \eta(t-s)\times \\ \times \int_{-\infty}^{\infty}\int_{-\infty}^{\infty} \mathrm{d}x_1'\mathrm{d}x_2' \int_{-\infty}^{\infty} \mathrm{d}t'\ K(\mathbf{x}-\mathbf{x}', s-t') f \circ u(\mathbf{x}', t', \epsilon\mathbf{x}', \epsilon t', \epsilon^2 t') \quad \text{(A.1)}$$

Taylor expanding (A.1) about the homogeneous equilibrium as in (4.3.6), the integral equation becomes

$$u(\mathbf{x},t,\epsilon\mathbf{x},\epsilon t,\epsilon^2 t)=\sum_{i=0}^{\infty}\gamma_i\int \mathrm{d}s\,\eta(t-s)\iint \mathrm{d}\Omega'\times \\ \times\int \mathrm{d}t'\,K(\mathbf{x}-\mathbf{x}',s-t')u_i(\mathbf{x}',t',\epsilon\mathbf{x}',\epsilon t',\epsilon^2 t'), \quad \text{(A.2)}$$

where here (and throughout this appendix) we omit the limits of integration for simplicity, and use $\mathrm{d}\Omega'=\mathrm{d}x_1'\mathrm{d}x_2'$.

For the integral part of (A.2), adding and subtracting each of the scaled coordinates in the appropriate place allows us to write

$$\begin{aligned}u_i(\mathbf{x}',t',\epsilon\mathbf{x}',\epsilon t',\epsilon^2 t')&=u_i(\mathbf{x}',t',\epsilon\mathbf{x}+\epsilon\mathbf{x}'-\epsilon\mathbf{x},\epsilon t+\epsilon t'-\epsilon t,\epsilon^2 t+\epsilon^2 t'-\epsilon^2 t)\\&=u_i(\mathbf{x}',t',\boldsymbol{\chi}+\epsilon(\mathbf{x}'-\mathbf{x}),\theta+\epsilon(t'-t),\tau+\epsilon^2(t'-t)),\end{aligned}$$

for each separate order of the perturbation solutions. Taylor expanding the last 3 arguments of this leads to

$$\begin{aligned}u_i(\mathbf{x}',t',\epsilon\mathbf{x}',\epsilon t',\epsilon^2 t') \quad &= \quad u_i(\mathbf{x}',t',\boldsymbol{\chi},\theta,\tau) \quad +\\ &+\epsilon\left[(\mathbf{x}'-\mathbf{x})\cdot\nabla_\chi+(t'-t)\frac{\partial}{\partial\theta}\right]u_i(\mathbf{x}',t',\boldsymbol{\chi},\theta,\tau) \quad +\\ &+\epsilon^2\left[\frac{1}{2}\left((\mathbf{x}'-\mathbf{x})\cdot\nabla_\chi+(t'-t)\frac{\partial}{\partial\theta}\right)^2+(t'-t)\frac{\partial}{\partial\tau}\right]u_i(\mathbf{x}',t',\boldsymbol{\chi},\theta,\tau) \quad +\\ &+\mathcal{O}(\epsilon^3),\end{aligned} \quad \text{(A.3)}$$

where $\nabla_\chi=(\frac{\partial}{\partial\chi_1},\frac{\partial}{\partial\chi_2})^T$.

Now the integral terms of (A.2) become

$$\begin{aligned}&\int \mathrm{d}s\,\eta(t-s)\iint \mathrm{d}\Omega'\int \mathrm{d}t'\,K(\mathbf{x}-\mathbf{x}',s-t')u_i(\mathbf{x}',t',\epsilon\mathbf{x}',\epsilon t',\epsilon^2 t')=\\ &\qquad\int \mathrm{d}s\,\eta(t-s)\iint \mathrm{d}\Omega'\int \mathrm{d}t'\,K(\mathbf{x}-\mathbf{x}',s-t')\Big\{u_i(\mathbf{x}',t',\boldsymbol{\chi},\theta,\tau)+\\ &\qquad\qquad+\epsilon\left[(\mathbf{x}'-\mathbf{x})\cdot\nabla_\chi+(t'-t)\frac{\partial}{\partial\theta}\right]u_i(\mathbf{x}',t',\boldsymbol{\chi},\theta,\tau)+\\ &+\epsilon^2\left[\frac{1}{2}\left((\mathbf{x}'-\mathbf{x})\cdot\nabla_\chi+(t'-t)\frac{\partial}{\partial\theta}\right)^2+(t'-t)\frac{\partial}{\partial\tau}\right]u_i(\mathbf{x}',t',\boldsymbol{\chi},\theta,\tau)+\mathcal{O}(\epsilon^3)\Big\}.\end{aligned} \quad \text{(A.4)}$$

Every order of ϵ can be broken down into the convolution notation using $*$ and $\otimes$, and to do so requires us to use $t'-t=(s-t)+(t'-s)$ to move between the time scales. Using this, and pulling the ϵ powers out of the integrals, we can continue from

(A.4)

$$
\begin{aligned}
&= \int \mathrm{d}s\,\eta \iint \mathrm{d}\Omega' \int \mathrm{d}t'\, K u_i + \\
&+ \epsilon\Bigg\{ \int \mathrm{d}s\,\eta \iint \mathrm{d}\Omega' \int \mathrm{d}t'\, (\mathbf{x}' - \mathbf{x})\, K \cdot \nabla_\chi u_i + \\
&\qquad + \int \mathrm{d}s\,(s-t)\eta \iint \mathrm{d}\Omega' \int \mathrm{d}t'\, K \frac{\partial u_i}{\partial \theta} + \\
&\qquad + \int \mathrm{d}s\,\eta \iint \mathrm{d}\Omega' \int \mathrm{d}t'\,(t'-s) K u_i \Bigg\} \quad + \\
&+ \frac{\epsilon^2}{2}\Bigg\{ \int \mathrm{d}s\,\eta \iint \mathrm{d}\Omega' \int \mathrm{d}t'\, K \left((\mathbf{x}' - \mathbf{x}) \cdot \nabla_\chi\right)^2 u_i + \\
&\qquad + 2 \int \mathrm{d}s\,(s-t)\eta \iint \mathrm{d}\Omega' \int \mathrm{d}t'\,(\mathbf{x}' - \mathbf{x}) K \cdot \nabla_\chi \frac{\partial u_i}{\partial \theta} + \\
&\qquad + 2 \int \mathrm{d}s\,\eta \iint \mathrm{d}\Omega' \int \mathrm{d}t'\,(t'-s) K (\mathbf{x}' - \mathbf{x}) K \cdot \nabla_\chi \frac{\partial u_i}{\partial \theta} + \\
&\qquad + \int \mathrm{d}s\,(s-t)^2\eta \iint \mathrm{d}\Omega' \int \mathrm{d}t'\, K \frac{\partial^2 u_i}{\partial \theta^2} + \\
&\qquad + 2 \int \mathrm{d}s\,(s-t)\eta \iint \mathrm{d}\Omega' \int \mathrm{d}t'\,(t'-s) K \frac{\partial^2 u_i}{\partial \theta^2} + \\
&\qquad + \int \mathrm{d}s\,\eta \iint \mathrm{d}\Omega' \int \mathrm{d}t'\,(t'-s)^2 K \frac{\partial^2 u_i}{\partial \theta^2} + \\
&\qquad + 2 \int \mathrm{d}s\,(s-t)\eta \iint \mathrm{d}\Omega' \int \mathrm{d}t'\, K \frac{\partial u_i}{\partial \tau} + \\
&\qquad + 2 \int \mathrm{d}s\,\eta \iint \mathrm{d}\Omega' \int \mathrm{d}t'\,(t'-s) K \frac{\partial u_i}{\partial \tau} \Bigg\} \quad + \\
&+ \mathcal{O}(\epsilon^3)
\end{aligned}
\tag{A.5}
$$

noting that the arguments of η, K, and u_i remain the same.

From equation (A.5) we can easily read off the convolutions after we have expanded

terms involving $(\mathbf{x}' - \mathbf{x}) \cdot \nabla_\chi$, resulting in

$$
\begin{aligned}
&= \eta * K \otimes u_i + \\
&\quad + \epsilon \Bigg\{ -\eta * \left(x_1 K \otimes \frac{\partial}{\partial \chi_1} + x_2 K \otimes \frac{\partial}{\partial \chi_2} \right) - (t\eta * K + \eta * tK) \otimes \frac{\partial}{\partial \theta} \Bigg\} u_i \quad + \\
&\quad + \epsilon^2 \Bigg\{ \frac{1}{2} \eta * \left(x_1^2 K \otimes \frac{\partial^2}{\partial \chi_1^2} + x_2^2 K \otimes \frac{\partial^2}{\partial \chi_2^2} \right) + \eta * x_1 x_2 K \otimes \frac{\partial}{\partial \chi_1} \frac{\partial}{\partial \chi_2} \\
&\qquad + t\eta * \left(x_1 K \otimes \frac{\partial}{\partial \chi_1} + x_2 K \otimes \frac{\partial}{\partial \chi_2} \right) \frac{\partial}{\partial \theta} \\
&\qquad + \eta * t \left(x_1 K \otimes \frac{\partial}{\partial \chi_1} + x_2 K \otimes \frac{\partial}{\partial \chi_2} \right) \frac{\partial}{\partial \theta} \\
&\qquad + \frac{1}{2} \left(t^2 \eta * K + 2t\eta * tK + \eta * t^2 K \right) \otimes \frac{\partial^2}{\partial \theta^2} \\
&\qquad + (t\eta * K + \eta * tK) \otimes \frac{\partial}{\partial \tau} \Bigg\} u_i \quad + \\
&\quad + \mathcal{O}(\epsilon)^3.
\end{aligned}
\tag{A.6}
$$

Here is where it makes sense to define the operators M_i according to equation (4.3.9).

Now, take perturbations of u about u_0 according to equation (4.3.7), and the result obtained in equation (A.6), and insert them into equation (A.2) to obtain

$$
\begin{aligned}
\epsilon u_1 + \epsilon^2 u_2 + + \epsilon^3 u_3 + \mathcal{O}(\epsilon^4) &= \eta * K \otimes \sum_{i=0}^{\infty} \gamma_i u_i \\
&= \epsilon \gamma_1 M_0 u_1 + \epsilon^2 \Big[M_0(\gamma_1 u_2 + \gamma_2 u_1^2) + \gamma_1 M_1 u_1 \Big] \quad + \\
&\quad + \epsilon^3 \Big[M_0(\gamma_1 u_3 + 2\gamma_2 u_1 u_2 + \gamma_3 u_1^3) + \\
&\qquad + M_1(\gamma_1 u_2 + \gamma_2 u_1^2) + \gamma_1 M_2 u_1 \Big] \quad + \\
&\quad + \mathcal{O}(\epsilon^4).
\end{aligned}
$$

It is possible to define an unfolding parameter δ according to $\gamma_1 = \gamma_c + \epsilon^2 \delta$, so that we can investigate dynamics in the neighbourhood of the bifurcation. Doing so brings us to the final stage, where we can pull out equations for each order of ϵ

$$
\begin{aligned}
u_1 &= \gamma_c M_0 u_1 \\
u_2 &= \gamma_c M_0 u_2 + \gamma_2 M_0 u_1^2 + \gamma_c M_1 u_1, \\
u_3 &= \gamma_c M_0 u_3 + M_0 \left(2\gamma_2 u_1 u_2 + \gamma_3 u_1^3 + \delta u_1 \right) + M_1 \left(\gamma_c u_2 + \gamma_2 u_1^2 \right) + \gamma_c M_2 u_1,
\end{aligned}
\tag{A.7}
$$

which can be rearranged to equation (4.3.8).

A.1.2 Details of Fredholm alternative inner products

This appendix section details the calculation of the inner products $\langle \phi_1, g_n \rangle$. Note that we only show the results of inner products using ϕ_1 since results with the other basis functions can be obtained by the same methods.

The first result is as easy as they come. We chose our basis functions to be orthogonal with respect to the inner product (4.3.11), so that we have

$$\langle \phi_1, u_1 \rangle = \left\langle \phi_1, \sum_{i=1}^{4} \left(A_i \phi_i + \bar{A}_i \bar{\phi}_i \right) \right\rangle = A_1. \tag{A.8}$$

Next, we have inner products with u_1^2. These are handled easily as well

$$\langle \phi_1, u_1^2 \rangle = \left\langle \phi_1, \left(\sum_{i=1}^{4} \left(A_i \phi_i + \bar{A}_i \bar{\phi}_i \right) \right)^2 \right\rangle = 0.$$

Equality here again comes down to orthogonality relationships of cosine and sine functions with respect to the defined inner product. The surviving terms in the expansion of the summation are all orthogonal to the ϕ_i basis functions. These two results are applied in the computation of $\langle \phi_1, g_2 \rangle$ in equation (4.3.13).

Now with the simple second order restriction computed, we move to the involved computation of the third order restriction $\langle \phi_1, g_3 \rangle$. We start with

$$\begin{aligned} \langle \phi_1, g_3 \rangle = {} & 2\gamma_2 \tilde{\eta} \widehat{K} \langle \phi_1, u_1 u_2 \rangle + \gamma_3 \tilde{\eta} \widehat{K} \langle \phi_1, u_1^3 \rangle + \delta \tilde{\eta} \widehat{K} \langle \phi_1, u_1 \rangle + \\ & + \gamma_c \left(-\frac{\partial}{\partial i k_1} \frac{\partial}{\partial \chi_1} + \frac{\partial}{\partial i \omega} \frac{\partial}{\partial \theta} \right) \tilde{\eta} \widehat{K} \langle \phi_1, u_2 \rangle + \\ & + \gamma_c \left[\frac{1}{2} \left(-\frac{\partial}{\partial i k_1} \frac{\partial}{\partial \chi_1} + \frac{\partial}{\partial i \omega} \frac{\partial}{\partial \theta} \right)^2 + \frac{\partial}{\partial i \omega} \frac{\partial}{\partial \tau} \right] \tilde{\eta} \widehat{K} \langle \phi_1, u_1 \rangle \\ = {} & 0, \end{aligned} \tag{A.9}$$

and can quickly apply equation (A.8) to two of the terms. With the help of Maple[1] we can also compute

$$\langle \phi_1, u_1^3 \rangle = 3A_1 \left[|A_1|^2 + 2 \left(|A_2|^2 + |A_3|^2 + |A_4|^2 \right) \right] + 6 \bar{A}_2 A_3 A_4,$$

and for the terms that include u_2, we must first calculate that. It is not possible to calculate u_2 directly, but one may assume that it will be a quadratic form of the complex exponential terms used in the lower order solution

$$u_2 = \sum_{l,m,n=\{0,\pm 1,\pm 2\}} B_{lmn} e^{i(l\omega_c t + m k_c x_1 + n k_c x_2)}. \tag{A.10}$$

Inserting this into the second equation in (A.7) permits us to pull out all values of

[1] Maple 18. Maplesoft, a division of Waterloo Maple Inc., Waterloo, Ontario.

l	m	n	$B_{lmn}/(\gamma_2 C_{lmn})$	l	m	n	$B_{lmn}/(\gamma_2 C_{lmn})$
-2	-2	0	$\bar{A}_1{}^2$	2	-2	0	A_2^2
-2	-1	-1	$2\bar{A}_1\bar{A}_3$	2	-1	-1	$2A_2A_4$
-2	-1	1	$2\bar{A}_1\bar{A}_4$	2	-1	1	$2A_2A_3$
-2	0	-2	$\bar{A}_3{}^2$	2	0	-2	A_4^2
-2	0	0	$2(\bar{A}_1\bar{A}_2+\bar{A}_3\bar{A}_4)$	2	0	0	$2(A_1A_2+A_3A_4)$
-2	0	2	$\bar{A}_4{}^2$	2	0	2	A_3^2
-2	1	-1	$2\bar{A}_2\bar{A}_3$	2	1	-1	$2A_1A_4$
-2	1	1	$2\bar{A}_2\bar{A}_4$	2	1	1	$2A_1A_3$
-2	2	0	$\bar{A}_2{}^2$	2	2	0	A_1^2

l	m	n	$B_{lmn}/(\gamma_2 C_{lmn})$
0	-2	0	$2\bar{A}_1\bar{A}_2$
0	-1	-1	$2(\bar{A}_1A_4+A_2\bar{A}_3)$
0	-1	1	$2(\bar{A}_1A_3+A_2\bar{A}_4)$
0	0	-2	$2\bar{A}_3A_4$
0	0	0	$2(\lvert A_1\rvert^2+\lvert A_2\rvert^2+\lvert A_3\rvert^2+\lvert A_4\rvert^2)$
0	0	2	$2A_3\bar{A}_4$
0	1	-1	$2(\bar{A}_2A_4+A_1\bar{A}_3)$
0	1	1	$2(\bar{A}_2A_3+A_1\bar{A}_4)$
0	2	0	$2A_1\bar{A}_2$

l	m	n	$B_{lmn}/(\gamma_2 C_{lmn})$	l	m	n	$B_{lmn}/(\gamma_2 C_{lmn})$
-1	-1	0	undetermined	1	-1	0	undetermined
-1	0	-1	undetermined	1	0	-1	undetermined
-1	0	1	undetermined	1	0	1	undetermined
-1	1	0	undetermined	1	1	0	undetermined

Table A.1: Nontrivial quadratic coefficients B_{lmn}, using C_{lmn} from equation (4.3.20).

B_{lmn} except those for $m=0$; $l,n=\pm1$ and $n=0$; $l,m=\pm1$ because those lie in the nullspace of $\mathcal{L}$. Aided again by Maple, we can compute 117 of the 125 components of B_{lmn}, most of them being 0, by using properties of the Laplace and the Fourier-Laplace tranform. The results are summarized in Table A.1.

Now that we have computed u_2, it is straightworward to determine the remaining inner products

$$\begin{aligned}\langle\phi_1,u_1u_2\rangle =&\gamma_2A_1\big[(2C_{000}+C_{220})|A_1|^2+2(C_{000}+C_{200}+C_{020})|A_2|^2\\ &+2(C_{211}+C_{011}+C_{000})|A_3|^2+2(C_{000}+C_{011}+C_{211})|A_4|^2\big]\\ &+2(C_{200}+2C_{011})\bar{A}_2A_3A_4,\end{aligned}$$

where symmetry properties in the indices of C_{lmn} have been used to combine terms, and

$$\langle \phi_1, u_2 \rangle = B_{110}. \tag{A.11}$$

The unknown B_{110} is actually a function of ξ_1, ξ_2, ξ_3, ξ_4, and τ.

Inserting all that is needed into equation (A.9), we obtain the equation

$$\begin{aligned} 0 = a_0 A_1 + A_1 \left[a_1 |A_2|^2 + a_2 \left(|A_1|^2 + |A_2|^2 \right) + a_3 \left(|A_3|^2 + |A_4|^2 \right) \right] + \\ + a_4 \bar{A}_2 A_3 A_4 + a_5 \frac{\partial^2 A_1}{\partial \xi_1^2} + \frac{\partial A_1}{\partial \tau} + D\gamma_c \left(-\frac{\partial}{\partial i k_1} \frac{\partial}{\partial \chi_1} + \frac{\partial}{\partial i \omega} \frac{\partial}{\partial \theta} \right) \tilde{\eta} \widehat{K} B_{110}, \end{aligned}$$

with the a_i coefficients and D as given in equation (4.3.19). Applying the chain rule for the derivatives acting on B_{110}, we can obtain

$$\begin{aligned} 0 = a_0 A_1 + A_1 \left[a_1 |A_2|^2 + a_2 \left(|A_1|^2 + |A_2|^2 \right) + a_3 \left(|A_3|^2 + |A_4|^2 \right) \right] + \\ + a_4 \bar{A}_2 A_3 A_4 + a_5 \frac{\partial^2 A_1}{\partial \xi_1^2} + \frac{\partial A_1}{\partial \tau} + \frac{v_g}{\gamma_c} \left(-2 \frac{\partial}{\partial \xi_2} + \frac{\partial}{\partial \xi_3} - \frac{\partial}{\partial \xi_4} \right) B_{110}. \end{aligned}$$

Since B_{110} is an unknown function, we want to eliminate it. If we average the equation over the ξ_1, ξ_2, and ξ_3 variables. That is, even though B_{110} depends on ξ_1, ξ_2, ξ_3, and ξ_4, averages of the form $\langle \langle \langle \frac{\partial B_{110}}{\partial \xi_j} \rangle_2 \rangle_3 \rangle_4$ (with the averages defined as in equation (4.3.18) for instance) will be independent of ξ_2, ξ_3, and ξ_4, leaving just just τ and ξ_1 as the independent variables.

The result is Eq. (4.3.14). If this method is repeated for ϕ_2, ϕ_3, and ϕ_4, the inner products will differ, but the final results are Eqs. (4.3.15)-(4.3.17).

A.2 Initialization files for nfSimulator

The initialization files used for simulation of the travelling and alternating rolls solutions in Figure 4.9 were performed with nfSimulator version 2.3.4. The initialization files for them are provided in the thesis repository
https://bitbucket.org/kegr/uoit_thesis.

Appendix B

Resources for Liley's model

B.1 Calculations **132**
B.1.1 Equivalence of Integral and PDE models 132
B.1.2 Normal form coefficient example 132
B.2 Numerical algorithm descriptions **134**
B.2.1 PETSc overview 134
B.2.2 Timestepping 135
B.2.3 Stepping of the first variational equation 136
B.2.4 Equilibria 137
B.2.5 Periodic solutions 138
B.3 PETSc simulation code initialization files **139**
B.4 Testing of simulation code **139**
B.4.1 Numerical timestepping error 139
B.4.2 Accuracy testing 139
Bibliography **141**

This appendix provides some additional details for calculations and simulations regarding Liley's model. The notation used in normal form computation section is consistent with the body of the text, but notation in the numerical section is distinct for simplicity. The numerical section is essentially that present in Green & van Veen [6].

B.1 Calculations

Specific useful calculations that were omitted from the text include the derivation of the PDE model from the integral system. And the process for computing $D_4 \ltimes T^2$ symmetric Hopf normal form coefficients.

B.1.1 Equivalence of Integral and PDE models

We do not reproduce this calculation here. Rather, we point to sources where similar calculations were used. We stress again that the equivalence can be shown by taking Fourier transforms in the infinite domain.

For the temporal operator $*$, Fourier transform in only the time dimension allows the η_j, η_{jk} to be written in terms of temporal differential operators on the left hand side.

For the spatiotemporal operator, Fourier transforming in time and both spatial dimensions will show the equivalence. This is because the Fourier transform of Eq. (2.4.5) will result in a rational polynomial in the norm of the wave vector and the temporal frequency. Sufficient details of this calculation are provided in Appendix B in Liley et al. [8].

B.1.2 Normal form coefficient example

The normal form calculation is not presented in full detail here. Instead, we just give the ideas that allow us to actually compute the second order solution and the restriction of the third order equation.

Second order solution

For the second order solution, it is useful to define a short notation, χ_{lmn}, as the matrix

$$\chi_{lmn} = \text{diag}\left(\begin{bmatrix} \tilde{\eta}_e(il\omega_c) \\ \tilde{\eta}_i(il\omega_c) \\ \tilde{\eta}_{ee}(il\omega_c)\widehat{K}_{ee}((m,n)^T k_c, il\omega_c) \\ \tilde{\eta}_{ie}(il\omega_c)\widehat{K}_{ie}((m,)^T k_c, il\omega_c) \\ \tilde{\eta}_{ei}(il\omega_c)\widehat{K}_{ei}((m,n)^T k_c, il\omega_c) \\ \tilde{\eta}_{ii}(il\omega_c)\widehat{K}_{ii}((m,n)^T k_c, il\omega_c) \end{bmatrix}\right). \tag{B.1}$$

With this, we define a vector for the quadratic terms evaluated at q (the null vector)

$$r = \begin{bmatrix} -\left(\frac{q_3}{|h_{ee}^{eq}-h_e^r|}+\frac{q_4}{|h_{ie}^{eq}-h_e^r|}\right)q_1 \\ -\left(\frac{q_5}{|h_{ei}^{eq}-h_i^r|}+\frac{q_6}{|h_{ii}^{eq}-h_i^r|}\right)q_2 \\ g_e^2(q_1)^2 \\ g_i^2(q_2)^2 \\ g_e^2(q_1)^2 \\ g_i^2(q_2)^2 \end{bmatrix}. \tag{B.2}$$

With this notation, it can be shown that the second order solution will satisfy

$$u^2(\mathbf{x},t) = \sum_{l=-2}^{2}\sum_{m=-2}^{2}\sum_{n=-2}^{2}\mathbf{C}_{lmn}e^{i(l\omega_c t+mk_c x_1+nk_c x_2)}, \tag{B.3}$$

with $\mathbf{C_{lmn}}$ the solution to a matrix equation

$$L((m,n)^T k_c, il\omega_c)\mathbf{C}_{lmn} = A_{lmn}r, \tag{B.4}$$

for L the Fourier-Laplace transformed linear operator, and A_{lmn} the scalar quantity (for a fixed l,m,n) with the same entries as $B_{lmn}/\gamma_2 C_{lmn}$ used in the scalar equation (Table A.1). A difference though, is that we do not have the undetermined terms, as those were caused by resonant terms that came up from the M_1 operator, which has become identically 0 for our simplified analysis.

Maple makes quick work of computing u^2, and we suppress the output, avoiding the gaze of Medusa. Now that we have the second order solution (still with arbitrary amplitudes A_j), we move to the applying the Fredholm alternative to the third order equation.

Third order restriction

The Fredholm alternative applied to the third order perurbation equation can be rewritten as (for nullvector $p\phi_1$)

$$\langle p\phi_1, g^3\rangle = \langle p\phi_1, \chi_{101}v^0 + D_2 v^2\rangle \tag{B.5}$$

with the matrix D_2

$$D_2 = \text{diag}\left(\begin{bmatrix} 0 \\ 0 \\ \frac{\partial}{\partial i\omega}\tilde{\eta}_{ee}(i\omega_c)\widehat{K}_{ee}((m,n)^T k_c, il\omega_c)\frac{\partial}{\partial\tau} \\ \frac{\partial}{\partial i\omega}\tilde{\eta}_{ie}(i\omega_c)\widehat{K}_{ie}((m,n)^T k_c, il\omega_c)\frac{\partial}{\partial\tau} \\ \frac{\partial}{\partial i\omega}\tilde{\eta}_{ei}(i\omega_c)\widehat{K}_{ei}((m,n)^T k_c, il\omega_c)\frac{\partial}{\partial\tau} \\ \frac{\partial}{\partial i\omega}\tilde{\eta}_{ii}(i\omega_c)\widehat{K}_{ii}((m,n)^T k_c, il\omega_c)\frac{\partial}{\partial\tau} \end{bmatrix}\right). \tag{B.6}$$

vector v^0

$$v^0 = \begin{bmatrix} -\left(\frac{u_3^2}{|h_{ee}^{eq}-h_e^r|}+\frac{u_4^2}{|h_{ie}^{eq}-h_e^r|}\right)u_1^1 - \left(\frac{u_3^1}{|h_{ee}^{eq}-h_e^r|}+\frac{u_4^1}{|h_{ie}^{eq}-h_e^r|}\right)u_1^2 \\ -\left(\frac{u_5^2}{|h_{ei}^{eq}-h_i^r|}+\frac{u_6^2}{|h_{ii}^{eq}-h_i^r|}\right)u_2^1 - \left(\frac{u_5^1}{|h_{ei}^{eq}-h_i^r|}+\frac{u_6^1}{|h_{ii}^{eq}-h_i^r|}\right)u_2^2 \\ 2g_e^2u_1^1u_1^2 + g_e^3(u_1^1)^3 \\ 2g_i^2u_2^1u_2^2 + g_i^3(u_2^1)^3 \\ 2g_e^2u_1^1u_1^2 + g_e^3(u_1^1)^3 \\ 2g_i^2u_2^1u_2^2 + g_i^3(u_2^1)^3 \end{bmatrix}, \tag{B.7}$$

and vector v^2

$$v^2 = \begin{bmatrix} 0 \\ 0 \\ g_e^1u_1^1 \\ g_i^1u_2^1 \\ g_e^1u_1^1 \\ g_i^1u_2^1 \end{bmatrix}. \tag{B.8}$$

With all of the above considered, the inner product of Eq. (B.5) can be numerically computed in a short amount of time. The result is an abundance of terms with numerical coefficients at or below the tolerance of the precision used. Discarding those negligible terms, we are left with only the A_j combinations present in the $D_4 \ltimes D^2$ symmetric normal form, and we can simply read off the normal form values.

B.2 Numerical algorithm descriptions

B.2.1 PETSc overview

Rather than creating our code from scratch, we opted to work with the Portable, Extensible Toolkit for Scientific Computation (PETSc): an open-source, object oriented library that is designed for the scalable solution and analysis of PDEs [2, 1]. PETSc is written in the C language, and is usable from C/C++ as well as Fortran and Python. We use PETSc in conjunction with the Scalable Library for Eigenvalue Problem Computations (SLEPc) [7], for the computation of eigenspectra of equilibrium and periodic solutions. Since our implementation uses some features of PETSc that are recent additions and are still being modified, we use the development version of both projects.

PETSc is split up into multiple components to address the various problems associated with solving PDEs numerically. For our purposes, we treat the `DM` component, which handles the topology of the discretization, as the most fundamental, from which we can easily derive memory allocation and communication for distributed vectors (`Vec`) and matrices (`Mat`). With vectors and matrices, we can now solve linear systems, such as those that arise in Newton iteration for implicit time-stepping and the

computation of equilibria and periodic orbits. PETSc's component for this is called `KSP`, and it has numerous iterative solvers implemented, as well as preconditioners, (`PC`), to increase convergence rates. For implicit time-stepping, for example, we use GMRES , preconditioned with incomplete LU (ILU) factorization, combined with the block Jacobi method [11, 10]. On top of the linear solvers come the nonlinear solvers, PETSc's `SNES` component, which implements a few different methods, such as globally convergent Newton iteration with line search [4]. Finally, PETSc provides a timestepping component, `TS`, to obtain time dependent solutions. Implemented here are numerous explicit and implicit schemes such as adaptive stepsize Runge-Kutta and implicit Euler. The implicit schemes make use of the `SNES` component. A schematic of the hierarchy discussed here can be found in Fig. B.1.

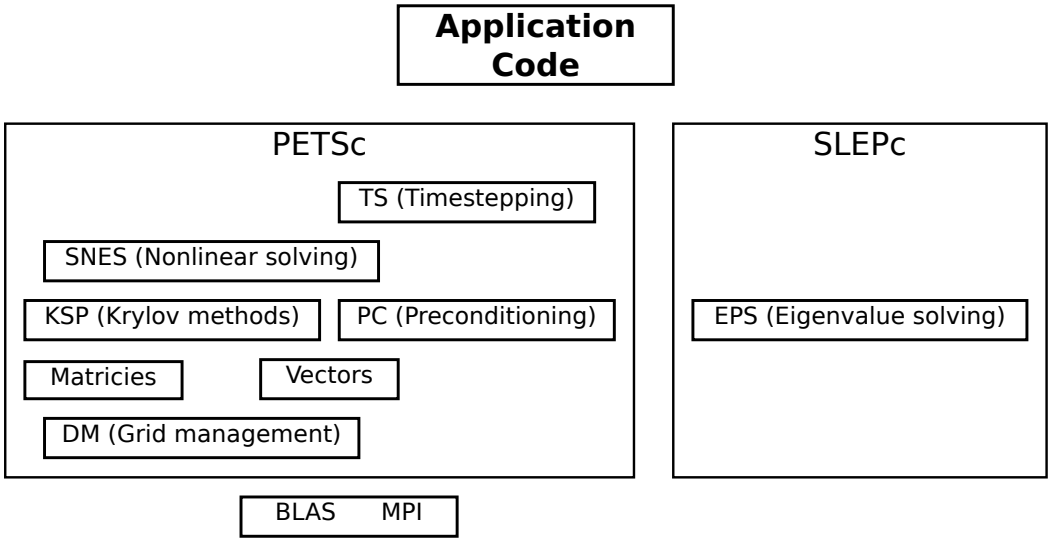

Figure B.1: Schematic representation of the components of PETSc and SLEPc used in our code, and their relative hierarchy.

For our dynamical systems calculations we will frequently need to compute specific eigenvalues and eigenvectors for system-sized matrices. For this end, we use SLEPc, which implements iterative eigenvalue solvers using PETSc `Vec` and `Mat` distributed data structures. The component of SLEPc that we use is `EPS`, which has a few algorithms for iteratively solving eigenproblems. Its default algorithm is Krylov-Schur iteration.

B.2.2 Timestepping

We currently use an arbitrary method to time step the discretized equations. This subsection goes through the process of timestepping with the implicit Euler method. Since we are aiming to compute periodic orbits, rather than to generate long time series, the first order accuracy of the method is not an issue. Once a periodic orbit is computed, the time step size can be reduced to increase accuracy.

We symbolically write the dynamical system as

$$\dot{u} = f(u), \quad f : \mathbb{R}^N \to \mathbb{R}^N. \tag{B.1}$$

where N is the total number of unknowns after discretization, in our case $14 \times N_x \times N_y$. The implicit Euler scheme for time integration is given by

$$u_{n+1} = u_n + \mathrm{d}t\, f(u_{n+1}) \tag{B.2}$$

where the subscript represents the step number, $\mathrm{d}t$ the step size, and u_0 the initial conditions. This nonlinear equation is solved by Newton iteration:

$$u_{n+1}^{k+1} = u_{n+1}^{k} + \mathrm{d}u^k, \tag{B.3}$$

where the superscript denotes the Newton iterate, and $\mathrm{d}u^k$ is the solution to the linear system

$$\left(\mathbb{I} - \mathrm{d}t \left. \frac{\partial f}{\partial u} \right|_{u_{n+1}^k} \right) \mathrm{d}u^k = \mathrm{d}t\, f(u_{n+1}^k) - u_{n+1}^k + u_n^k, \tag{B.4}$$

where $\partial f / \partial u$ denotes the $N \times N$ Jacobian matrix. Provided that the initial approximation, u_{n+1}^0, is close enough to the actual solution of equation (B.2), this iteration should converge quadratically. This is achieved by making the initial approximation the result of an explicit Euler step

$$u_{n+1}^0 = u_n + \mathrm{d}t\, f(u_n). \tag{B.5}$$

As we scale up the size of our problems, it becomes the linear solve in equation (B.4) that takes most of the time. This problem is handled by using GMRES to solve the linear system. For large time steps, the spectrum of the matrix in Eq. (B.4) is spread out, and we need to precondition it for iterative solving. We make use ILU, which has shown to be reliable for this type of problem [12, 9]. If we use more than one processor, PETSc uses distributed storage for the matrix, and combines ILU with block Jacobi preconditioning.

B.2.3 Stepping of the first variational equation

The variational equations for the dynamical system are written as

$$\dot{v} = \left. \frac{\partial f}{\partial u} \right|_u v, \quad v \in \mathbb{R}^N \tag{B.6}$$

and must be integrated simultaneously with the dynamical system (B.1). Solving the variational equations allow us to compute the stability of solutions, and is also an essential ingredient for the treatment of boundary value problems such as those that arise in the computation of periodic orbits.

Performing implicit Euler timestepping on the variational equations (B.6) requires

solutions of the linear problems

$$\left(\mathbb{I} - \mathrm{d}t \left.\frac{\partial f}{\partial u}\right|_{u_{n+1}}\right) v_{n+1} = v_n. \tag{B.7}$$

Since we already have the Jacobian of the dynamical system at timestep $n+1$, stepping the variational equations requires only one additional $N \times N$ linear solve per time step.

B.2.4 Equilibria

Having set up the function `FormFunction` for the right hand side of the dynamical system, and its Jacobian computation `FormJacobian`, also used for time integration, we can set up equilibrium calculations using PETSc's `SNES` component with very little effort.

Equilibrium solutions to the dynamical system (B.1) are solutions that satisfy

$$f(u) = 0. \tag{B.8}$$

To solve this, we can set up a Newton iteration scheme

$$u^{k+1} = u^k + \mathrm{d}u^k \tag{B.9}$$

with $\mathrm{d}u$ coming from the solution of the linear system

$$\left.\frac{\partial f}{\partial u}\right|_{u^k} \mathrm{d}u^k = -f(u^k). \tag{B.10}$$

As with the timestepping, if the initial guess is good enough this will converge quadratically provided that $\left.\frac{\partial f}{\partial u}\right|_{u^k}$ is nonsingular. Unlike the case of time stepping, though, we do not always have a way to produce an initial approximation that is good enough. For stable equilibrium solutions, we can use timestepping to get close to an equilibrium, but this will not work for unstable equilibria. One possible solution is using globally convergent Newton methods. Using such methods we can find equilibria from very coarse initial data, at the cost of computing many iterations. The line search algorithm and the trust region approach (see, e.g., [4]) are implemented in the `SNES` component.

Stability of equilibrium solutions follows from the spectrum of the Jacobian. Because of the reflection symmetries of the model, these will mostly appear in groups. On a square domain, for instance, a single eigenvalue will be associated with up to eight eigenvectors, with wavenumbers $(\pm k_x, \pm k_y)$ and $(\pm k_y, \pm k_x)$.

As discussed in Section 3.3.2, the model on square periodic domains is also equivariant under translatations in both dimensions. In the presence of this symmetry, it is more natural to search for *relative* equilibria, also called travelling waves. This leads to the introduction of two extra unknowns, that can be thought of as the wave velocities, into system (B.8), and an extension by two equations of the associated linear

system (B.10). However, since we have so far only observed spatially homogeneous equilibrium states, we will discuss this adjustment in Sec. B.2.5 on periodic solutions.

B.2.5 Periodic solutions

The primary instability in the Liley model is often a Hopf bifurcation, and periodic orbits have been shown to play an important role in the dynamics of ODE reductions of the model (e.g. [5, 14]). However, space dependent periodic orbits have not previously been computed and studied. Using PETSc data structures for bordered matrices, in conjunction with a `MATSHELL`, we can solve for periodic orbits based on the time stepping described in Secs. B.2.2 and B.2.3.

Relative periodic orbits solve the boundary value problem

$$F(u,t) = \phi(t,u) - T_{ab}u = 0, \tag{B.11}$$

where ϕ is the flow of the dynamical system (B.1), t is the period, and $T_{ab}u(x,y) = u(x+a, y+b)$ the translation operator. Our strategy for solving this equation is essentially that of Sanchez *et al.* [13], namely Newton iterations combined with unconditioned GMRES iteration. Linearising Eq. (B.11) gives

$$(D_u\phi(u,t) - \mathbb{I})\,\mathrm{d}u + f(\phi(u,t))\mathrm{d}t - \frac{\partial u}{\partial x}\mathrm{d}a - \frac{\partial u}{\partial y}\mathrm{d}b = -F(u,t), \tag{B.12}$$

where $D_u\phi$ is a matrix of derivatives of the flow with respect to its initial condition. Upon convergence, this is the monodromy matrix of the periodic orbit. The result is N equations in $N+3$ unknowns, which must be closed by phase conditions. For the temporal phase, we opted to handle this by providing a constraint on the Newton update step:

$$[D_u\phi(u,t)]_{k,\cdot}\,\mathrm{d}u + f_k(\phi(u,t))\mathrm{d}t = 0. \tag{B.13}$$

As $D_u\phi$ is a matrix, $[D_u\phi(u,t)]_{k,\cdot}$ denotes the k^{th} row of the matrix $D_u\phi$. As Similar constraints can be applied to fix the phase in the spatial dimensions as well:

$$\begin{aligned} \frac{\partial u}{\partial x}\mathrm{d}u &= 0, \\ \frac{\partial u}{\partial y}\mathrm{d}u &= 0. \end{aligned} \tag{B.14}$$

These choices give the bordered system

$$\begin{bmatrix} (D_u\phi(u,t) - T_{ab}) & f(\phi(u,t)) & -\frac{\partial u}{\partial x} & -\frac{\partial u}{\partial y} \\ [D_u\phi(u,t)]_{k,\cdot} & f_k(\phi(u,t)) & 0 & 0 \\ \frac{\partial u}{\partial x} & 0 & 0 & 0 \\ \frac{\partial u}{\partial y} & 0 & 0 & 0 \end{bmatrix} \begin{bmatrix} \mathrm{d}u \\ \mathrm{d}t \\ \mathrm{d}a \\ \mathrm{d}b \end{bmatrix} = \begin{bmatrix} -F(u,t) \\ 0 \\ 0 \\ 0 \end{bmatrix}, \tag{B.15}$$

the solution to which can be used to update the approximate solution

$$\begin{bmatrix} u^{n+1} \\ t^{n+1} \\ a^{n+1} \\ b^{n+1} \end{bmatrix} = \begin{bmatrix} u^{n} \\ t^{n} \\ a^{n} \\ b^{n} \end{bmatrix} + \begin{bmatrix} \mathrm{d}u \\ \mathrm{d}t \\ \mathrm{d}a \\ \mathrm{d}b \end{bmatrix}. \tag{B.16}$$

The matrix $D_u\phi$ is dense, so we should avoid calculating and storing it explicitly. Iterative solving of the linear problem, (B.15), requires the computation of matrix-vector products, which are constructed from the integration of the variational equation (B.6) with $v = \mathrm{d}u$ and the vector field $f(\phi(u,t))$ at the end point of the approximately periodic orbit. This method will work well in dispersive regimes of the PDE, i.e., when most of the eigenvalues of the monodromy matrix are clustered around zero. This aids the convergence of GMRES, without any preconditioning. Sanchez *et al.* [13] provide bounds for the number of GMRES iterations for the Navier-Stokes equation, and the convergence we observe for the Liley model is qualitatively similar.

B.3 PETSc simulation code initialization files

Similar to the scalar model, all of the initialization files for this code have been provided and organized in the online mercurial repository for this thesis:
`https://bitbucket.org/kegr/uoit_thesis`.

B.4 Testing of simulation code

This section summarizes some of the testing that was performed on our PETSc code for Liley's model. The timestepping order testing for both the full system and the linearized equations are supplied in the mercurial repository.

B.4.1 Numerical timestepping error

For timestepping, we choose a fixed discretization and a fixed time integration time, and vary the size of the time step for. This allows us to compute an approximate error, as in Figure B.2. Of all of the timestepping methods shown, their computed order match theoretical prediction at least in some region.

B.4.2 Accuracy testing

Determining that our code is capable of producing correct results is not as straightforward as the above finite difference testing. To do this, we must compare certain computations of the PETSc code with results demonstrated in past literature.

The literature chosen was that of Bojak & Liley [3], with the problem that the

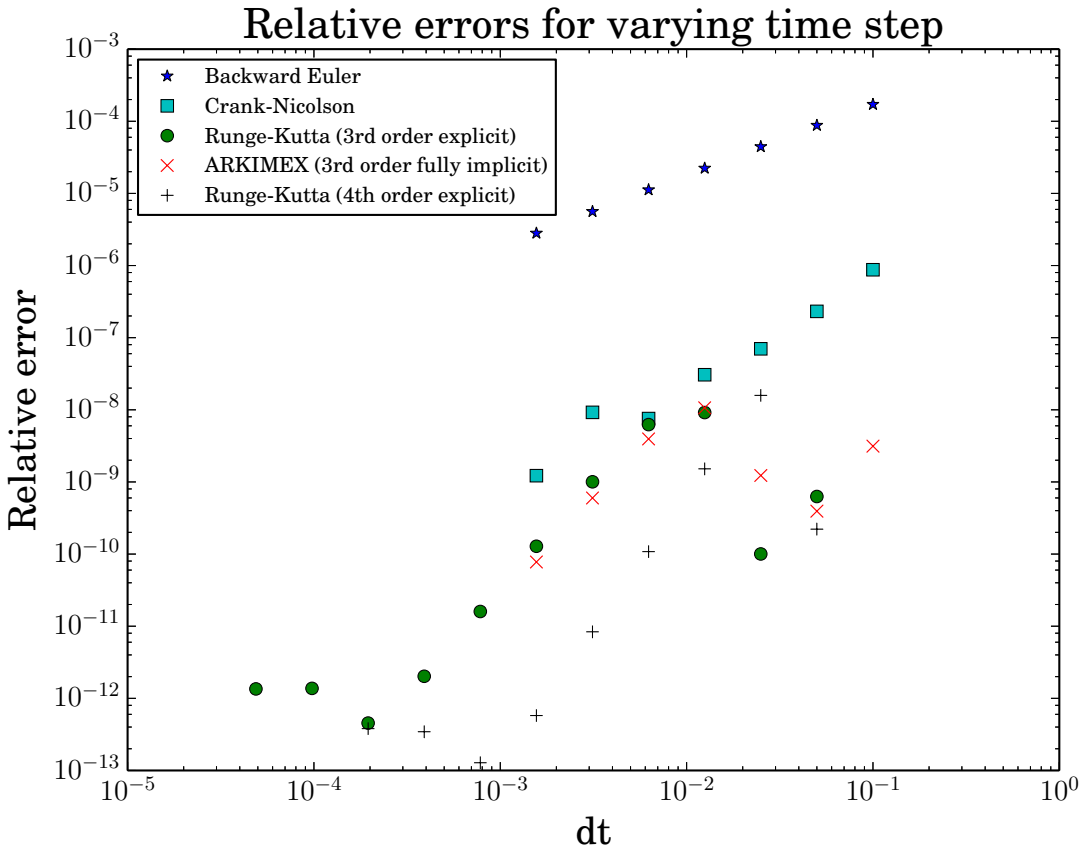

Figure B.2: Relative differences computed after a time integration of 100ms using various timestepping methods. State is initialized with a space-dependent field that will result in varying dynamics (i.e., not an equilibrium). With the final state written as a function of time step, $u(\mathrm{d}t)$, this relative error is computed by

$$err(\mathrm{d}t) = \frac{||u(2\mathrm{d}t) - u(\mathrm{d}t)||_2}{||u(\mathrm{d}t)||_2},$$

with $\|\cdot\|_2$ denoting the 2-norm of its vector entry. Note that the implicit methods took *much* longer to integrate than the explicit, and thus their $\mathrm{d}t$ do not get as small.

results are only expressed graphically. To reproduce the results we first wrote some (more simple) AUTO-07p code that could reproduce the data of the SHE and SHPO curves in the right side of Figure 5.3. Confirming that both the equilibrium and periodic orbit curves look as in the published figure.

We then compare the data of our PETSc SHE continuation curve with the data from the AUTO-07p code, with results (not included here) being equivalent up to 7 digits.

The PETSc code is further verified, qualtitatively, by observing the principle instability of the SHE in the correct parameter region indicated from the published article (right side of Figure 5.4). As the article does not include a precise calculation of this instability, this is the best we can do.

Combining the accuracy testing on stationary states with the order calculations for various timestepping methods, gives us high confidence that our implementation of Liley's model in PETSc is correct.

Bibliography

[1] Balay, S., Brown, J., Buschelman, K., Eijkhout, V., Gropp, W. D., Kaushik, D., Knepley, M. G., Curfman, L. M., Smith, B. F., and Zhang, H. PETSc Users Manual. Tech. rep., Argonne National Laboratory, 2012.

[2] Balay, S., Brown, J., Buschelman, K., Gropp, W. D., Kaushik, D., Knepley, M. G., Curfman, L. M., Smith, B. F., and Zhang, H. PETSc Web page, 2012.

[3] Bojak, I., and Liley, D. Self-organized 40Hz synchronization in a physiological theory of EEG. *Neurocomputing 70* (2007), 2085–2090.

[4] Dennis, J. E., and Schnabel, R. B. *Numerical Methods for Unconstrained Optimization and Nonlinear Equations*. Classics in Applied Mathematics. Prentice-Hall, Englewood Cliffs, NJ, 1983.

[5] Frascoli, F., van Veen, L., Bojak, I., and Liley, D. T. Metabifurcation analysis of a mean field model of the cortex. *Physica D 240*, 11 (2011), 949–962.

[6] Green, K. R., and van Veen, L. Open-source tools for dynamical analysis of Liley's mean-field cortex model. *Journal of Computational Science 5*, 3 (2014), 507–516.

[7] Hernandez, V., Roman, J. E., and Vidal, V. SLEPc: A scalable and flexible toolkit for the solution of eigenvalue problems. *ACM Transactions on Mathematical Software 31*, 3 (2005), 351–362.

[8] Liley, D. T. J., Cadusch, P. J., and Dafilis, M. P. A spatially continuous mean field theory of electrocortical activity. *Network Computation in Neural Systems 13*, 1 (2002), 67–113.

[9] Saad, Y. Preconditioned Krylov subspace methods for CFD applications. Tech. rep., Minnesota Supercomputer Institute, Minneapolis, 1994.

[10] Saad, Y. *Iterative Methods for Sparse Linear Systems*, 2 ed. Society for Industrial and Applied Mathematics, Philadelphia, PA, 2003.

[11] Saad, Y., and Schultz, M. H. GMRES: A Generalized Minimal Residual Algorithm for Solving Nonsymmetric Linear Systems. *SIAM Journal on Scientific and Statistical Computing 7*, 3 (1986), 856–869.

[12] Sanchez, J., Marques, F., and Lopez, J. M. A Continuation and Bifurcation Technique for Navier-Stokes Flows. *Journal of Computational Physics 180*, 1 (2002), 78–98.

[13] Sanchez, J., Net, M., Garcia-Archilla, B., and Simo, C. Newton-Krylov continuation of periodic orbits for Navier-Stokes flows. *Journal of Computational Physics 201*, 1 (2004), 13–33.

[14] van Veen, L., and Liley, D. Chaos via Shilnikov's Saddle-Node Bifurcation in a Theory of the Electroencephalogram. *Phys Rev Lett 97*, 20 (Nov. 2006), 1–4.

Appendix C

Copyright permissions

C.1 Oxford – Nunez & Srinivasan 2006 . . . . . **144**
C.2 IOP Publishing – Silber & Knobloch 1991 . . . . . **146**
C.3 Elsevier – Frascoli et al. 2011 . . . . . **149**
C.4 Elsevier – Bojak & Liley 2007 . . . . . **156**

Some figures in this thesis were reproduced from published sources. These are the required copyright permissions allowing them to be used in this document, ordered by appearance.

C.1 Oxford – Nunez & Srinivasan 2006

Figures 2.4 and 2.5.

Kevin Green

From: Academic Permissions <Academic.permissions@oup.com>
Sent: June-10-15 5:36 AM
To: Kevin Green
Subject: FW: Academic Permissions Request Form

Dear Mr Green,

Thank you for your request. You have our permission to use the OUP Material you list in your email below in your thesis for submission to University of Ontario Institute of Technology.

If at some future date your thesis is published it will be necessary to re-clear this permission. Please also note that if the material to be used is acknowledged to any other source, you will need to clear permission with the rights holder.

Kind regards,

IF THIS PERMISSION IS INCLUDED IN ANY THESIS/DISSERTATION MADE AVAILABLE ONLINE PLEASE REMOVE MY NAME AND CONTACT INFORMATION. THANK YOU.

From: no.reply@oup.com [mailto:no.reply@oup.com]
Sent: 09 June 2015 15:39
To: Academic Permissions
Subject: Academic Permissions Request Form

0_0_URL	/uk/academic/rights/permissions/request
A_Z_firstname	Kevin
A_Z_lastname	Green
B_Z_Company	University of Ontario Institute of Technology
C_Z_Address	2000 Simcoe Street North
C_Z_zip	L1H 7K4
D_Z_PhoneNo	+1-905-721-8668 x 5368
D_Z_country	Canada
E_Z_FaxNo	
F_Z_Email	kevin.green@uoit.ca
F_Z_VATnumber	
G_Z_TheirTitle	Dynamic Square Patterns in Two Dimensional Neural Fields
H_Z_Author	Kevin R. Green
H_Z_Publisher	University of Ontario Institute of Technology

I_Z_Covers	Both
I_Z_PrintRunHard	0
I_Z_pubDate	August 2015
J_Z_Territory	Canada
K_Z_Language	English
K_Z_Notes	This is a PhD thesis.
L_Z_Media1	illustration
M_Z_Author1	Paul Nunez and Ramesh Srinivasan
M_Z_Title1	Electric Fields of the Brain: The Neurophysics of EEG 2nd ed.
M_Z_editedby1	
N_Z_Material1	Figure 2-3. page 64. schematic drawing of neocortical dipole layers, with EEG and MEG measurement Figure 11-4. page 496. schematic drawing of cortical columns
O_Z_ISBN1	978-0-19-505038-7
O_Z_OUPpubDate1	2006
P_Z_Media2	Text
Q_Z_Author2	
Q_Z_Title2	
Q_Z_editedby2	
R_Z_Material2	
S_Z_ISBN2	
S_Z_OUPpubDate2	
T_Z_Media3	Text
U_Z_Author3	
U_Z_Title3	
U_Z_editedby3	
V_Z_ISBN3	
V_Z_Material3	
V_Z_OUPpubDate3	
W_Z_Additional	
subject	
view	submitform

C.2 IOP Publishing – Silber & Knobloch 1991

Figure 3.6.

Kevin Green

From: on behalf of Permissions <permissions@iop.org>
Sent: June-10-15 4:35 AM
To: Kevin Green
Subject: Re: PLS Clear Permission Request - [701] NONLINEARITY (09517715)

Dear Kevin Green,

Thank you for your request to reproduce IOP Publishing material in your thesis.

Regarding:

Figure 9 (Nonlinearity 4 (1991) 1063-1106.)

We are happy to grant permission for the use you request on the terms set out below.

Conditions

Non-exclusive, non-transferrable, revocable, worldwide, permission to use the material in print and electronic form will be granted **subject to the following conditions:**

- Permission will be cancelled without notice if you fail to fulfil any of the conditions of this letter.
- You will make reasonable efforts to contact the author(s) to seek consent for your intended use. Contacting one author acting expressly as authorised agent for their co-authors is acceptable.
- You will reproduce the following prominently alongside the material:
  - the source of the material, including author, article title, title of journal, volume number, issue number (if relevant), page range (or first page if this is the only information available) and date of first publication. This information can be contained in a footnote or reference note; or
  - a link back to the article (via DOI); and
  - if practical and IN ALL CASES for works published under any of the Creative Commons licences the words "© IOP Publishing & London Mathematical Society. Reproduced with permission. All rights reserved"
- The material will not, without the express permission of the author(s), be used in any way which, in the opinion of IOP Publishing, could distort or alter the author(s)' original intention(s) and meaning, be prejudicial to the honour or reputation of the author(s) and/or imply endorsement by the author(s) and/or IOP Publishing.
- Payment of £0 is received in full by IOP Publishing prior to use.

Special Conditions – For STM Signatories ONLY (as agreed as part of the STM Guidelines)

Any permissions granted for a particular edition will apply also to subsequent editions and for editions in other languages, provided such editions are for the work as a whole in situ and does not involve the separate exploitation of the permitted illustrations or excerpts.

If you have any questions, please feel free to contact our Permissions team at permissions@iop.org.

I should be grateful if you would acknowledge receipt of this email.

Kind regards,

IOP Publishing

Please note: We do not usually provide signed permission forms as a separate attachment. Please print this email and provide it to your publisher as proof of permission.

From: <plsclear@pls.org.uk>
To: <permissions@iop.org>,
Cc: <plsclear@pls.org.uk>, <plsclearlive@gmail.com>
Date: 09/06/2015 16:02
Subject: PLS Clear Permission Request - [701] NONLINEARITY (09517715)

Here is a permissions request for you. It has been generated by PLSclear, the Publishers Licensing Society's new permissions tool.

The tool ensures that

- you only receive requests for content you own, and that the requests go to the right people in your company
- you receive all the necessary information to grant requests (PLSclear uses a questionnaire that has been developed by some of the UK's leading rights specialists).

We hope this saves you time and makes managing the process easier.

If this is not one of your titles, you cannot grant permission or perhaps we have emailed the wrong contact, then please click the following link and tell us so that we can update our records: [Unable to process this request]

I am applying for permission for:

NONLINEARITY (09517715)	
A **illustration** extract	
content source:	**Online**
issue date:	**November 1991**
issue number:	**4**
issue URL:	**http://iopscience.iop.org/0951-7715/4/4**
article title:	**Hopf Bifurcation on a Square Lattice**

figure number & title / caption:	**Figure 9: Bifurcation diagrams indicating direction of bifurcation and stability...**
position on page:	**whole page**
reproduction colour:	**Black and White**
reproduction size:	**Full page**
positioning:	**inside or later pages**

To be used in:

A **Book, Journal, Magazine or Academic Paper...**	
The **Thesis** details are	
type of document:	**PhD Thesis**
publication title:	**Dynamic Square Patterns in Two Dimensional Neural Fields**
number of pages:	**160**
estimated publication date:	**August 2015**
distribution:	**print/electronic**
other relevant Information:	**Canadian graduate theses are reproduced by the Library and Archives of Canada (formerly Nati**

Please respond directly to the person making the request. They have not received your company name or contact details.

Contact details are

Name:	**Kevin Green**
Email:	**kevin.green@uoit.ca**
Address:	**2000 Simcoe Street North**
Town /City:	**Oshawa, Ontario**
Post Code:	**L1H 7K4**

Help us improve PLSclear: 5 quick questions

C.3 Elsevier – Frascoli et al. 2011

Figure 2.15.

ELSEVIER LICENSE
TERMS AND CONDITIONS

Jun 01, 2015

This is a License Agreement between Kevin R Green ("You") and Elsevier ("Elsevier") provided by Copyright Clearance Center ("CCC"). The license consists of your order details, the terms and conditions provided by Elsevier, and the payment terms and conditions.

All payments must be made in full to CCC. For payment instructions, please see information listed at the bottom of this form.

Supplier	Elsevier Limited The Boulevard,Langford Lane Kidlington,Oxford,OX5 1GB,UK
Registered Company Number	1982084
Customer name	Kevin R Green
Customer address	UOIT - Faculty of Science Oshawa, ON L1H 7K4
License number	3640390465691
License date	Jun 01, 2015
Licensed content publisher	Elsevier
Licensed content publication	Physica D: Nonlinear Phenomena
Licensed content title	Metabifurcation analysis of a mean field model of the cortex
Licensed content author	Federico Frascoli,Lennaert van Veen,Ingo Bojak,David T.J. Liley
Licensed content date	15 May 2011
Licensed content volume number	240
Licensed content issue number	11
Number of pages	14
Start Page	949
End Page	962
Type of Use	reuse in a thesis/dissertation
Portion	figures/tables/illustrations
Number of figures/tables/illustrations	1
Format	both print and electronic
Are you the author of this Elsevier article?	No
Will you be translating?	No
Original figure numbers	Figure 1
Title of your thesis/dissertation	Dynamic square patterns in some two dimensional neural fields
Expected completion date	Aug 2015

Estimated size (number of pages)	150
Elsevier VAT number	GB 494 6272 12
Permissions price	0.00 CAD
VAT/Local Sales Tax	0.00 CAD / 0.00 GBP
Total	0.00 CAD
Terms and Conditions	

INTRODUCTION

1. The publisher for this copyrighted material is Elsevier. By clicking "accept" in connection with completing this licensing transaction, you agree that the following terms and conditions apply to this transaction (along with the Billing and Payment terms and conditions established by Copyright Clearance Center, Inc. ("CCC"), at the time that you opened your Rightslink account and that are available at any time at http://myaccount.copyright.com).

GENERAL TERMS

2. Elsevier hereby grants you permission to reproduce the aforementioned material subject to the terms and conditions indicated.

3. Acknowledgement: If any part of the material to be used (for example, figures) has appeared in our publication with credit or acknowledgement to another source, permission must also be sought from that source. If such permission is not obtained then that material may not be included in your publication/copies. Suitable acknowledgement to the source must be made, either as a footnote or in a reference list at the end of your publication, as follows:

"Reprinted from Publication title, Vol /edition number, Author(s), Title of article / title of chapter, Pages No., Copyright (Year), with permission from Elsevier [OR APPLICABLE SOCIETY COPYRIGHT OWNER]." Also Lancet special credit - "Reprinted from The Lancet, Vol. number, Author(s), Title of article, Pages No., Copyright (Year), with permission from Elsevier."

4. Reproduction of this material is confined to the purpose and/or media for which permission is hereby given.

5. Altering/Modifying Material: Not Permitted. However figures and illustrations may be altered/adapted minimally to serve your work. Any other abbreviations, additions, deletions and/or any other alterations shall be made only with prior written authorization of Elsevier Ltd. (Please contact Elsevier at permissions@elsevier.com)

6. If the permission fee for the requested use of our material is waived in this instance, please be advised that your future requests for Elsevier materials may attract a fee.

7. Reservation of Rights: Publisher reserves all rights not specifically granted in the combination of (i) the license details provided by you and accepted in the course of this licensing transaction, (ii) these terms and conditions and (iii) CCC's Billing and Payment terms and conditions.

8. License Contingent Upon Payment: While you may exercise the rights licensed immediately upon issuance of the license at the end of the licensing process for the transaction, provided that you have disclosed complete and accurate details of your proposed use, no license is finally effective unless and until full payment is received from you (either by publisher or by CCC) as provided in CCC's Billing and Payment terms and conditions. If full payment is not received on a timely basis, then any license preliminarily granted shall be deemed automatically revoked and shall be void as if never granted. Further, in the event that you breach any of these terms and conditions or any of CCC's Billing and Payment terms and conditions, the license is automatically revoked and shall be void as if never granted. Use of materials as described in a revoked license, as well as any use of the materials beyond the scope of an unrevoked license, may constitute copyright infringement and publisher reserves the right to take any and all action to protect its copyright in the materials.

9. Warranties: Publisher makes no representations or warranties with respect to the licensed material.

10. Indemnity: You hereby indemnify and agree to hold harmless publisher and CCC, and their respective officers, directors, employees and agents, from and against any and all claims arising out of your use of the licensed material other than as specifically authorized pursuant to this license.

11. No Transfer of License: This license is personal to you and may not be sublicensed, assigned, or transferred by you to any other person without publisher's written permission.

12. No Amendment Except in Writing: This license may not be amended except in a writing signed by both parties (or, in the case of publisher, by CCC on publisher's behalf).

13. Objection to Contrary Terms: Publisher hereby objects to any terms contained in any purchase order, acknowledgment, check endorsement or other writing prepared by you, which terms are inconsistent with these terms and conditions or CCC's Billing and Payment terms and conditions. These terms and conditions, together with CCC's Billing and Payment terms and conditions (which are incorporated herein), comprise the entire agreement between you and publisher (and CCC) concerning this licensing transaction. In the event of any conflict between your obligations established by these terms and conditions and those established by CCC's Billing and Payment terms and conditions, these terms and conditions shall control.

14. Revocation: Elsevier or Copyright Clearance Center may deny the permissions described in this License at their sole discretion, for any reason or no reason, with a full refund payable to you. Notice of such denial will be made using the contact information provided by you. Failure to receive such notice will not alter or invalidate the denial. In no event will Elsevier or Copyright Clearance Center be responsible or liable for any costs, expenses or damage incurred by you as a result of a denial of your permission request, other than a refund of the amount(s) paid by you to Elsevier and/or Copyright Clearance Center for denied permissions.

LIMITED LICENSE

The following terms and conditions apply only to specific license types:

15. **Translation**: This permission is granted for non-exclusive world **English** rights only unless your license was granted for translation rights. If you licensed translation rights you may only translate this content into the languages you requested. A professional translator must perform all translations and reproduce the content word for word preserving the integrity of the article. If this license is to re-use 1 or 2 figures then permission is granted for non-exclusive world rights in all languages.

16. **Posting licensed content on any Website**: The following terms and conditions apply as follows: Licensing material from an Elsevier journal: All content posted to the web site must maintain the copyright information line on the bottom of each image; A hyper-text must be included to the Homepage of the journal from which you are licensing at http://www.sciencedirect.com/science/journal/xxxxx or the Elsevier homepage for books at http://www.elsevier.com; Central Storage: This license does not include permission for a scanned version of the material to be stored in a central repository such as that provided by Heron/XanEdu.

Licensing material from an Elsevier book: A hyper-text link must be included to the Elsevier homepage at http://www.elsevier.com . All content posted to the web site must maintain the copyright information line on the bottom of each image.

Posting licensed content on Electronic reserve: In addition to the above the following clauses are applicable: The web site must be password-protected and made available only to bona fide students registered on a relevant course. This permission is granted for 1 year only. You may obtain a new license for future website posting.

17. **For journal authors:** the following clauses are applicable in addition to the above:

Preprints:

A preprint is an author's own write-up of research results and analysis, it has not been peer-reviewed, nor has it had any other value added to it by a publisher (such as formatting, copyright, technical enhancement etc.).

Authors can share their preprints anywhere at any time. Preprints should not be added to or enhanced in any way in order to appear more like, or to substitute for, the final versions of articles however authors can update their preprints on arXiv or RePEc with their Accepted Author Manuscript (see below).

If accepted for publication, we encourage authors to link from the preprint to their formal publication via its DOI. Millions of researchers have access to the formal publications on ScienceDirect, and so links will help users to find, access, cite and use the best available version. Please note that Cell Press, The Lancet and some society-owned have different preprint policies. Information on these policies is available on the journal homepage.

Accepted Author Manuscripts: An accepted author manuscript is the manuscript of an article that has been accepted for publication and which typically includes author-incorporated changes suggested during submission, peer review and editor-author communications.

Authors can share their accepted author manuscript:

- immediately
    - via their non-commercial person homepage or blog
    - by updating a preprint in arXiv or RePEc with the accepted manuscript
    - via their research institute or institutional repository for internal institutional uses or as part of an invitation-only research collaboration work-group
    - directly by providing copies to their students or to research collaborators for their personal use
    - for private scholarly sharing as part of an invitation-only work group on commercial sites with which Elsevier has an agreement
- after the embargo period
    - via non-commercial hosting platforms such as their institutional repository
    - via commercial sites with which Elsevier has an agreement

In all cases accepted manuscripts should:

- link to the formal publication via its DOI
- bear a CC-BY-NC-ND license - this is easy to do
- if aggregated with other manuscripts, for example in a repository or other site, be shared in alignment with our hosting policy not be added to or enhanced in any way to appear more like, or to substitute for, the published journal article.

Published journal article (JPA): A published journal article (PJA) is the definitive final record of published research that appears or will appear in the journal and embodies all value-adding publishing activities including peer review co-ordination, copy-editing, formatting, (if relevant) pagination and online enrichment.

Policies for sharing publishing journal articles differ for subscription and gold open access articles:

Subscription Articles: If you are an author, please share a link to your article rather than the full-text. Millions of researchers have access to the formal publications on ScienceDirect, and so links will help your users to find, access, cite, and use the best available version.

Theses and dissertations which contain embedded PJAs as part of the formal submission can be posted publicly by the awarding institution with DOI links back to the formal publications on ScienceDirect.

If you are affiliated with a library that subscribes to ScienceDirect you have additional private sharing rights for others' research accessed under that agreement. This includes use for classroom teaching and internal training at the institution (including use in course packs and courseware programs), and inclusion of the article for grant funding purposes.

Gold Open Access Articles: May be shared according to the author-selected end-user license and should contain a CrossMark logo, the end user license, and a DOI link to the formal publication on ScienceDirect.

Please refer to Elsevier's posting policy for further information.

18. **For book authors** the following clauses are applicable in addition to the above: Authors are permitted to place a brief summary of their work online only. You are not allowed to download and post the published electronic version of your chapter, nor may you scan the printed edition to create an electronic version. **Posting to a repository:** Authors are permitted to post a summary of their chapter only in their institution's repository.

19. **Thesis/Dissertation**: If your license is for use in a thesis/dissertation your thesis may be submitted to your institution in either print or electronic form. Should your thesis be published commercially, please reapply for permission. These requirements include permission for the Library and Archives of Canada to supply single copies, on demand, of the complete thesis and include permission for Proquest/UMI to supply single copies, on demand, of the complete thesis. Should your thesis be published commercially, please reapply for permission. Theses and dissertations which contain embedded PJAs as part of the formal submission can be posted publicly by the awarding institution with DOI links back to the formal publications on ScienceDirect.

Elsevier Open Access Terms and Conditions

You can publish open access with Elsevier in hundreds of open access journals or in nearly 2000 established subscription journals that support open access publishing. Permitted third party re-use of these open access articles is defined by the author's choice of Creative Commons user license. See our open access license policy for more information.

Terms & Conditions applicable to all Open Access articles published with Elsevier:

Any reuse of the article must not represent the author as endorsing the adaptation of the article nor should the article be modified in such a way as to damage the author's honour or reputation. If any changes have been made, such changes must be clearly indicated.

The author(s) must be appropriately credited and we ask that you include the end user license and a DOI link to the formal publication on ScienceDirect.

If any part of the material to be used (for example, figures) has appeared in our publication with credit or acknowledgement to another source it is the responsibility of the user to ensure their reuse complies with the terms and conditions determined by the rights holder.

Additional Terms & Conditions applicable to each Creative Commons user license:

CC BY: The CC-BY license allows users to copy, to create extracts, abstracts and new works from the Article, to alter and revise the Article and to make commercial use of the Article (including reuse and/or resale of the Article by commercial entities), provided the user gives appropriate credit (with a link to the formal publication through the relevant DOI), provides a link to the license, indicates if changes were made and the licensor is not represented as endorsing the use made of the work. The full details of the license are

available at http://creativecommons.org/licenses/by/4.0.

CC BY NC SA: The CC BY-NC-SA license allows users to copy, to create extracts, abstracts and new works from the Article, to alter and revise the Article, provided this is not done for commercial purposes, and that the user gives appropriate credit (with a link to the formal publication through the relevant DOI), provides a link to the license, indicates if changes were made and the licensor is not represented as endorsing the use made of the work. Further, any new works must be made available on the same conditions. The full details of the license are available at http://creativecommons.org/licenses/by-nc-sa/4.0.

CC BY NC ND: The CC BY-NC-ND license allows users to copy and distribute the Article, provided this is not done for commercial purposes and further does not permit distribution of the Article if it is changed or edited in any way, and provided the user gives appropriate credit (with a link to the formal publication through the relevant DOI), provides a link to the license, and that the licensor is not represented as endorsing the use made of the work. The full details of the license are available at http://creativecommons.org/licenses/by-nc-nd/4.0. Any commercial reuse of Open Access articles published with a CC BY NC SA or CC BY NC ND license requires permission from Elsevier and will be subject to a fee.

Commercial reuse includes:

- Associating advertising with the full text of the Article
- Charging fees for document delivery or access
- Article aggregation
- Systematic distribution via e-mail lists or share buttons

Posting or linking by commercial companies for use by customers of those companies.

20. **Other Conditions**:

v1.7

Questions? customercare@copyright.com or +1-855-239-3415 (toll free in the US) or +1-978-646-2777.

C.4 Elsevier – Bojak & Liley 2007

Figures 5.3- 5.5.

Pages 3-7 of license identical to Frascoli license, and thus omitted.

ELSEVIER LICENSE
TERMS AND CONDITIONS

Jun 01, 2015

This is a License Agreement between Kevin R Green ("You") and Elsevier ("Elsevier") provided by Copyright Clearance Center ("CCC"). The license consists of your order details, the terms and conditions provided by Elsevier, and the payment terms and conditions.

All payments must be made in full to CCC. For payment instructions, please see information listed at the bottom of this form.

Supplier	Elsevier Limited The Boulevard,Langford Lane Kidlington,Oxford,OX5 1GB,UK
Registered Company Number	1982084
Customer name	Kevin R Green
Customer address	UOIT - Faculty of Science
	Oshawa, ON L1H 7K4
License number	3640430557347
License date	Jun 01, 2015
Licensed content publisher	Elsevier
Licensed content publication	Neurocomputing
Licensed content title	Self-organized 40Hz synchronization in a physiological theory of EEG
Licensed content author	William R. Holmes,D.T.J. Liley
Licensed content date	June 2007
Licensed content volume number	70
Licensed content issue number	10-12
Number of pages	6
Start Page	2085
End Page	2090
Type of Use	reuse in a thesis/dissertation
Intended publisher of new work	other
Portion	figures/tables/illustrations
Number of figures/tables/illustrations	3
Format	both print and electronic
Are you the author of this Elsevier article?	No
Will you be translating?	No
Original figure numbers	Figures 1, 2 and 3
Title of your thesis/dissertation	Dynamic square patterns in some two dimensional neural fields

Expected completion date	Aug 2015
Estimated size (number of pages)	150
Elsevier VAT number	GB 494 6272 12
Permissions price	0.00 CAD
VAT/Local Sales Tax	0.00 CAD / 0.00 GBP
Total	0.00 CAD
Terms and Conditions	